Technische Universität München

Lehrstuhl für Angewandte Mechanik

Spatial Dynamics of Pushbelt CVTs

Dipl.-Tech. Math. Univ. Thorsten Schindler

Vollständiger Abdruck der von der Fakultät für Maschinenwesen der
Technischen Universität München zur Erlangung des akademischen Grades eines

Doktor-Ingenieurs

genehmigten Dissertation.

Vorsitzender:

Univ.-Prof. Dr.-Ing. Bernd-Robert Höhn

Prüfer der Dissertation:

1. Univ.-Prof. Dr.-Ing. habil. Heinz Ulbrich
2. Univ.-Prof. Dr. rer. nat. habil. Martin Arnold, Martin-Luther-Universität Halle-Wittenberg

Die Dissertation wurde am 01.07.2010 bei der Technischen Universität München
eingereicht und durch die Fakultät für Maschinenwesen am 05.10.2010 angenommen.

Acknowledgment

This work summarises my results as scientific research assistant at the Institute of Applied Mechanics of the Technische Universität München. It was initiated and funded by Bosch Transmission Technology B.V.

The research project would not have been possible without the support of many people. I would like to express my gratitude to my supervisor Prof. Dr. Heinz Ulbrich who took a great interest in the topic. He offered an invaluable assistance and guidance but also the freedom to find one's feet and to assume responsibility for the different tasks at his institute. Especially the last articles are the reason that the time was such diversified, challenging and instructive in a convenient sense.

Deepest gratitude is also due to Prof. Dr. Martin Arnold for continuous and fruitful discussions about numerical mathematics and multibody formulations at different conferences; gratitude also for his support and for him being a member of the supervisory committee.

I would like to thank Prof. Dr. Friedrich Pfeiffer for his commitment and mentoring. The conversations about nonsmooth mechanics always stimulated the progress of the thesis and my understanding for this sophisticated research field.

The cooperation with Arie van der Velde, Han Pijpers and Arjen Brandsma of Bosch Transmission Technology B.V. was always like with a good colleague. I will treasure the visits for project meetings in Tilburg.

A main contribution of the excellent working atmosphere can be traced back to the cooperativeness of all colleagues at the institute. Special thanks to Markus Friedrich and Roland Zander, as well as the whole MBSim development crew for always being available to approach the solution of tricky and difficult modelling and programming questions. Markus Friedrich and Jan Clauberg have provided a perfect computer pool for extensive simulations for instance during the validation process. Thanks to Sebastian Lohmeier for making available his LaTeXclasses and to Thomas Cebulla for his notably efficient project assumption. Proofreading of the manuscript surely was not a nice job but the feedback of Markus Friedrich, Thomas Cebulla, Arie van der Velde and Claudia Kirmeyer was detailed and constructive.

Thanks to all my friends for giving the possibility to balance in my free time and for providing lots of ideas apart from the day-to-day work.

I wish to express my gratitude to my family for their understanding and support through the duration of my studies and doing a Doctor of Philosophy.

Garching, October 2010 *Thorsten Schindler*

Unsere Zeit steckt, wie kaum eine andere zuvor,
voller Möglichkeiten – zum Guten und Bösen.
Nichts kommt von selbst.
Darum – besinnt Euch auf Eure Kraft und darauf,
dass jede Zeit eigene Antworten will und man auf ihrer Höhe zu sein hat,
wenn Gutes bewirkt werden soll.

Willy Brandt
18.12.1913 – 08.10.1992

4th German Chancellor
22.10.1969 – 16.05.1974

Nobel Peace Prize Laureate
10.12.1971

read by Hans-Jochen Vogel on the occasion of the socialist international congress in Berlin on 15.09.1992
Willy Brandt was already seriously ill at this time

Contents

Abstract

With a pushbelt continuously variable transmission (CVT), the whole drivetrain including the engine of a passenger car can operate in an optimal state at any time. For further improvements with respect to fuel consumption, dynamic simulations of the system have been investigated by Bosch Transmission Technology B.V. and the Institute of Applied Mechanics of the Technische Universität München in recent years.

The underlying mathematical models are characterised by numerous contacts and a large degree of freedom. In order to avoid high numerical stiffnesses due to springs and to encourage an efficient as well as a stable and robust numerical treatment, a nonsmooth contact description is chosen. Timestepping schemes are used to integrate the resulting measure differential inclusions.

This work deals with a spatial transient mathematical model of pushbelt continuously variable transmissions to consider also out-of-plane effects, for instance pushbelt misalignment. The equations of motion result from using methods of multibody theory and nonlinear mechanics. The bodies themselves are described using rigid and large deflection elastic mechanical models. In-between the bodies, all possible flexible or rigid contact descriptions namely frictionless unilateral contacts, bilateral contacts with planar friction and even unilateral contacts with spatial friction occur.

In comparison with the planar case, the calculation time increases significantly mainly because of the large degree of freedom and the number of contact possibilities. Stationary initial value problems are solved and parallelisation techniques are tested to reduce the computational effort.

The validation with measurements of global values like thrust ratio, spiral running of the pushbelt in the pulleys and alignment as well as of local internal contact forces correlates very well. This completely proves the applicability of the simulation model.

Altogether, a new level of detail in CVT modelling has been achieved giving the possibility to further analyse this complex physical system.

1 Point of Departure

The PhD thesis [27] marks the point of departure for the scientific discussion about the current pushbelt continuously variable transmission (CVT) research project of the Institute of Applied Mechanics at the Technische Universität München[1] with Bosch Transmission Technology B.V.[2] This chapter is devoted to outline the state-of-the-art concepts concerning CVTs based on the pushbelt principle, nonsmooth flexible multibody dynamics and generalised time integration schemes for measure differential inclusions. These topics have been the background both in [27] to achieve a detailed planar dynamical model of the pushbelt CVT and in the following to derive a spatial extension. References to the respective literature and a summary of the objectives close this introduction.

1.1 Pushbelt CVTs

The reduction of greenhouse gas emissions has become a more and more important factor in daily politics; for example, the United Nations climate meeting lately collected all top-ranking politicians within the scope of the United Nations Framework Convention on Climate Change in Copenhagen in December 2009. In the resulting Kyoto II protocol and as a consequence of it, emission regulations will be decided for a responsibility phase beginning in 2013. This is similar to the constitutions in Kyoto 1997 for the responsibility phase of the Kyoto I protocol and its cross-national realisations from 2008 until 2012. What is the outcome of possible limitations for the transportation sector? First off, it is important to state that urbanisation will rather support than reduce the increase of transportation activity and that the use of alternative energy is still very challenging. Therefore, it is necessary for the automotive industry to refine the current engine and transmission technologies for meeting the early wave of emission regulations [72].

The CVT is an alternative transmission system for passenger cars with high expectation values. Especially the automatically optimal operation of the whole drive train including the engine explains its increasing production volume. Though there are many kinds of CVTs [72], chain and pushbelt types are most commonly used. At Bosch Transmission Technology B.V. pushbelt mass production began in 1985. By the end of 2008, 13 million vehicles were equipped with this transmission type in many markets such as Japan, Korea, China, North America and Europe [39]. About three million pushbelts are installed in over 70 different vehicle models per year.

1 `http://www.amm.mw.tum.de/`
2 `http://www.cvt.bosch.com/`

1.1.1 Set Up and Functionality

The variator of the transmission system is made up by an input and an output pulley as well as the pushbelt (left side of Fig. 1.1).

Figure 1.1: Pushbelt variator and pushbelt with elements.

Each of the pulleys consists of a fixed and an axially moveable V-shaped sheave. The pushbelt is composed of approximately 400 elements which are guided by two ring packages of nine to twelve steel rings (right side of Fig. 1.1).

Figure 1.2 shows the functionality for two different transmission ratios.

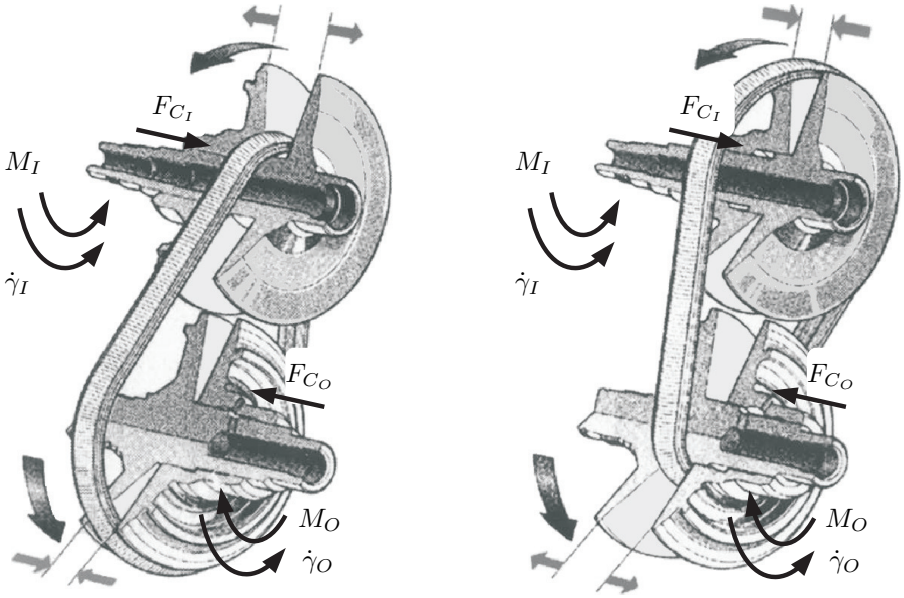

Figure 1.2: Functionality of the pushbelt variator for two different transmission ratios.

Here, $\dot{\gamma}$ denotes the angular velocity of a pulley, M the torque and F_C the axial clamping force acting on the loose sheaves. The torque is transmitted from the input (I) to the output (O) pulley via friction forces between the pushbelt and the sheaves and further on via push and tension forces within the pushbelt. By applying hydraulic pressures on the loose sheaves their axial positions can be changed, modifying the effective running radii of the pushbelt within the pulleys continuously.

1.1.2 Important Phenomena

Both pushbelt and chain CVTs belong to the category of friction-limited drives in contrast to conventional automatic gear trains which transmit power by form closure [54]. Overall topics are performance, slip behaviour, efficiency, configuration design, shift characteristics, power density, operating regime, variator package size, loss mechanisms, vibrations, noise and wear.

Concerning Sect. 1.1.1, the transmission is defined at least by a geometric ratio

$$i_r := \frac{r_O}{r_I} \tag{1.1}$$

of the input r_I and output r_O radius. The usual ratio spread is between about $i_r = 0.42$ and $i_r = 2.4$. By reason of the friction-closure, the speed ratio

$$i_s := \frac{\dot{\gamma}_I}{\dot{\gamma}_O} \tag{1.2}$$

might be different [52]. The absolute element – pulley slip speed is defined as

$$v_s := \dot{\gamma}_I r_I - \dot{\gamma}_O r_O \ . \tag{1.3}$$

Then, the relative element – pulley slip is given by

$$s_r := \frac{v_s}{\dot{\gamma}_O r_O} = \frac{i_s - i_r}{i_r} \ . \tag{1.4}$$

Often, the relationship

$$\zeta := \frac{F_{C_I}}{F_{C_O}} \tag{1.5}$$

between the input and output thrust is used as an indicator for element – pulley slip [14]. It is a function of the transmission i_r and the ratios

$$\xi_* := \frac{M_*}{M_{*,\max}} \ , \quad * \in \{I, O\} \tag{1.6}$$

between the current torque and a referencing maximum one (Sect. 3.2.1). If there is too less clamping, the element – pulley slip will in the worst case increase to macro slip and damage the whole system. Normal micro slip between element and pulleys, which is also called creep, is the main reason for variator losses and so mainly affects fuel saving possibilities [52, 72]. Though, with over-clamping there will be too much wear because of elastic shear deformations and compliance. One has to look for a way out of the dilemma of improving fuel consumption, performance and slip behaviour. The research community on the one side is interested in analysing accurately the variator behaviour with detailed models [39] and on the other side in controlling the clamping pressures and the resulting traction. The latter is done with fast models which are accurate enough by at least including *transient general*

inertia terms [72, 8]. Also other losses, for example due to wedge and *penetration* in the pulleys, translational and rotational *misalignment*, seals and bearings [72, 39], are regarded.

The contact zone between elements and pulleys can be divided into an idle and an active arc as well as into a transition region for ring tension and element compression, respectively [38, 72]. Then, the idea of dimensioning ζ from (1.5) is to get rid of the idle and transition arc at either the input or the output pulley. This results in an unstable equality of forces because the whole arc is used for power transmission and further extension would induce macro slip between elements and pulleys. For this reason controlling this phenomenon is very complicated and modelling of the contact as well as understanding its quasi-periodic and chaotic effects are still a topic of active research [42, 72]. How should the shock induced by the transition be compensated? How could the lubrication oil be represented? Is COULOMB *friction* sufficient? In the general case, it is supposed that COULOMB's law only represents the macro slip accurately enough but for both creep and slip a viscoelastic or STRIBECK law is needed. Otherwise, COULOMB is said to be sufficient if the pulleys are modelled as *flexible bodies*, which is necessary in any case. The so-called noise-phenomenon is governed by the running-in of the elements in the pulleys yielding sheave bending in rotational direction. The about 1% spiral deviation of the elements from the circular radial position in the pulley wedge –called spiral running– or the *shifting gradient* of the pushbelt are deeply rooted in the sheave flexibility and in the prestressing of the ring packages as well. If one is not directly interested in the distribution of losses on the sheave and its connection, the stiffness of bearing and tilting is not as important as the sheave flexibility. In steady states, an uneven elastic sinusoidal deformation due to the pulley clamping occurs which can be represented quasi-stationary by harmonic ansatz functions [59]. More general are local time-variant elastodynamic models of the sheaves.

Power is transmitted from the input pulley to the elements which accelerate the rings due to friction forces. A relative motion between elements and rings occurs because of different radial positions in the pulleys. The elements are faster than the rings in the smaller arc and they stick in part of the larger arc [27]. These different velocities yield a *not constant band tension* depending on the transmission ratio and axial prestressing. As input for the *element – ring friction*, they also mainly affect the scratch-phenomenon which is the highest eigenfrequency lower than 300Hz of the output pulley angular acceleration and the reason for gear rattle. Altogether, the element – ring slip should be reduced by minimising the difference between the element and ring running radii; though, in the majority of cases further design requirements constrict this demand [39]. As from the input to the output pulley at one strand the elements are pressed together forming a kind of *pressure* bar, a minimal size of the area between the elements where this force is transmitted and so a minimal difference of the element and ring running radii are necessary to ensure a basic lifetime of the pushbelt. Superposed at the other strand, the elements are more or less loose on the rings acting as a tensile bar [54]. Depending on the load case defined by $\dot{\gamma}_I$, M_O, i_r, F_{C_O}, the partition of pressure and tensile bar to the trums can change. Compression forces depend on the load torque, they nearly vanish for small

values of M_O but cannot be neglected for large values of M_O. At a threshold load torque, the compression force propagation switches the trum [28]. The efficiency of the power transmission is depending monotonically on the reciprocal of the play between the elements.

1.1.3 Simulation Models

A profound understanding of the dynamics of pushbelt CVTs is necessary to conduct future investigations. This can be achieved by mostly expensive and elaborate experiments or with simulation models. Validated computational models enable economical examinations and correspond to short development periods.

Excellent surveys about pushbelt CVTs are available [27, 72]. Most existing models are planar and established with the principle of quasi-static equilibrium [28, 59]. Available planar transient models consider only rubber belts [71], are modeled as one dimensional continuum [12, 13, 14], neglect inertia [40] or the bending stiffness of the belt [73]. Additionally, there are relatively simple models to analyse the vibrational behaviour [42]. Summarising, the validated model for the planar dynamics of the pushbelt variator deduced from the nonsmooth mechanics approach [27] is still the most accurate transient model available based on the important phenomena in Sect. 1.1.2. It can be used to identify the potential of the pushbelt CVT with respect to industrially relevant topics like fuel consumption [63].

Focusing on chain CVTs a lot of planar models [74] but also a spatial model [65] as well as comparative studies [81] are available. Detailed overviews are provided in the cited literature.

Besides the improvement of physical understanding of CVTs, the aim in all abovementioned cases is to optimise the operation mode by for instance enhancing the slip control [70, 52, 69, 58] or by optimising the design parameters [51, 39].

All CVTs show out-of-plane effects such as pushbelt misalignment or elastic behaviour of components. Design improvements especially with respect to wear and noise are only possible by applying a spatial theory as even very small deviations result in large forces as a consequence of an extreme stiffness [54]. That is why in the following, an extension of the planar model [27] is given using the nonsmooth mechanics approach and so describing spatial motion and three-dimensional contact behaviour. As a consequence in times of tightening emission legislation, further optimisations concerning comfort, cost, fun to drive and especially fuel consumption could be investigated in more detail.

1.2 Nonsmooth Multibody Systems

Nonsmooth multibody systems are special mechanical systems basically including rigid bodies and in space discretised deformable bodies [89] in a hybrid way. They

are additionally characterised by rigid unilateral and bilateral contacts as well as impacts which lead to discrete jumps within the system's velocities. Thus, the degree of freedom is not a constant function but changes during the simulation process and determines a time-variant topology. A unitary mathematical and numerical formulation [90] based on measure differential equations (MDE) with constraints has been processed in the last decades at different research institutes [10, 56, 83, 77, 11, 44, 45, 1, 20, 46]. It allows the efficient integration even of industrial systems with large numbers of transitions [54, 85, 82] and avoids both high artificial stiffnesses and additional modelling errors due to regularised interactions.

1.2.1 Measure Differential Equation

A measure differential equation [48]

$$\boldsymbol{M}\boldsymbol{\mu}^{\boldsymbol{u}} = \boldsymbol{\mu}^{\boldsymbol{G}} + \sum_{k} \boldsymbol{\mu}^{\boldsymbol{H}_k} \tag{1.7}$$

involves measures $\boldsymbol{\mu}$ representing the velocity by superscript $\boldsymbol{u}$, integrable forces by superscript $\boldsymbol{G}$ and impacts at countable points in time t_k, $k \in \mathbb{N}$, by superscript for Heaviside functions $\boldsymbol{H}_k$. The symmetric and positive definite mass matrix $\boldsymbol{M}$ depends on the position $\boldsymbol{q}$ of the system.

Equivalent to the MDE (1.7) it is also possible to distinguish between smooth (non-impulsive) dynamics

$$\boldsymbol{M}\dot{\boldsymbol{u}} = \boldsymbol{h} + \boldsymbol{W}\boldsymbol{\lambda}\,, \tag{1.8}$$

and impact (impulsive) dynamics

$$\boldsymbol{M}_k \left(\boldsymbol{u}_k^+ - \boldsymbol{u}_k^-\right) = \boldsymbol{W}_k \boldsymbol{\Lambda}_k \quad \forall k \in \mathbb{N} \tag{1.9}$$

using $\dot{\boldsymbol{u}}$ for denoting the weak time derivative of $\boldsymbol{u}$ and $\boldsymbol{u}_k^+$ as well as $\boldsymbol{u}_k^-$ for describing the velocity after and before an impact time t_k. The generalised velocities $\boldsymbol{u}$ depend on the positions $\boldsymbol{q}$ via the linear equation

$$\dot{\boldsymbol{q}} = \boldsymbol{Y}\,\boldsymbol{u} \text{ with } \boldsymbol{Y} = \boldsymbol{Y}\,(\boldsymbol{q}) \tag{1.10}$$

and the vector $\boldsymbol{h}$ contains all smooth external, internal and gyroscopic forces. These forces are functions of $\boldsymbol{q}$, $\boldsymbol{u}$ and explicitly of the time t and also hold reactions of single-valued contacts for example flexible ones. The directions of set-valued contact reactions are summarised in the wrench matrix

$$\boldsymbol{W} = \boldsymbol{W}\,(\boldsymbol{q}) \tag{1.11}$$

as well as $\boldsymbol{\lambda}$ and $\boldsymbol{\Lambda}_k$ refer to smooth and nonsmooth contact reaction values due to persisting contacts and respectively due to discrete impulses.

1.2.2 Contact Laws

The computation of the accelerations $\dot{\boldsymbol{u}}$ in (1.8) and the post-impact velocities $\boldsymbol{u}_k^+$ in (1.9) requires the knowledge of the unknown contact reactions $\boldsymbol{\lambda}$ and $\boldsymbol{\Lambda}_k$ governed by set-valued contact laws $(\boldsymbol{q}, \boldsymbol{u}, \boldsymbol{\lambda}, \boldsymbol{\Lambda}_k, t) \in \mathcal{N}$. These contact laws are described in the following.

First of all, only smooth motion is considered which means that no impacts occur. Then, closed contact implies a bilateral constraint

$$g_B = 0, \quad \lambda_B \lessgtr 0 \,, \tag{1.12}$$

where g_B denotes the normal distance of the interacting bodies in the contact point. The second type of contact also allows for detachment. The associated unilateral constraint is given by the Signorini-Fichera-condition

$$g_U \geq 0, \quad \lambda_U \geq 0, \quad g_U \lambda_U = 0 \tag{1.13}$$

with the normal distance g_U. The respective force laws are shown in Figs. 1.3(a) and 1.3(b).

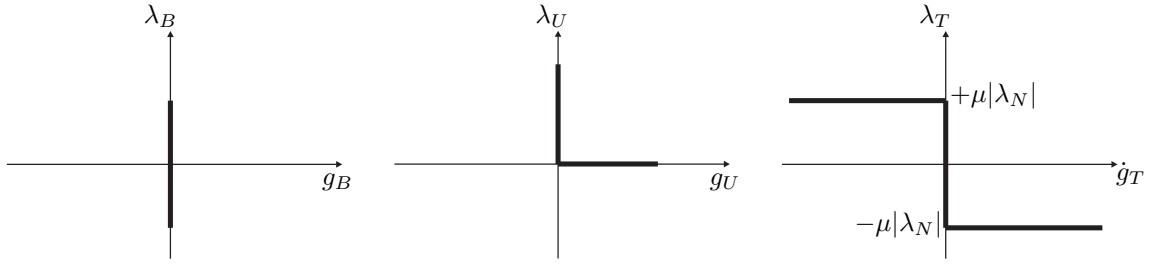

(a) Bilateral constraint. (b) Unilateral constraint. (c) Planar Coulomb friction.

Figure 1.3: Force laws for bi- and unilateral constraints and friction.

For both bi- and unilateral constraints for instance dry friction can be considered. In order to establish Coulomb's law, the force of a single contact is decomposed in a component $\lambda_N \in \{\lambda_B, \lambda_U\}$ normal to the contact plane and tangential components $\boldsymbol{\lambda}_T \in \mathbb{R}^2$ in friction direction. Using the relative tangential velocity $\dot{\boldsymbol{g}}_T \in \mathbb{R}^2$ and the friction coefficient μ, Coulomb's friction law is given by

$$\dot{\boldsymbol{g}}_T = \boldsymbol{0} \quad \Rightarrow \quad \|\boldsymbol{\lambda}_T\| \leq \mu|\lambda_N| \,, \tag{1.14a}$$

$$\dot{\boldsymbol{g}}_T \neq \boldsymbol{0} \quad \Rightarrow \quad \boldsymbol{\lambda}_T = -\frac{\dot{\boldsymbol{g}}_T}{\|\dot{\boldsymbol{g}}_T\|}\mu|\lambda_N| \,. \tag{1.14b}$$

For the planar case, it is plotted in Fig. 1.3(c).

An impact influences all contacts between bodies concerning the post impact velocity. Thus, the impact laws have to be formulated on velocity level substituting g by $\dot{g}^+$ and λ by Λ in (1.12) and (1.13) subject to the condition that the affected contact is closed. In this context, it is even possible to define special impact laws by replacing

$\dot{g}^+$ with adequate physical approximations to regard for example elastic impact behaviour [48].

The formulations of the contact and impact laws (1.12) to (1.14) are self-evident from the mechanical point of view [56, 30] but not suitable for the numerical computation [25]. A more appropriate formulation can be attained using convex analysis. With the proximal point to a convex set $C \subset \mathbb{R}^n$, $n \in \mathbb{N}$,

$$\mathbf{prox}_C(\boldsymbol{x}) = \arg\min_{\boldsymbol{x}^* \in C} |\boldsymbol{x} - \boldsymbol{x}^*|, \quad \boldsymbol{x} \in \mathbb{R}^n \tag{1.15}$$

the relations (1.12) to (1.14) have the form [3]:

$$\lambda_B = \mathrm{prox}_{C_B}(\lambda_B - r\, g_B)\,, \qquad \Lambda_B = \mathrm{prox}_{C_B}(\Lambda_B - r\, \dot{g}_B^+)\,, \tag{1.16a}$$

$$\lambda_U = \mathrm{prox}_{C_U}(\lambda_U - r\, g_U)\,, \qquad \Lambda_U = \mathrm{prox}_{C_U}(\Lambda_U - r\, \dot{g}_U^+)\,, \tag{1.16b}$$

$$\boldsymbol{\lambda}_T = \mathbf{prox}_{C_T(\lambda_N)}(\boldsymbol{\lambda}_T - r\, \dot{\boldsymbol{g}}_T)\,, \qquad \boldsymbol{\Lambda}_T = \mathbf{prox}_{C_T(\Lambda_N)}(\boldsymbol{\Lambda}_T - r\, \dot{\boldsymbol{g}}_T^+)\,. \tag{1.16c}$$

The corresponding convex sets are specified by

$$C_B = \mathbb{R}\,, \quad C_U = \{x \in \mathbb{R}\,;\, x \geq 0\}\,, \quad C_T(y) = \{\boldsymbol{x} \in \mathbb{R}^2\,;\, |\boldsymbol{x}| \leq \mu |y|\} \tag{1.17}$$

with $y \in \mathbb{R}$. The independent auxiliary parameter for each contact $r > 0$ is arbitrary from the mathematical but not from the numerical point of view. The optimal choice of r with respect to numerical efficiency and stability of the fixed-point or root-finding solution scheme is discussed [25], an efficient evaluation of (1.16) is described [50].

1.2.3 Contour Description

With the description outlined above, a mechanical system is divided into the motion of bodies and in the interaction between bodies. Only missing is the calculation of the wrench matrix $\boldsymbol{W}$, the gaps g and relative velocities $\dot{g}$. This is done body-per-body by assigning a contour characterised by a position vector

$$\boldsymbol{r} = \boldsymbol{r}(\boldsymbol{q}, \boldsymbol{s})\,, \tag{1.18}$$

the outward pointing contour normal

$$\boldsymbol{n} = \boldsymbol{n}(\boldsymbol{q}, \boldsymbol{s}) \tag{1.19}$$

and the tangents

$$\boldsymbol{T} = (\boldsymbol{t}_1(\boldsymbol{q}, \boldsymbol{s}), \boldsymbol{t}_2(\boldsymbol{q}, \boldsymbol{s})) \tag{1.20}$$

all depending on the generalised position $\boldsymbol{q}$ of the associated body and on the contour parameters $\boldsymbol{s}$ [89]. In this case assuming unique point-to-point contacts, the contact

parameters $\boldsymbol{s}_{c_1}$ and $\boldsymbol{s}_{c_2}$ for two contacting bodies necessarily fulfill

$$\boldsymbol{T}_1^T\left(\boldsymbol{s}_{c_1}\right)\left[\boldsymbol{r}_2\left(\boldsymbol{s}_{c_2}\right)-\boldsymbol{r}_1\left(\boldsymbol{s}_{c_1}\right)\right]=\boldsymbol{0}\ , \tag{1.21}$$

$$\boldsymbol{T}_2^T\left(\boldsymbol{s}_{c_2}\right)\left[\boldsymbol{r}_2\left(\boldsymbol{s}_{c_2}\right)-\boldsymbol{r}_1\left(\boldsymbol{s}_{c_1}\right)\right]=\boldsymbol{0}\ . \tag{1.22}$$

Depending on the structure of these equations either analytical (for geometric primitive contour pairings) or numerical for example NEWTON methods [17] have to be applied to get a set of potential contact parameters. Selecting the solution with minimal normal distance

$$g_N=\boldsymbol{n}_1\left(\boldsymbol{s}_{c_1}\right)\cdot\left[\boldsymbol{r}_2\left(\boldsymbol{s}_{c_2}\right)-\boldsymbol{r}_1\left(\boldsymbol{s}_{c_1}\right)\right] \tag{1.23}$$

allows the calculation of the relative normal and tangential velocities by projecting the relative velocity on the corresponding matrices $\boldsymbol{n}$ and $\boldsymbol{T}$ of the bodies:

$$\begin{pmatrix}\dot{g}_N\\ \dot{g}_{T_1}\\ \dot{g}_{T_2}\end{pmatrix}=\left(\boldsymbol{n}\ ,\boldsymbol{T}\right)^T\left[\boldsymbol{v}_2\left(\boldsymbol{s}_{c_2}\right)-\boldsymbol{v}_1\left(\boldsymbol{s}_{c_1}\right)\right]\ . \tag{1.24}$$

Each body's portion of the wrench matrix $\boldsymbol{W}$ is the projection of the Cartesian directions $\boldsymbol{n}$ and $\boldsymbol{T}$ of contact reactions in the space of generalised velocities $\boldsymbol{u}$ by appropriate JACOBIAN matrices $\left(\partial\,\dot{\boldsymbol{r}}/\partial\,\boldsymbol{u}\right)^T$.

1.3 Integration Schemes

Sophisticated computational methods have been established to adopt mechanical models to a wide range of industrial applications [4]. In order to integrate multibody systems with rigid contacts, two different numerical methods can be distinguished: event-driven and time-stepping schemes.

1.3.1 Event-Driven Integration Schemes

Event-driven or event tracking schemes [56] detect changes of the constraints, for example closing of unilateral contacts or stick-slip transitions, and resolve the exact transition times using indicator functions. Between these events, the motion of the system is smooth and can be computed by a standard integrator for differential algebraic equations [31]. While the general procedure using event-driven methods is known, the particular implementation depends on the underlying integrator. The treatment of constraints and the root finding mechanism play a crucial role in this context [26].

While the event-driven integration is very accurate, the detection of events can be time consuming especially in case of frequent transitions for example for systems with numerous contacts and Zeno phenomena. In principal, this approach is used for systems with only few configuration changes.

1.3.2 Time-Stepping Integration Schemes

In contrast to event-driven schemes, so-called time-stepping schemes belong to event capturing methods. They are based on the discretisation of the equations of motion including the constraints not adapting the globally fixed time step size Δt due to closing contacts. Hence, time-stepping schemes allow to focus on the global averaged physical behaviour of the simulated models. This reduces the number of combinatorial problems and avoids event detections. Therefore, a large number of contact transitions can be handled with increased computational efficiency if single events are not as important. On the other hand, common time-discretisations are of order one and the integrator is very sensitive with respect to the time step size influencing numerical stability and accuracy [34, 78, 24, 43, 25, 79].

A robust linear-implicit time-stepping algorithm of first order on velocity level is briefly introduced as an example. In the following, a single integration step $l \to l+1$ is outlined:

1. Compute the distances

   $$\boldsymbol{g}_U^l = \boldsymbol{g}_U(\boldsymbol{q}^l, t^l)$$

   of all unilateral contacts.

2. Compute the index set

   $$\{i \in \mathbb{N} : g_{U,i}^l \leq 0\}$$

   of active unilateral contacts and note that bilateral constraints are active by definition.

3. Compute the generalised velocities by solving the discretised equations of motion considering the active constraints (index a) on velocity level:

   $$\begin{aligned}
   \boldsymbol{u}^{l+1} &= \boldsymbol{u}^l + \left(\boldsymbol{M}_{\text{eff}}^l\right)^{-1} \left(\Delta t\, \boldsymbol{h}_{\text{eff}}^l + \boldsymbol{W}_a^l\, \boldsymbol{\Lambda}_a^l\right) , \\
   \dot{\boldsymbol{g}}_a^{l+1} &= \dot{\boldsymbol{g}}_a(\boldsymbol{u}^{l+1}, \boldsymbol{q}^l, t^{l+1}) , \\
   \boldsymbol{\Lambda}_a^{l+1} &= \mathbf{proj}(\dot{\boldsymbol{g}}_a^{l+1}, \boldsymbol{\Lambda}_a^{l+1}) .
   \end{aligned}$$

   The effective mass matrix and right hand side are given by

   $$\begin{aligned}
   \boldsymbol{M}_{\text{eff}}^l &= \boldsymbol{M}^l - \Delta t \left.\frac{\partial \boldsymbol{h}}{\partial \boldsymbol{u}}\right|_l - \Delta t^2 \left.\frac{\partial \boldsymbol{h}}{\partial \boldsymbol{q}}\right|_l \boldsymbol{Y}^l , \\
   \boldsymbol{h}_{\text{eff}}^l &= \boldsymbol{h}^l + \Delta t \left.\frac{\partial \boldsymbol{h}}{\partial \boldsymbol{q}}\right|_l \boldsymbol{Y}^l \boldsymbol{u}^l + \Delta t \left.\frac{\partial \boldsymbol{h}}{\partial t}\right|_l .
   \end{aligned}$$

   An implementation of the contact conditions according to Sect. 1.2.2 is denoted by **proj**.

4. Compute the new generalised positions

$$\boldsymbol{q}^{l+1} = \boldsymbol{q}^{l} + \Delta t\, \boldsymbol{Y}^{l}\, \boldsymbol{u}^{l+1} \ .$$

5. Correct numerical drifts.

1.4 MBSim

The software for modelling and simulation of nonsmooth dynamical systems at the Institute of Applied Mechanics of the Technische Universität München is called *MBSim* [47]. Mathematically, it is based on the ideas outlined in Sects. 1.2 and 1.3.

From the point of view of software development, a standard structure for multibody simulation frameworks distinguishing between bodies and interactions was proposed [60]. The programs [2, 7] also follow this approach. It is approved and used in *MBSim* using object-oriented C++ programming. Altogether, Fig. 1.4 shows the embedding of *MBSim* in the global simulation and analysing process.

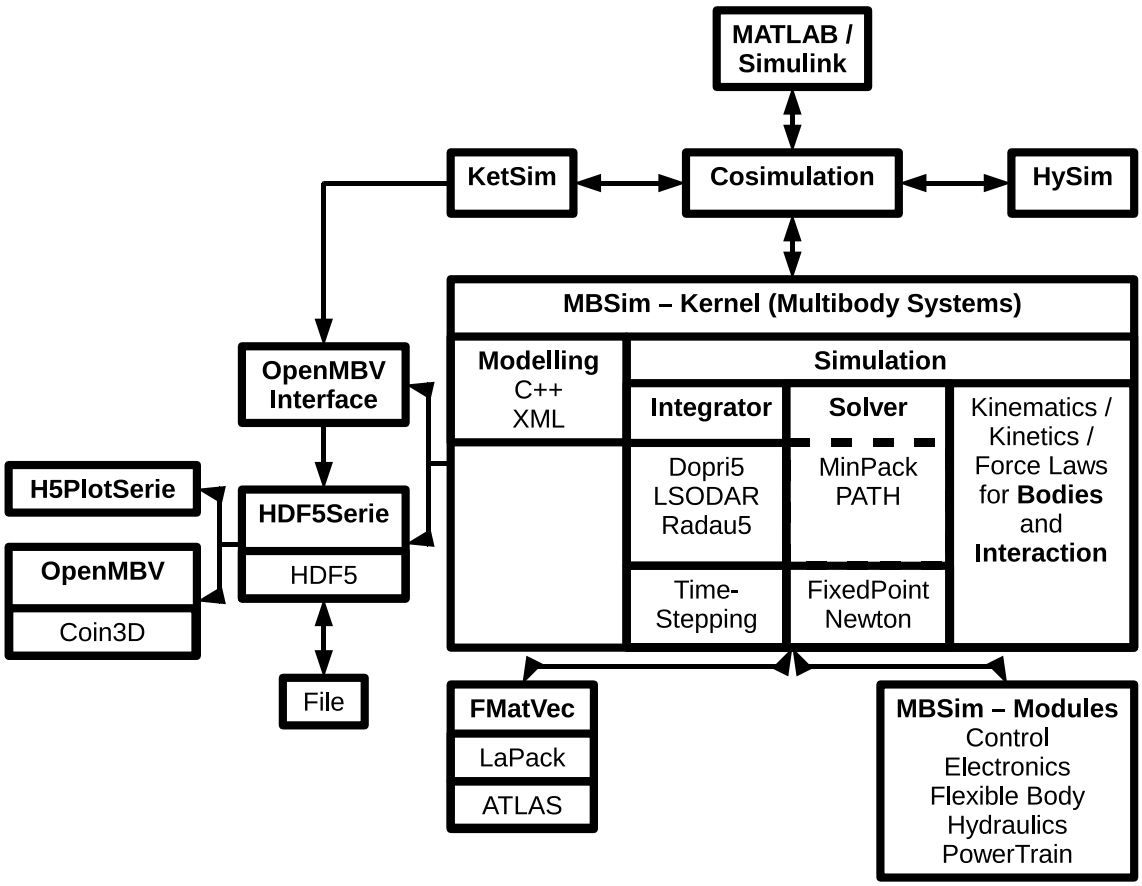

Figure 1.4: Embedding of *MBSim* in the global simulation and analysing process.

The kernel of *MBSim* was historically devoted to the analysis of rigid multibody systems explaining the program name. Now, it is able to handle arbitrary dynamical systems according to the equations in Sect. 1.2. The simulation of control, electronics, flexible bodies, hydraulics and power train systems is included within several modules. *MBSim* is based on the interface *FMatVec* [21] using either *LaPack*[3] or *ATLAS*[4] for fast evaluation of linear algebra routines. It uses *HDF5Serie* [32] to write simulation result files using the hierarchical HDF5 file format[5] even for large dynamical systems. These files can be read by *H5PlotSerie* for plotting or by *OpenMBV* [53] for visualisation. *OpenMBV* is based on the *Coin* implementation[6] of the *Open Inventor Library*[7]. A co-simulation with *MATLAB/Simulink*[8], *HySim* [55] for hydraulic components and *KetSim* [36] for camshaft timing chains is possible as well. *MBSim* is divided into a modelling part using C++ or XML and a simulation part. The simulation part is implemented completely modular distinguishing between the kinematic and kinetic update of bodies and interactions as well as integration or nonlinear solution schemes. External libraries are used where it is possible for always having a state-of-the-art numerical basis [62].

3 http://www.netlib.org/lapack/
4 http://www.netlib.org/atlas/
5 http://www.hdfgroup.org/HDF5/
6 http://www.coin3d.org/
7 http://oss.sgi.com/projects/inventor/
8 http://www.mathworks.de/

2 Model of the Pushbelt CVT

The variator model [64] is shown in Fig. 2.1.

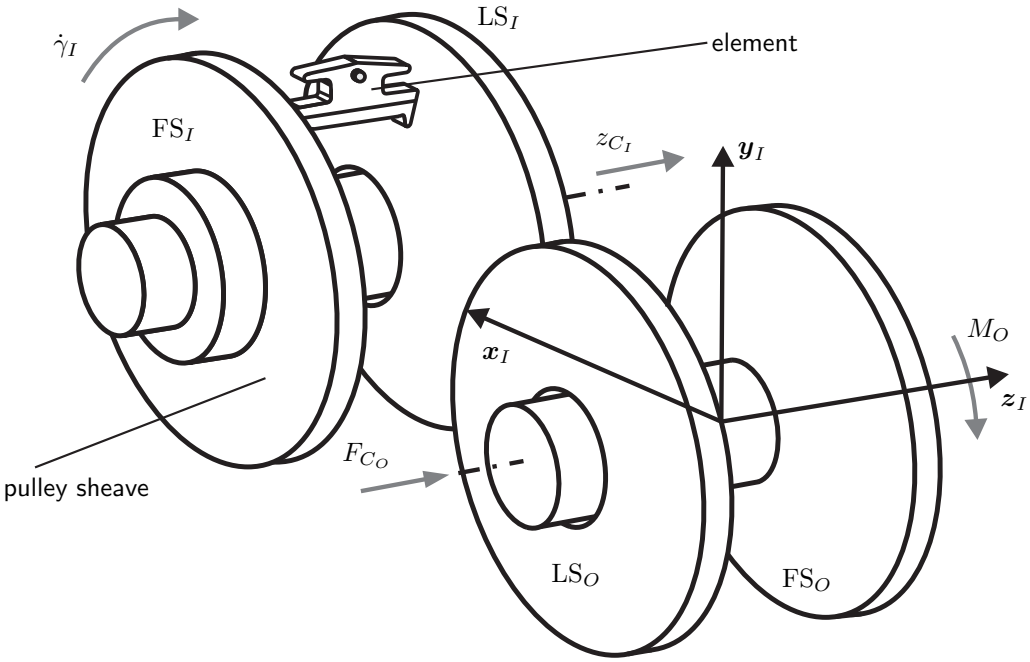

Figure 2.1: CVT with inertial frame of reference.

The inertial frame of reference of the whole CVT model is located in the centre of the output pulley (O) symmetric between the input fixed and the output fixed sheave. The $\boldsymbol{z}_I$-axis is in axial direction to the output fixed sheave, the $\boldsymbol{x}_I$-axis is perpendicular to it in direction to the input pulley (I) axis. The $\boldsymbol{y}_I$-axis completes the $\boldsymbol{x}_I$- and the $\boldsymbol{z}_I$-axis to a positive Cartesian coordinate system. Thus, the main angular motion of the pushbelt is positive around the $\boldsymbol{z}_I$-axis when it is in clockwise direction with perpendicular view to the outer side of the input fixed and the output loose sheave. Further, LS symbolises the loose and FS respectively the fixed sheave of each pulley.

2.1 Bodies

Bodies in a multibody dynamics model are characterised by inertia terms in their equations of motion. In case of the pushbelt CVT model one distinguishes between the elements, the ring packages and the pulley sheaves.

2.1.1 Elements

Altogether, N_E rigid elements with degree of freedom (dof) equal to six for translation and Cardan rotation are used for the simulation of the CVT dynamics, whereas the number of elements in reality is given by N_{E_0}. Elasticity of the elements is not regarded in the body equations of motion. Instead, it is considered within the interaction (Sect. 2.2) quasistatically because deformations only happen in case of contact and affect in a much smaller scale than global motion [63].

Figure 2.2 depicts the element shape schematically.

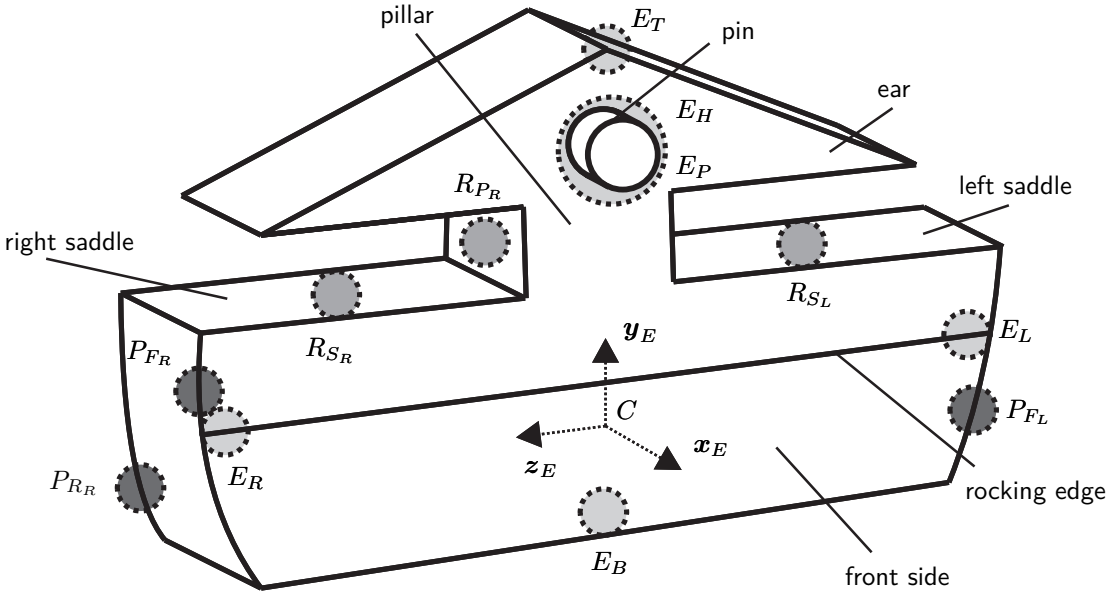

Figure 2.2: Element - three-dimensional perspective.

The element frame of reference is located in the centre of gravity C. The $\boldsymbol{x}_E$-axis is perpendicular to the planar rear side of the element and in direction to the front side. The $\boldsymbol{y}_E$-axis is perpendicular to the planar bottom of the element in direction to the top assuming that the rear side of the element is perpendicular to the bottom. The $\boldsymbol{z}_E$-axis completes the $\boldsymbol{x}_E$- and $\boldsymbol{y}_E$-axis to a positive Cartesian coordinate system.

The Newton-Euler equations of motion for a rigid body describe the internal dynamics [66].

The entire contact and visualisation geometry of the element is defined with respect to the frame of reference (Sect. 2.2). For example from the point of view of Fig. 2.2, the visible possible contact points for the element – pulley contact (P) (at the left and right front or rear side), for the element – ring package contact (R) (at the left and right saddle or pillar) as well as for the element – element contact (E) (at the top, at the left and right side of the rocking edge, at the pin and hole or at the bottom) are already indicated. In the following, the location of extremal points is

prepared. With Fig. 2.3, it holds

$$
{}_E\boldsymbol{M}_{R_P} = \begin{pmatrix} -t_S \\ h_P - h_S \\ 0 \end{pmatrix}, \quad {}_E\boldsymbol{M}_{F_P} = \begin{pmatrix} t_T - t_S \\ h_P - h_S \\ 0 \end{pmatrix}, \quad {}_E\boldsymbol{M}_{R_H} = \begin{pmatrix} -t_S \\ h_H - h_S \\ 0 \end{pmatrix},
$$

$$
{}_E\boldsymbol{M}_{F_H} = \begin{pmatrix} t_P - t_S \\ h_H - h_S \\ 0 \end{pmatrix}, \; {}_E\boldsymbol{M}_{M_{H_1}} = \begin{pmatrix} t_T - t_S \\ h_H - h_S \\ 0 \end{pmatrix}, \; {}_E\boldsymbol{M}_{M_{H_2}} = \begin{pmatrix} t_H - t_S \\ h_H - h_S \\ 0 \end{pmatrix},
$$

$$
{}_E\boldsymbol{M}_{R_S} = \begin{pmatrix} -t_S \\ 0 \\ 0 \end{pmatrix}, \qquad {}_E\boldsymbol{M}_{R_B} = \begin{pmatrix} -t_S \\ -h_S \\ 0 \end{pmatrix}, \qquad {}_E\boldsymbol{M}_{R_T} = \begin{pmatrix} -t_S \\ h_T - h_S \\ 0 \end{pmatrix},
$$

$$
{}_E\boldsymbol{E}_B = \begin{pmatrix} t_B - t_S \\ -h_S \\ 0 \end{pmatrix}, \qquad {}_E\boldsymbol{E}_T = \begin{pmatrix} t_T - t_S \\ h_T - h_S \\ 0 \end{pmatrix}
$$

with the indices characterising the rough position of the points.

It is assumed that the top edge, the ear plane and the saddle plane are parallel to the bottom and that the front is piecewise parallel to the rear side. The radii of the frustums are used in Sect. 2.2 for the explicit definition of the contact geometry.

Figure 2.4 shows the rear side of an element assuming a symmetric shape.

Then, it is

$$
{}_E\boldsymbol{C}_{R_{B_L}} = \begin{pmatrix} -t_S \\ -h_S \\ -w_B/2 \end{pmatrix}, \qquad {}_E\boldsymbol{C}_{R_{B_R}} = \begin{pmatrix} -t_S \\ -h_S \\ w_B/2 \end{pmatrix}, \qquad {}_E\boldsymbol{C}_{R_{S_L}} = \begin{pmatrix} -t_S \\ h_P - h_S \\ -w_S/2 \end{pmatrix},
$$

$$
{}_E\boldsymbol{C}_{R_{S_R}} = \begin{pmatrix} -t_S \\ h_P - h_S \\ w_S/2 \end{pmatrix}, \qquad {}_E\boldsymbol{C}^1_{R_{P_L}} = \begin{pmatrix} -t_S \\ h_P - h_S \\ -w_P/2 \end{pmatrix}, \quad {}_E\boldsymbol{C}^1_{R_{P_R}} = \begin{pmatrix} -t_S \\ h_P - h_S \\ w_P/2 \end{pmatrix},
$$

$$
{}_E\boldsymbol{C}^2_{R_{P_L}} = \begin{pmatrix} -t_S \\ h_E - h_S \\ -w_P/2 \end{pmatrix}, \qquad {}_E\boldsymbol{C}^2_{R_{P_R}} = \begin{pmatrix} -t_S \\ h_E - h_S \\ w_P/2 \end{pmatrix}, \quad {}_E\boldsymbol{C}_{R_{E_L}} = \begin{pmatrix} -t_S \\ h_E - h_S \\ -w_E/2 \end{pmatrix},
$$

$$
{}_E\boldsymbol{C}_{R_{E_R}} = \begin{pmatrix} -t_S \\ h_E - h_S \\ w_E/2 \end{pmatrix}.
$$

With $\alpha = \arctan\left(\frac{w_S - w_B}{2h_P}\right) \in \left[0, \frac{\pi}{2}\right)$ and $d_P = \sqrt{r_P^2 - h_P^2/4 - (w_S/4 - w_B/4)^2}$

$$
{}_E\boldsymbol{M}_{R_{CP_L}} = \begin{pmatrix} -t_S \\ -h_S + h_P/2 + d_P \sin\alpha \\ -w_B/4 - w_S/4 + d_P \cos\alpha \end{pmatrix},
$$

$$
{}_E\boldsymbol{M}_{R_{CP_R}} = \begin{pmatrix} -t_S \\ -h_S + h_P/2 + d_P \sin\alpha \\ w_B/4 + w_S/4 - d_P \cos\alpha \end{pmatrix}.
$$

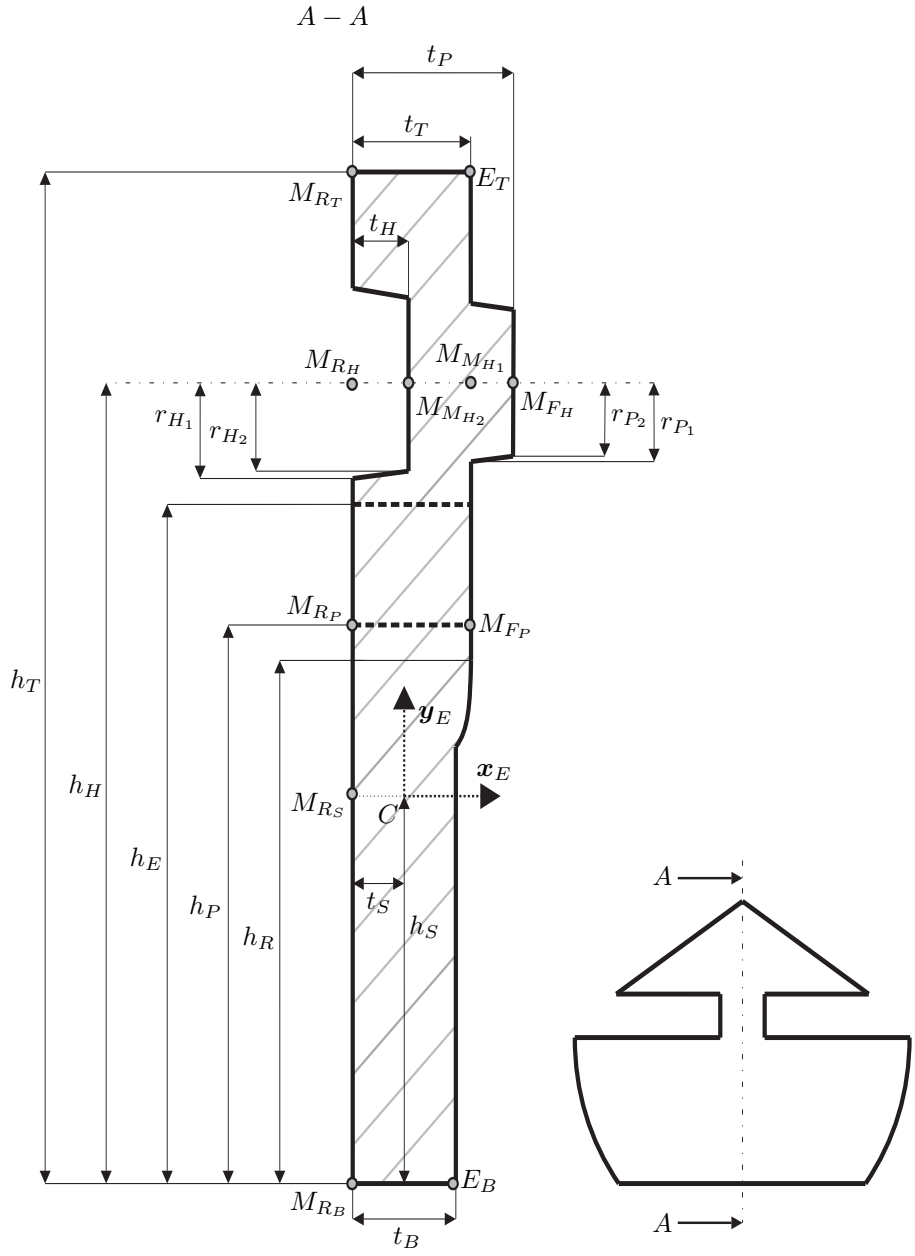

Figure 2.3: Element - perpendicular cut through centre of gravity.

Later, β is needed for the definition of the contact geometry between element and pulley (Sect. 2.2).

The front side of the element can be seen in Fig. 2.5.

This yields

$$ {}_E\boldsymbol{C}_{F_{B_L}} = \begin{pmatrix} t_B - t_S \\ -h_S \\ -w_B/2 \end{pmatrix} , \quad {}_E\boldsymbol{C}_{F_{B_R}} = \begin{pmatrix} t_B - t_S \\ -h_S \\ w_B/2 \end{pmatrix} , \quad {}_E\boldsymbol{C}_{F_{S_L}} = \begin{pmatrix} t_T - t_S \\ h_P - h_S \\ -w_S/2 \end{pmatrix} , $$

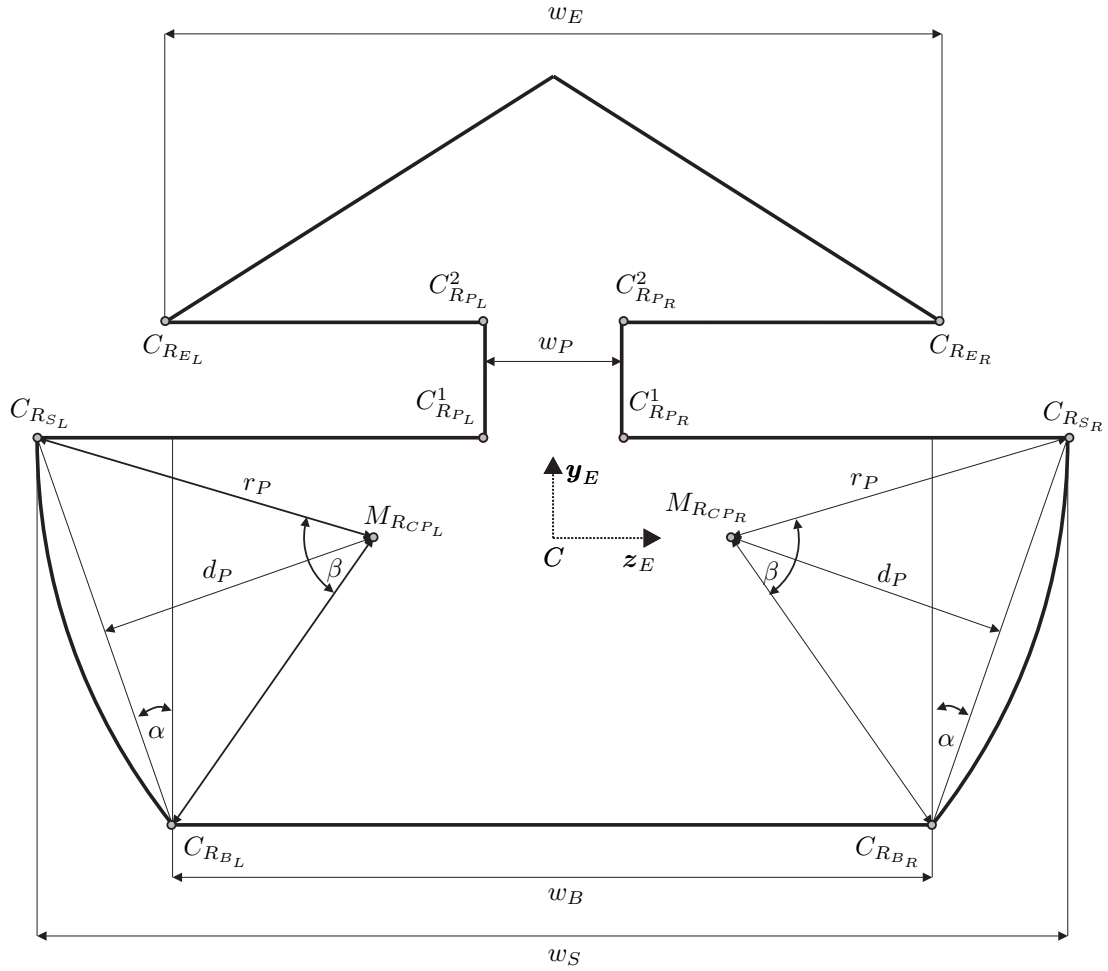

Figure 2.4: Element - rear side.

$$
{}_E\boldsymbol{C}_{F_{S_R}} = \begin{pmatrix} t_T - t_S \\ h_P - h_S \\ w_S/2 \end{pmatrix} \ , \quad {}_E\boldsymbol{C}^1_{F_{P_L}} = \begin{pmatrix} t_T - t_S \\ h_P - h_S \\ -w_P/2 \end{pmatrix} \ , \quad {}_E\boldsymbol{C}^1_{F_{P_R}} = \begin{pmatrix} t_T - t_S \\ h_P - h_S \\ w_P/2 \end{pmatrix} \ ,
$$

$$
{}_E\boldsymbol{C}^2_{F_{P_L}} = \begin{pmatrix} t_T - t_S \\ h_E - h_S \\ -w_P/2 \end{pmatrix} \ , \quad {}_E\boldsymbol{C}^2_{F_{P_R}} = \begin{pmatrix} t_T - t_S \\ h_E - h_S \\ w_P/2 \end{pmatrix} \ , \quad {}_E\boldsymbol{C}_{F_{E_L}} = \begin{pmatrix} t_T - t_S \\ h_E - h_S \\ -w_E/2 \end{pmatrix} \ ,
$$

$$
{}_E\boldsymbol{C}_{F_{E_R}} = \begin{pmatrix} t_T - t_S \\ h_E - h_S \\ w_E/2 \end{pmatrix}
$$

and

$$
{}_E\boldsymbol{C}_{F_{A_L}} = \begin{pmatrix} t_T - t_S \\ h_R - h_S \\ -w_B/2 - h_R \left(w_S - w_B\right) / \left(2h_P\right) \end{pmatrix} \ ,
$$

$$
{}_E\boldsymbol{C}_{F_{A_R}} = \begin{pmatrix} t_T - t_S \\ h_R - h_S \\ w_B/2 + h_R \left(w_S - w_B\right) / \left(2h_P\right) \end{pmatrix} \ ,
$$

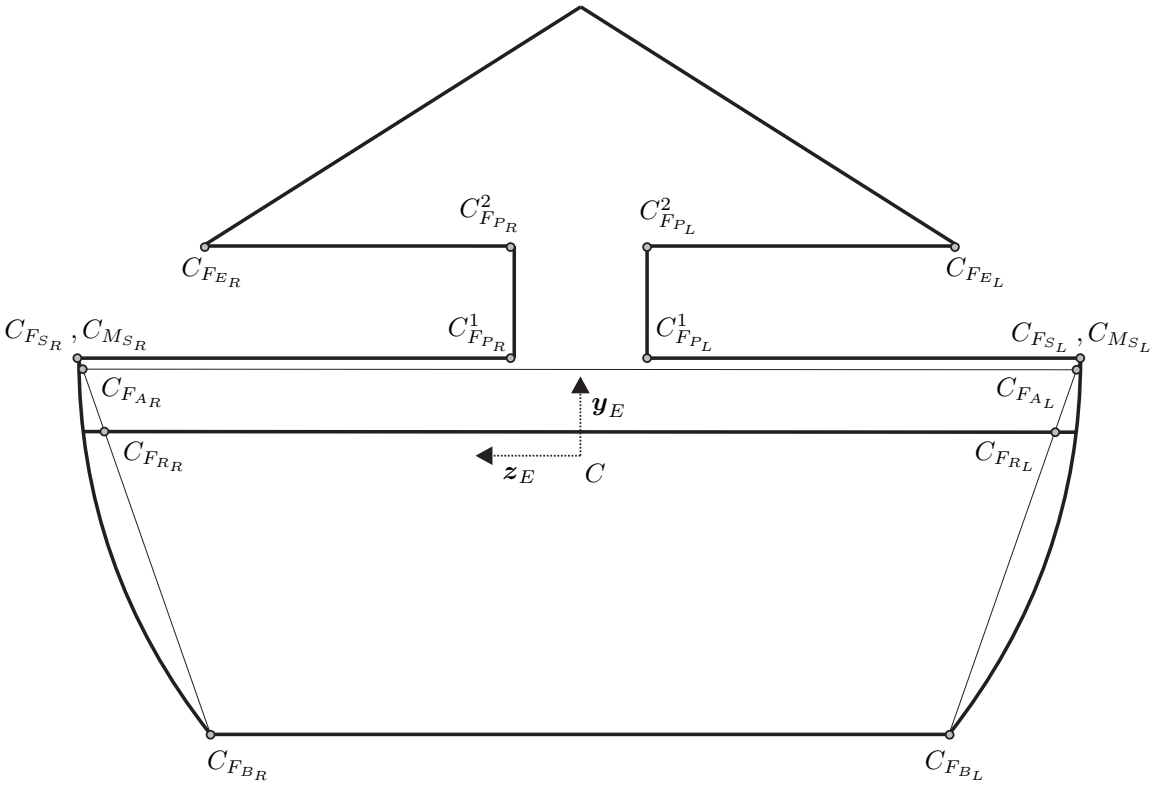

Figure 2.5: Element - front side.

$$
{}_E\boldsymbol{C}_{F_{R_L}} = {}_E\boldsymbol{C}_{F_{A_L}} + \begin{pmatrix} t_B - t_T \\ -r_R \cos\alpha \sin\gamma^* \\ r_R \sin\alpha \sin\gamma^* \end{pmatrix} ,
$$

$$
{}_E\boldsymbol{C}_{F_{R_R}} = {}_E\boldsymbol{C}_{F_{A_R}} - \begin{pmatrix} t_T - t_B \\ r_R \cos\alpha \sin\gamma^* \\ r_R \sin\alpha \sin\gamma^* \end{pmatrix}
$$

with $\gamma^* = \arccos\left(1 - \frac{t_T - t_B}{r_R}\right)$. Not explicitly visible in Fig. 2.5 are

$$
{}_E\boldsymbol{C}_{M_{S_L}} = \begin{pmatrix} t_B - t_S \\ h_P - h_S \\ -w_S/2 \end{pmatrix} , \quad {}_E\boldsymbol{C}_{M_{S_R}} = \begin{pmatrix} t_B - t_S \\ h_P - h_S \\ w_S/2 \end{pmatrix} .
$$

The parameters of the elements are summarised by:

- the mass of the element in reality m_E [kg] ,
- the entries of the inertia tensor ${}_E\boldsymbol{\Theta}_C$ in reality being defined with respect to the element frame of reference ${}_E\boldsymbol{\Theta}_{C_x}$ [kgm^2], ${}_E\boldsymbol{\Theta}_{C_y}$ [kgm^2], ${}_E\boldsymbol{\Theta}_{C_z}$ [kgm^2] ,
- the thicknesses in reality t_S [m], t_B [m], t_P [m], t_T [m], t_H [m] ,
- the heights in reality h_R [m], h_E [m], h_S [m], h_P [m], h_H [m], h_T [m] ,
- the radii in reality r_{H_1} [m], r_{H_2} [m], r_{P_1} [m], r_{P_2} [m], r_P [m], r_R [m] ,

- the widths in reality w_B [m], w_S [m], w_P [m], w_E [m] .

The effect of the change of the number of elements N_E on the above mentioned parameters has to be discussed. Main criterion is the conservation with respect to the values in reality. Defining the ratio $\iota = N_{E_0}/N_E$ yields a scaling in $\boldsymbol{x}_E$-direction and the changed "$\sim$"-parameters

$$\tilde{t}_* := \iota\, t_* \ , \tag{2.1}$$

$$\tilde{m}_E := \iota\, m_E \ , \tag{2.2}$$

$${}_E\tilde{\boldsymbol{\Theta}}_{C_x} := \iota\, {}_E\boldsymbol{\Theta}_{C_x} \ , \tag{2.3}$$

$${}_E\tilde{\boldsymbol{\Theta}}_{C_y} := 0.5 \left[\iota^3 \left({}_E\boldsymbol{\Theta}_{C_y} + {}_E\boldsymbol{\Theta}_{C_z} - {}_E\boldsymbol{\Theta}_{C_x}\right) + \iota \left({}_E\boldsymbol{\Theta}_{C_x} + {}_E\boldsymbol{\Theta}_{C_y} - {}_E\boldsymbol{\Theta}_{C_z}\right)\right] \ , \tag{2.4}$$

$${}_E\tilde{\boldsymbol{\Theta}}_{C_z} := 0.5 \left[\iota^3 \left({}_E\boldsymbol{\Theta}_{C_y} + {}_E\boldsymbol{\Theta}_{C_z} - {}_E\boldsymbol{\Theta}_{C_x}\right) + \iota \left({}_E\boldsymbol{\Theta}_{C_x} + {}_E\boldsymbol{\Theta}_{C_z} - {}_E\boldsymbol{\Theta}_{C_y}\right)\right] \tag{2.5}$$

used in the simulation by evaluating the change of the element thicknesses. Then, the inertia tensor does not represent the conservation of global parameters as it depends on ι to the power of three. Thus, an additional parameter $\tau \in [0,1]$ is introduced to finally declare the convex combinations

$${}_E\hat{\boldsymbol{\Theta}}_{C_x} := {}_E\tilde{\boldsymbol{\Theta}}_{C_x} \ , \tag{2.6}$$

$${}_E\hat{\boldsymbol{\Theta}}_{C_y} := \tau\, {}_E\tilde{\boldsymbol{\Theta}}_{C_y} + (1-\tau)\, \iota\, {}_E\boldsymbol{\Theta}_{C_y} \ , \tag{2.7}$$

$${}_E\hat{\boldsymbol{\Theta}}_{C_z} := \tau\, {}_E\tilde{\boldsymbol{\Theta}}_{C_z} + (1-\tau)\, \iota\, {}_E\boldsymbol{\Theta}_{C_z} \ . \tag{2.8}$$

A mixture of cubic and linear dependence on ι can be defined based on the users choice.

2.1.2 Ring Packages

As the entire model of the variator allows transient states, no reference path of the pushbelt and thus of the ring packages can be given. Therefore, the model of the ring packages has to cope with free spatial motions including geometrically nonlinear large translations and deflections but linear material laws. It has to be modelled dynamically because oscillations cannot be neglected [27]. As on the other hand the relative motion of the rings within the ring packages is not regarded, Fig. 2.6 shows part of a ring package homogenising $\tilde{N}_R$ rings with rectangular shaped cross-section to a one-dimensional continuum. Its motion can be described by the motion of the neutral fibre which is parametrised by the LAGRANGIAN coordinate $x \in \left[0,\, \tilde{l}_R\right]$. The normal $\boldsymbol{n}$ is pointing outwards and the tangent $\boldsymbol{t}$ is pointing along the ring circle negatively around the $\boldsymbol{z}_I$-axis. The direction of the binormal $\boldsymbol{b}$ depends on the definition of the trihedral. In this section it is assumed that the vectors are ordered as $\boldsymbol{t} - \boldsymbol{n} - \boldsymbol{b}$. The total length of the ring packages satisfies

$$\tilde{l}_R = 2\,\pi \left(\tilde{r}_R + \tilde{h}_R/2\right) \ . \tag{2.9}$$

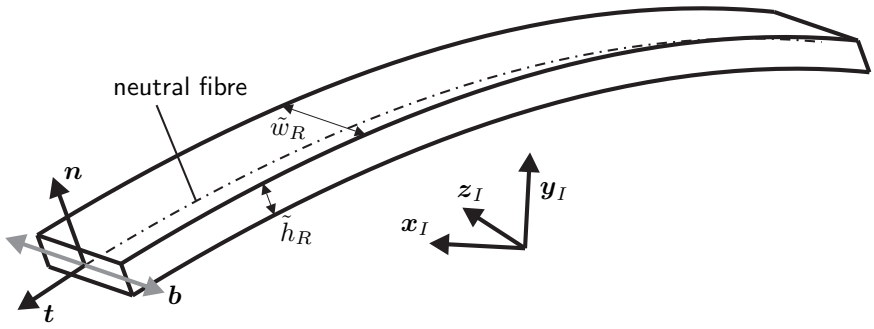

Figure 2.6: Ring package.

The radius of the inner ring circle $\tilde{r}_R$ [m] has to be adapted with N_{E_0} and the element thicknesses t_*. The height of the whole ring package $\tilde{h}_R = \tilde{N}_R \, \tilde{h}_{R_l}$ is the sum of the single ring heights $\tilde{h}_{R_l}$ [m]. It is

$$\tilde{h}_R < h_E - h_P \; . \tag{2.10}$$

For the ring width $\tilde{w}_R$ [m] holds

$$\tilde{w}_R < (w_S - w_P)/2 \; . \tag{2.11}$$

The cross-sectional area satisfies $\tilde{A}_R = \tilde{h}_R \tilde{w}_R$. The predefined curvatures for a relaxed state of the neutral fibre in the $\boldsymbol{x}_I$-$\boldsymbol{y}_I$- and in the $\boldsymbol{x}_I$-$\boldsymbol{z}_I$-planes are given by

$$\tilde{\kappa}_{1_0} = -1/\left(\tilde{r}_R + \tilde{h}_R/2\right) \; , \tag{2.12}$$

$$\tilde{\kappa}_{2_0} = 0 \; [1/\mathrm{m}] \; . \tag{2.13}$$

Young's modulus $\tilde{E}_R$ [N/m²] directly influences the numerical stiffness. Poisson's ratio $\tilde{\mu}_R$ [−] is used for the calculation of the shear modulus

$$\tilde{G}_R = \tilde{E}_R/\left(2 + 2\tilde{\mu}_R\right) \tag{2.14}$$

and $\tilde{\rho}_R$ [kg/m³] is the density. The Lehr damping values $\tilde{\vartheta}_{\tilde{\epsilon}}$ [−] for longitudinal and $\tilde{\vartheta}_{\kappa_0}$ [−] for torsional dynamics are mainly used for adaptation of the numerics. The area moments of inertia in the current $\boldsymbol{t}$-$\boldsymbol{n}$- and $\boldsymbol{t}$-$\boldsymbol{b}$-planes as well as the torsional constant [84] are given by

$$\tilde{I}_1 = \tilde{w}_R \tilde{h}_R^3/\left(12\tilde{N}_R^2\right) \; , \tag{2.15}$$

$$\tilde{I}_2 = \tilde{h}_R \tilde{w}_R^3/12 \; , \tag{2.16}$$

$$\tilde{I}_0 = 0.32 \tilde{w}_R \tilde{h}_R^3/\tilde{N}_R^2 \; . \tag{2.17}$$

They all take care of the layered structure of the ring package by summing up the area moments of inertia of the single layers and not considering interior friction.

Dividing the ring package into $\tilde{N}_B$ spatial large deformation beams (each of length

$l_0 = \tilde{l}_R/\tilde{N}_B$) provides a lot of modelling possibilities [87]. The model in [89] relies on the co-rotational approach [6, 16] and shows an efficient behaviour in the planar case compared to absolute nodal coordinate formulations [18, 29, 67]. Here, it is extended to a three-dimensional description using inertial approaches [5, 68] where the physically interpretable EULER-BERNOULLI beam formulation is used. The mathematical derivation is based on the ideas of finite element theory for assembling and multibody formulations for the evaluation of the equations of motion for each finite element [61].

Coordinate settings

The entire kinematic of one finite element can be described with a general stationary frame of reference (Fig. 2.7).

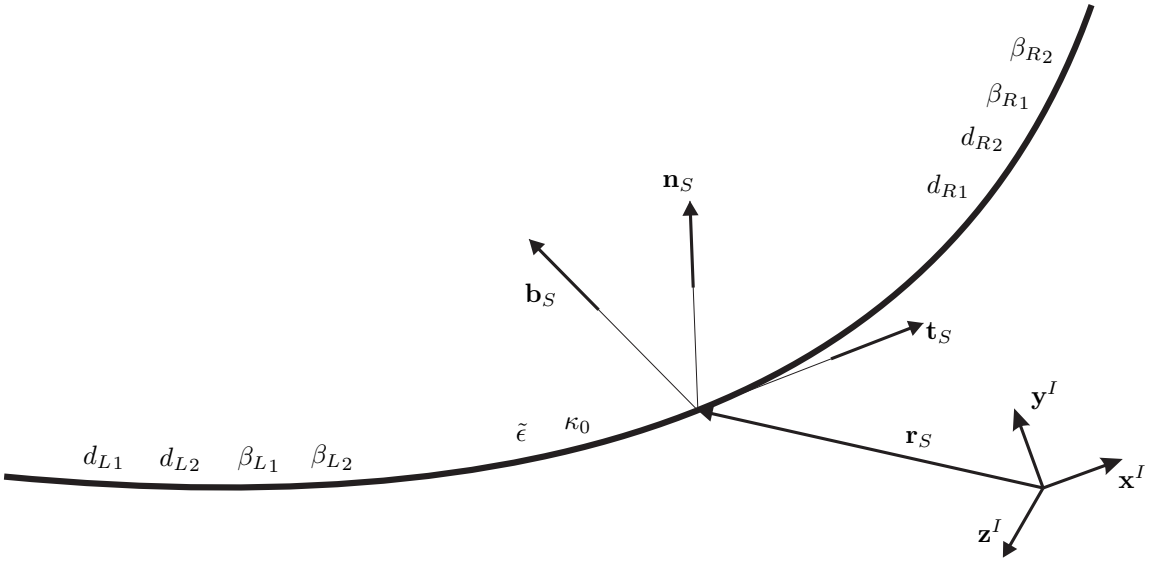

Figure 2.7: Internal coordinates.

Using a reversed Cardan parametrisation

$$\varphi_0(x) := \varphi_{S_0} + w_0'(x) \ , \ \varphi_1(x) := \varphi_{S_1} + w_1'(x) \ , \ \varphi_2(x) := \varphi_{S_2} + w_2'(x) \ , \quad (2.18)$$

a set of internal coordinates

$$\mathbf{q_i} := (x_S, y_S, z_S, \varphi_{S0}, \varphi_{S1}, \varphi_{S2}, \tilde{\epsilon}, d_{L1}, d_{R1}, \beta_{L1}, \beta_{R1}, d_{L2}, d_{R2}, \beta_{L2}, \beta_{R2}, \kappa_0)^T \quad (2.19)$$

is defined by the position vector

$$\mathbf{r}_S^T = (x_S, y_S, z_S) \quad (2.20)$$

and the angle parametrisation of the trihedral of the finite element centre as well as the longitudinal strain, the coefficients

$$w_i(-l_0/2) := d_{Li} \ , \ w_i(0) := 0 \ , \ w_i(l_0/2) := d_{Ri} \ , \ i = 1, 2 \ , \quad (2.21)$$

$$w_i^{'}\left(-l_0/2\right) := \beta_{Li}\ ,\ w_i^{'}\left(0\right) := 0\ ,\ w_i^{'}\left(l_0/2\right) := \beta_{Ri}\ ,\ i = 1, 2 \tag{2.22}$$

of the ansatz functions with the torsion

$$\kappa_0 := {}_I\mathbf{b} \cdot {}_I\mathbf{n}' = w_0^{''} - \sin\left(\varphi_{S_1}\right) w_2^{''}\ . \tag{2.23}$$

A prime denotes the derivative with respect to the LAGRANGIAN coordinate x. The degree of the real polynomials

$$w_i := a_{w_i} x^5 + b_{w_i} x^4 + c_{w_i} x^3 + d_{w_i} x^2\ ,\ i = 0, 1, 2 \tag{2.24}$$

is a compromise between too much stiffening for lower orders and too much support for higher orders with the coefficients of w_0 being constrained by the constant torsion characteristics of (2.23). In combination, rigid and elastic body motion are decoupled and a compact form of the equations of motion with appropriate approximation not depending on the boundary conditions is available for evaluation.

For coupling of finite elements the global coordinates

$$\mathbf{q}_{\mathrm{g}} := \left(x_L, y_L, z_L, \varphi_{L0}, \varphi_{L1}, \varphi_{L2}, c_{L_1}, c_{R_1}, c_{L_2}, c_{R_2}, x_R, y_R, z_R, \varphi_{R0}, \varphi_{R1}, \varphi_{R2}\right)^T \tag{2.25}$$

with

$$c_{L_1} := w_1\left(-l_0/4\right)\ ,\ c_{R_1} := w_1\left(l_0/4\right)\ , \tag{2.26}$$

$$c_{L_2} := w_2\left(-l_0/4\right)\ ,\ c_{R_2} := w_2\left(l_0/4\right) \tag{2.27}$$

are used (Fig. 2.8) to obtain equations of motion in minimal representation.

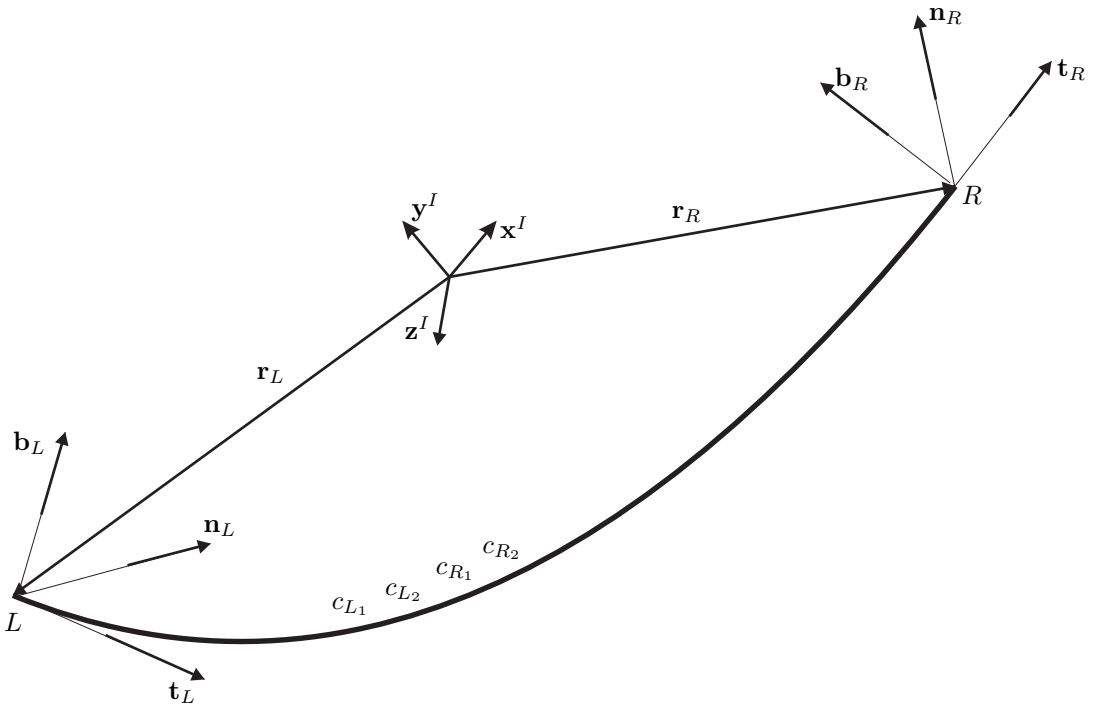

Figure 2.8: Global coordinates.

The information between the coordinate sets is transferred by the motion of the neutral fibre

$$ {}_I\mathbf{r}\left(x\right) = \left(1+\tilde{\epsilon}\right)\int {}_I\mathbf{t}\mathrm{d}x \doteq {}_I\mathbf{r}_S + \left(1+\tilde{\epsilon}\right)x\,{}_I\mathbf{t}_S + \hat{w}_1\left(x\right){}_I\mathbf{n}_S + \hat{w}_2\left(x\right){}_I\mathbf{b}_S \tag{2.28} $$

with

$$ \hat{w}_1 := \xi_{\tilde{n}} w_1 + \xi_{\tilde{b}} w_2 \ , \ \hat{w}_2 := \eta_{\tilde{n}} w_1 + \eta_{\tilde{b}} w_2 \ . \tag{2.29} $$

This results in a transformation $\mathbf{F}\left(\mathbf{q}_\mathrm{i},\mathbf{q}_\mathrm{g}\right) = \mathbf{0}$. One part can be solved analytically with respect to the internal coordinates:

$$ \begin{aligned} {}_I\mathbf{r}_S = \frac{{}_I\mathbf{r}_L + {}_I\mathbf{r}_R}{2} &- \frac{\left[\xi_{\tilde{n}}\left(d_{L_1}+d_{R_1}\right)+\xi_{\tilde{b}}\left(d_{L_2}+d_{R_2}\right)\right]{}_I\mathbf{n}_S}{2} \\ &- \frac{\left[\eta_{\tilde{n}}\left(d_{L_1}+d_{R_1}\right)+\eta_{\tilde{b}}\left(d_{L_2}+d_{R_2}\right)\right]{}_I\mathbf{b}_S}{2} \end{aligned} \tag{2.30} $$

and

$$ \tilde{\epsilon} = \frac{1}{l_0}\left({}_I\mathbf{r}_R - {}_I\mathbf{r}_L\right)\cdot {}_I\mathbf{t}_S - 1 \ , \tag{2.31} $$

$$ \kappa_0 = \frac{1}{l_0}\left[\varphi_{R_0} - \varphi_{L_0} - \sin\left(\varphi_{S_1}\right)\left(\beta_{R_2} - \beta_{L_2}\right)\right] \ . \tag{2.32} $$

A system of nonlinear equations

$$ \tilde{\mathbf{F}}_1 := \varphi_{S_0} - \frac{\varphi_{L_0}+\varphi_{R_0}}{2} + \sin\left(\varphi_{S_1}\right)\frac{\beta_{L_2}+\beta_{R_2}}{2} = 0 \ , \tag{2.33} $$

$$ \tilde{\mathbf{F}}_2 := \varphi_{S_1} - \frac{\varphi_{L_1}+\varphi_{R_1}}{2} + \frac{\beta_{L_1}+\beta_{R_1}}{2} = 0 \ , \tag{2.34} $$

$$ \tilde{\mathbf{F}}_3 := \varphi_{S_2} - \frac{\varphi_{L_2}+\varphi_{R_2}}{2} + \frac{\beta_{L_2}+\beta_{R_2}}{2} = 0 \ , \tag{2.35} $$

$$ \tilde{\mathbf{F}}_4 := \beta_{R_1} - \beta_{L_1} - \varphi_{R_1} + \varphi_{L_1} = 0 \ , \tag{2.36} $$

$$ \tilde{\mathbf{F}}_5 := \beta_{R_2} - \beta_{L_2} - \varphi_{R_2} + \varphi_{L_2} = 0 \ , \tag{2.37} $$

$$ \tilde{\mathbf{F}}_6 := \xi_{\tilde{n}}\left(d_{R_1} - d_{L_1}\right) + \xi_{\tilde{b}}\left(d_{R_2} - d_{L_2}\right) - \left({}_I\mathbf{r}_R - {}_I\mathbf{r}_L\right)\cdot {}_I\mathbf{n}_S = 0 \ , \tag{2.38} $$

$$ \tilde{\mathbf{F}}_7 := \eta_{\tilde{n}}\left(d_{R_1} - d_{L_1}\right) + \eta_{\tilde{b}}\left(d_{R_2} - d_{L_2}\right) - \left({}_I\mathbf{r}_R - {}_I\mathbf{r}_L\right)\cdot {}_I\mathbf{b}_S = 0 \ , \tag{2.39} $$

$$ \tilde{\mathbf{F}}_8 := 2b_{w_1} l_0^4/256 + 2d_{w_1} l_0^2/16 - c_{R_1} - c_{L_1} = 0 \ , \tag{2.40} $$

$$ \tilde{\mathbf{F}}_9 := 2a_{w_1} l_0^5/1024 + 2c_{w_1} l_0^3/64 - c_{R_1} + c_{L_1} = 0 \ , \tag{2.41} $$

$$ \tilde{\mathbf{F}}_{10} := 2b_{w_2} l_0^4/256 + 2d_{w_2} l_0^2/16 - c_{R_2} - c_{L_2} = 0 \ , \tag{2.42} $$

$$ \tilde{\mathbf{F}}_{11} := 2a_{w_2} l_0^5/1024 + 2c_{w_2} l_0^3/64 - c_{R_2} + c_{L_2} = 0 \tag{2.43} $$

in the unknowns $\mathbf{x}_\mathrm{be}$ remains, which can be solved with Newton's method using analytical Jacobian evaluations. The derivatives fulfill the relations

$$ \dot{\mathbf{q}}_\mathrm{i} = \frac{\mathrm{d}\mathbf{q}_\mathrm{i}}{\mathrm{d}\mathbf{q}_\mathrm{g}}\dot{\mathbf{q}}_\mathrm{g} \qquad\qquad =: \mathbf{J}_\mathrm{ig}\dot{\mathbf{q}}_\mathrm{g} \ , \tag{2.44} $$

$$\ddot{\mathbf{q}}_\mathrm{i} = \frac{\mathrm{d}}{\mathrm{d}t}\left(\frac{\mathrm{d}\mathbf{q}_\mathrm{i}}{\mathrm{d}\mathbf{q}_\mathrm{g}}\right)\dot{\mathbf{q}}_\mathrm{g} + \frac{\mathrm{d}\mathbf{q}_\mathrm{i}}{\mathrm{d}\mathbf{q}_\mathrm{g}}\ddot{\mathbf{q}}_\mathrm{g} =: \dot{\mathbf{J}}_\mathrm{ig}\dot{\mathbf{q}}_\mathrm{g} + \mathbf{J}_\mathrm{ig}\ddot{\mathbf{q}}_\mathrm{g} \tag{2.45}$$

with the expressions involving the internal coordinates $\mathbf{x}_\mathrm{be}$ being calculated by the chain rule:

$$\frac{\partial\tilde{\mathbf{F}}}{\partial\mathbf{x}_\mathrm{be}}\frac{\mathrm{d}\mathbf{x}_\mathrm{be}}{\mathrm{d}\mathbf{q}_\mathrm{g}} = -\frac{\partial\tilde{\mathbf{F}}}{\partial\mathbf{q}_\mathrm{g}}\,, \tag{2.46}$$

$$\frac{\partial\tilde{\mathbf{F}}}{\partial\mathbf{x}_\mathrm{be}}\frac{\mathrm{d}}{\mathrm{d}t}\left(\frac{\mathrm{d}\mathbf{x}_\mathrm{be}}{\mathrm{d}\mathbf{q}_\mathrm{g}}\right) = -\frac{\mathrm{d}}{\mathrm{d}t}\left(\frac{\partial\tilde{\mathbf{F}}}{\partial\mathbf{q}_\mathrm{g}}\right) - \frac{\mathrm{d}}{\mathrm{d}t}\left(\frac{\partial\tilde{\mathbf{F}}}{\partial\mathbf{x}_\mathrm{be}}\right)\frac{\mathrm{d}\mathbf{x}_\mathrm{be}}{\mathrm{d}\mathbf{q}_\mathrm{g}}\,. \tag{2.47}$$

Equations of motion

Energy expressions are the point of departure for the derivation of the equations of motion.

Mass conservation is a basic principle for the kinetic energy

$$T \approx \frac{1}{2}\tilde{\rho}_R\left[\tilde{A}_R\int\limits_{-l_0/2}^{l_0/2}\left\|{}_I\dot{\mathbf{r}}\right\|^2\mathrm{d}x + \tilde{I}_0\int\limits_{-l_0/2}^{l_0/2}\omega_t^2\mathrm{d}x\right]\,. \tag{2.48}$$

It is

$$\omega_t = \dot{\varphi}_0 - \sin\left(\varphi_1\right)\dot{\varphi}_2 \tag{2.49}$$

the projection of the angular velocity on the local tangent neglecting angular bending dependencies.

The elastic energy

$$\begin{aligned} V_e \approx{}& \frac{\tilde{E}_R\tilde{A}_R}{2}\epsilon^2 l_0 + \frac{\tilde{E}_R\tilde{I}_1}{2}\int\limits_{-l_0/2}^{l_0/2}\left(\hat{w}_1'' - \tilde{\kappa}_{1_0}\right)^2\mathrm{d}x \\ &+ \frac{\tilde{E}_R\tilde{I}_2}{2}\int\limits_{-l_0/2}^{l_0/2}\left(\hat{w}_2'' - \tilde{\kappa}_{2_0}\right)^2\mathrm{d}x + \frac{\tilde{G}_R\tilde{I}_0}{2}\int\limits_{-l_0/2}^{l_0/2}\kappa_0^2\mathrm{d}x \end{aligned} \tag{2.50}$$

results from considering at most quadratic elastic deformation terms. The bending length

$$l_b := \int\limits_{-l_0/2}^{l_0/2}\left\|{}_I\mathbf{r}'\right\|\mathrm{d}x \approx \left(1+\tilde{\epsilon}\right)l_0 + \frac{1}{2}\left[\int\limits_{-l_0/2}^{l_0/2}\hat{w}_1'\hat{w}_1'\mathrm{d}x + \int\limits_{-l_0/2}^{l_0/2}\hat{w}_2'\hat{w}_2'\mathrm{d}x\right] \tag{2.51}$$

contains second order terms concerning bending and so allows geometric nonlinear

foreshortening. The corresponding strain is given by

$$\epsilon := \frac{l_b - l_0}{l_0} \approx \tilde{\epsilon} + \frac{1}{2l_0}\left[\int_{-l_0/2}^{l_0/2} \hat{w}_1' \hat{w}_1' \mathrm{d}x + \int_{-l_0/2}^{l_0/2} \hat{w}_2' \hat{w}_2' \mathrm{d}x\right] . \tag{2.52}$$

The gravity ${}_I\mathbf{g}$ enters the gravitational energy

$$\begin{aligned} V_g &= -\tilde{\rho}_R \tilde{A}_R \, {}_I\mathbf{g} \cdot \int_{-l_0/2}^{l_0/2} {}_I\mathbf{r} \mathrm{d}x \\ &= -\tilde{\rho}_R \tilde{A}_R \, {}_I\mathbf{g} \cdot \left[l_{0I}\mathbf{r}_S + \int_{-l_0/2}^{l_0/2} \hat{w}_1 \mathrm{d}x \, {}_I\mathbf{n}_S + \int_{-l_0/2}^{l_0/2} \hat{w}_2 \mathrm{d}x \, {}_I\mathbf{b}_S \right] . \end{aligned} \tag{2.53}$$

Using the LAGRANGE II formalism

$$\frac{\mathrm{d}}{\mathrm{d}t}\left(\frac{\partial T}{\partial \dot{\mathbf{q}}_\mathrm{i}}\right)^T - \left(\frac{\partial T}{\partial \mathbf{q}_\mathrm{i}}\right)^T + \left(\frac{\partial \left(V_e + V_g\right)}{\partial \mathbf{q}_\mathrm{i}}\right)^T = \mathbf{0} \tag{2.54}$$

one derives the equations of motion. As a result of $T = T\left(\mathbf{q}_\mathrm{i}, \dot{\mathbf{q}}_\mathrm{i}\right)$ it holds

$$\frac{\mathrm{d}}{\mathrm{d}t}\left(\frac{\partial T}{\partial \dot{\mathbf{q}}_\mathrm{i}}\right)^T = \frac{\partial^2 T}{\partial \dot{\mathbf{q}}_\mathrm{i}^2}\ddot{\mathbf{q}}_\mathrm{i} + \frac{\partial^2 T}{\partial \dot{\mathbf{q}}_\mathrm{i} \partial \mathbf{q}_\mathrm{i}}\dot{\mathbf{q}}_\mathrm{i} . \tag{2.55}$$

Hence, the mass matrix and the smooth right hand side are given by

$$\mathbf{M}_\mathrm{i} := \frac{\partial^2 T}{\partial \dot{\mathbf{q}}_\mathrm{i}^2} , \quad \mathbf{h}_\mathrm{i} := \left(\frac{\partial T}{\partial \mathbf{q}_\mathrm{i}}\right)^T - \left(\frac{\partial \left(V_e + V_g\right)}{\partial \mathbf{q}_\mathrm{i}}\right)^T - \frac{\partial^2 T}{\partial \dot{\mathbf{q}}_\mathrm{i} \partial \mathbf{q}_\mathrm{i}}\dot{\mathbf{q}}_\mathrm{i} \tag{2.56}$$

such that

$$\mathbf{M}_\mathrm{i}\ddot{\mathbf{q}}_\mathrm{i} - \mathbf{h}_\mathrm{i} = \mathbf{0} . \tag{2.57}$$

Globally, the equations of motion satisfy

$$\underbrace{\mathbf{J}_\mathrm{ig}^T \mathbf{M}_\mathrm{i} \mathbf{J}_\mathrm{ig}}_{\mathbf{M}_\mathrm{g}} \ddot{\mathbf{q}}_\mathrm{g} - \underbrace{\mathbf{J}_\mathrm{ig}^T \left(\mathbf{h}_\mathrm{i} - \mathbf{M}_\mathrm{i} \dot{\mathbf{J}}_\mathrm{ig} \dot{\mathbf{q}}_\mathrm{g}\right)}_{\mathbf{h}_\mathrm{g}} = \mathbf{0} . \tag{2.58}$$

Damping

Damping terms have to be appended to the right hand side. The vector $\mathbf{h}_\mathrm{i}$ is replaced by $\mathbf{h}_\mathrm{i} + \mathbf{h}_{\mathrm{i}_D}$ with for instance

$$\mathbf{h}_{\mathrm{i}_D} := -\tilde{\epsilon}_D \dot{\tilde{\epsilon}} \mathbf{e}_7 - \kappa_{0_D} \dot{\kappa}_0 \mathbf{e}_{16} \tag{2.59}$$

and the unit vectors $\{\mathbf{e}_j\}_{j=1,\dots,16}$ considering only prolongation and torsion. The damping terms $\tilde{\epsilon}_D$, κ_{0_D} can be added directly or for easier interpretation with Lehr damping expressions $\tilde{\vartheta}_{\tilde{\epsilon}}$, $\tilde{\vartheta}_{\kappa_0}$. For prolongation or torsion only, the finite element ordinary differential equations reduce to

$$\tilde{\rho}_R \tilde{A}_R \frac{l_0^3}{12} \ddot{\tilde{\epsilon}} + \tilde{\epsilon}_D \dot{\tilde{\epsilon}} + \tilde{E}_R \tilde{A}_R l_0 \tilde{\epsilon} = 0 \ , \tag{2.60}$$

$$\tilde{\rho}_R \tilde{I}_0 \frac{l_0^3}{12} \ddot{\kappa}_0 + \kappa_{0_D} \dot{\kappa}_0 + \tilde{G}_R \tilde{I}_0 l_0 \kappa_0 = 0 \ . \tag{2.61}$$

Then with the undamped eigenfrequencies

$$\omega_{\tilde{\epsilon}} = \sqrt{\frac{12\tilde{E}_R}{\tilde{\rho}_R l_0^2}} \ , \quad \omega_{\kappa_0} = \sqrt{\frac{12\tilde{G}_R}{\tilde{\rho}_R l_0^2}} \ , \tag{2.62}$$

it is

$$\tilde{\epsilon}_D = \tilde{\rho}_R \tilde{A}_R \frac{l_0^3}{6} \tilde{\vartheta}_{\tilde{\epsilon}} \omega_{\tilde{\epsilon}} \ , \quad \kappa_{0_D} = \tilde{\rho}_R \tilde{I}_0 \frac{l_0^3}{6} \tilde{\vartheta}_{\kappa_0} \omega_{\kappa_0} \ . \tag{2.63}$$

Implicit integration

For the linear implicit integration one has to define an efficient mass matrix and an efficient right hand side. Then, the derivatives $\mathrm{d}\mathbf{h}_\mathrm{g}/\mathrm{d}\mathbf{q}_\mathrm{g}$ and $\mathrm{d}\mathbf{h}_\mathrm{g}/\mathrm{d}\dot{\mathbf{q}}_\mathrm{g}$ are necessary. The appropriate numeric calculation can be done taking advantage of the finite element structure resulting in a block-diagonal implicit integration JACOBIAN.

Assembling of the beam elements

An extended vector of global coordinates describing the whole beam structure has to be defined for coupling the finite elements:

$$\mathbf{q}_{\mathrm{g_e}} := (\dots, x_j, y_j, z_j, \varphi_{j,0}, \varphi_{j,1}, \varphi_{j,2}, c_{j,L_1}, c_{j,R_1}, c_{j,L_2}, c_{j,R_2}, x_{j+1}, \dots)^T \ . \tag{2.64}$$

The relationship between the internal coordinates of the j-th finite element and these extended global coordinates can be written as

$$\mathbf{q}_{\mathrm{i}_j} = \mathbf{Q}\left(\mathbf{q}_{\mathrm{g_e}}\right) \ . \tag{2.65}$$

Then,

$$\mathbf{J}_{\mathrm{i}_j \mathrm{g_e}} := \frac{\mathrm{d}\mathbf{q}_{\mathrm{i}_j}}{\mathrm{d}\mathbf{q}_{\mathrm{g_e}}} \tag{2.66}$$

is the JACOBIAN matrix of this transformation.

For the whole structure with $\tilde{N}_B$ finite elements, one gets a sparse system of equations which can be implemented very efficiently by index-scanning for used degrees of freedom on the global parts:

$$\underbrace{\sum_{j=1}^{\tilde{N}_B} \mathbf{J}_{\mathrm{i}_j \mathrm{g_e}}^T \mathbf{M}_{\mathrm{i}_j} \mathbf{J}_{\mathrm{i}_j g_\mathrm{e}}}_{\mathbf{M}_{\mathrm{g_e}}} \ddot{\mathbf{q}}_{\mathrm{g_e}} - \underbrace{\sum_{j=1}^{\tilde{N}_B} \mathbf{J}_{\mathrm{i}_j \mathrm{g_e}}^T \left(\mathbf{h}_{\mathrm{i}_j} - \mathbf{M}_{\mathrm{i}_j} \dot{\mathbf{J}}_{\mathrm{i}_j \mathrm{g_e}} \dot{\mathbf{q}}_{\mathrm{g_e}} \right)}_{\mathbf{h}_{\mathrm{g_e}}} = \mathbf{0} \,. \tag{2.67}$$

With (2.67), operations on zero entries can be avoided and arbitrary ring structures are represented.

2.1.3 Pulleys

Figure 2.9 shows the pulleys assembled by two rigid or elastodynamic sheaves in an undeformed configuration.

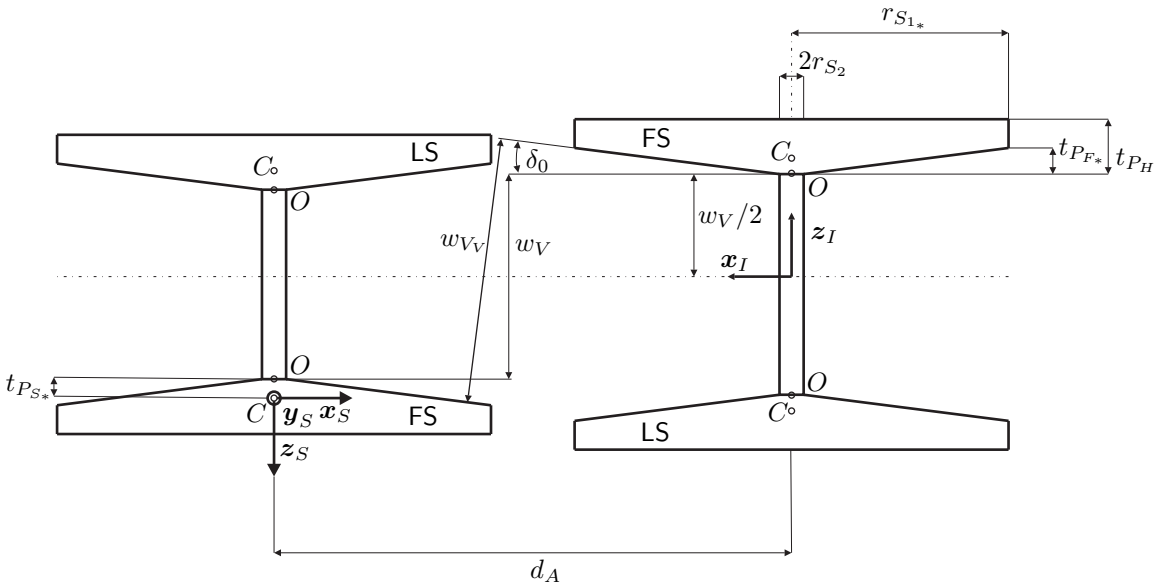

Figure 2.9: Pulleys and variator setting.

In the first case, elasticity is considered within the element interaction quasistatically and decoupled (Sect. 2.2). In the second case, the mutual influence of all the elements being in contact with one sheave is investigated in addition. As the axes of the pulleys are always considered rigid and without any inertia terms, the sheaves themselves include the respective information.

All necessary parameters for contact description (Sect. 2.2), the calculation of an initial configuration (Sect. 2.3) and visualisation are given by:

- distance of the axes d_A [m] ,
- half wedge angle δ_0 [−] ,

- widths of the variator w_{V_V} [m] and

$$w_V = -\left(d_A - 2r_{S_2}\right)\tan\left(\delta_0\right) + \frac{w_{V_V}}{\cos\left(\delta_0\right)} \ ,$$

- radii $r_{S_{1_I}}$ [m] , $r_{S_{1_O}}$ [m] and r_{S_2} [m] ,
- thicknesses t_{P_H} [m] ,

$$t_{P_{S_*}} = \frac{1}{2}\left[\frac{t_{P_{F_*}}}{3}\frac{r_{S_2} + 2r_{S_{1_*}}}{r_{S_{1_*}} + r_{S_2}} + \frac{t_{P_H} - t_{P_{F_*}}}{2}\right] \ ,$$
$$t_{P_{F_*}} = \left(r_{S_{1_*}} - r_{S_2}\right)\tan\left(\delta_0\right) \ .$$

Assuming a symmetric shape, the moving sheave frame of reference is located in the centre of gravity C of each sheave. The $\boldsymbol{z}_S$-axis is in axial direction normal to the rear side, the $\boldsymbol{y}_S$-axis is initially parallel to the $\boldsymbol{y}_I$-axis of the inertial frame of reference and the $\boldsymbol{x}_S$-axis completes a positive Cartesian coordinate system.

Rigid Sheaves

The loose sheaves (LS) have dof = 4 for axial translation, rotation and tilting as well as the fixed sheaves (FS) have dof = 1 only for axial rotation.

With

- the sheave mass m_S [kg] ,
- the inertia tensor ${}_S\Theta_C$ defined with respect to the sheave frame of reference also considering the portion of the pulley axis

the Newton-Euler equations of motion for a rigid body [66] describe the internal dynamics of each sheave.

Elastodynamic Sheaves

For elastic sheaves one has

- Young's modulus E_S [N/m²] ,
- Poisson's ratio μ_S [−] ,
- density ρ_S [kg/m³]

and the possibility to include the axis inertia contribution.

Since contacts lead to time-variant boundary conditions, the occurring small elastic deformations of the disk are modelled with local finite element shape functions [89]. The internal sheave dynamics is described only for one single finite element using

the setting from Fig. 2.10 because assembling and node condensation are canonically explained [9].

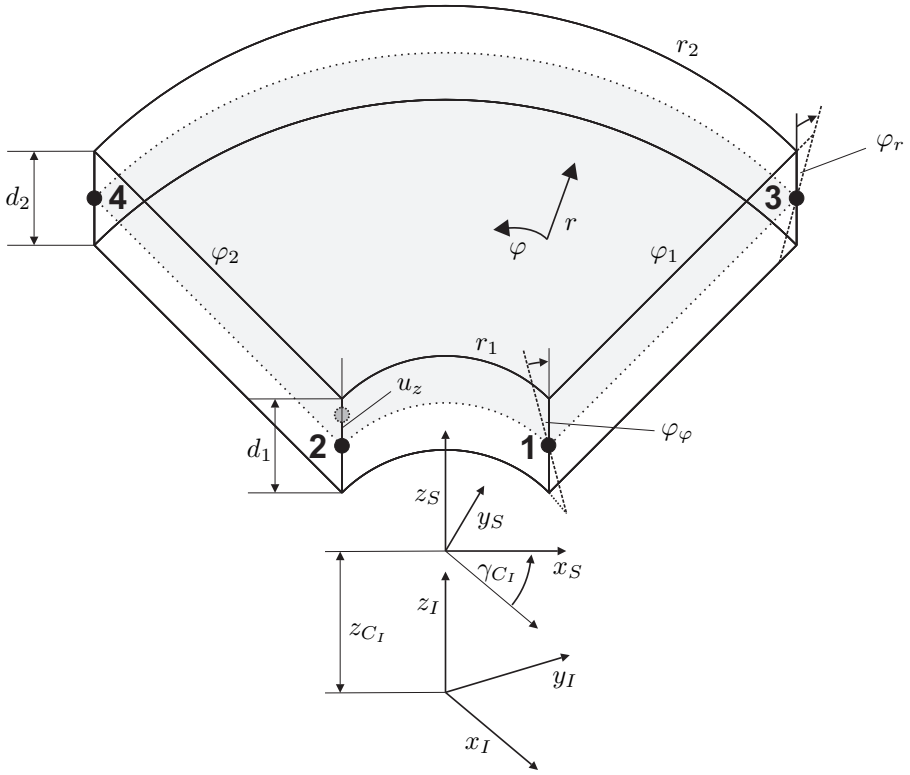

Figure 2.10: Elastodynamic sheave finite element.

Thereby, I defines an inertial frame and S the moving frame holding rigid translation z_{C_I} and rotation γ_{C_I} in direction of the sheave axis to represent sheave clamping and rotational excitation in the CVT application. Concerning the local frame S, cylindrical coordinates (r,φ,z) describing radial, azimuthal and axial principal directions are used to define an isoparametric disk. The thickness is linearly changing from d_1 at the inner radius r_1 to d_2 at the outer radius r_2 in order to capture the conical shape of the CVT sheaves and to symmetrise for the internal dynamics. The azimuthal dimension and position are defined by φ_1 and φ_2 in mathematically positive direction. The finite element nodes are located at the midplane and numbered from 1 to 4. Starting from linear elastic continuum mechanics with homogeneous and isotropic material, the assumptions of Reissner/Mindlin [91] are the basis for the description of a fairly thick structure in comparison to Kirchhoff theory. Another advantage of a Reissner/Mindlin plate is the possible usage of globally continuous instead of globally continuously differentiable shape functions. In detail, one has the following six assumptions:

1. plane stress ,
2. plane mid-surface ,
3. constant density ρ_S ,

4. no dependency of the local u_z displacement on z,
5. planar cross-sections remain planar ,
6. external forces only normal to mid-surface .

Then, one gets for the local displacements

$$u_r(r,\varphi,z) = z\,\varphi_r\,(r,\varphi)\ , \tag{2.68}$$
$$u_\varphi(r,\varphi,z) = -z\,\varphi_\varphi\,(r,\varphi)\ , \tag{2.69}$$
$$u_z(r,\varphi,z) = u_z\,(r,\varphi) \tag{2.70}$$

with φ_r, φ_φ and u_z being unknown functions of the tilting cross-section around the midplane and of the axial translational deformation.

The co-rotational coordinate contribution

$$\boldsymbol{q}^T = \left(\boldsymbol{q}_r^T\ ,\ \boldsymbol{q}_e^T\right) \tag{2.71}$$

of each finite element to the assembled differential equations can be classified into rigid body coordinates $\boldsymbol{q}_r$ being the same for all finite elements and elastic coordinates $\boldsymbol{q}_e$ [66]. The related substructures can be seen in the derivation of the system matrices in the following sections.

Finite element stiffness matrix: The reduction of the stationary continuum mechanics equations yields transverse forces and bending moments

$$\boldsymbol{s} = \begin{pmatrix} s_r \\ s_\varphi \end{pmatrix} = \boldsymbol{D}_s\boldsymbol{\gamma}\ , \tag{2.72}$$
$$\boldsymbol{m} = \begin{pmatrix} m_r \\ m_\varphi \\ m_{r\varphi} \end{pmatrix} = \boldsymbol{D}_m\boldsymbol{\kappa} \tag{2.73}$$

with shear and bending strains as well as corresponding constitutive transformation matrices

$$\boldsymbol{\gamma} = \begin{pmatrix} \gamma_r \\ \gamma_\varphi \end{pmatrix} = \begin{pmatrix} \varphi_r + \frac{\partial u_z}{\partial r} \\ -\varphi_\varphi + \frac{1}{r}\frac{\partial u_z}{\partial \varphi} \end{pmatrix}\ , \tag{2.74}$$
$$\boldsymbol{\kappa} = \begin{pmatrix} \kappa_r \\ \kappa_\varphi \\ \kappa_{r\varphi} \end{pmatrix} = \begin{pmatrix} \frac{\partial \varphi_r}{\partial r} \\ \frac{1}{r}\left(\varphi_r - \frac{\partial \varphi_\varphi}{\partial \varphi}\right) \\ \frac{1}{2}\left(-\frac{\partial \varphi_\varphi}{\partial r} + \frac{1}{r}\left(\frac{\partial \varphi_r}{\partial \varphi} + \varphi_\varphi\right)\right) \end{pmatrix}\ , \tag{2.75}$$
$$\boldsymbol{D}_s = G_S\,d\,\sigma_e \begin{pmatrix} 1 & 0 \\ 0 & 1 \end{pmatrix}\ , \tag{2.76}$$
$$\boldsymbol{D}_m = K_S \begin{pmatrix} 1 & \mu_S & 0 \\ \mu_S & 1 & 0 \\ 0 & 0 & 1-\mu_S \end{pmatrix} \tag{2.77}$$

appearing at the right hand sides. Thereby,

$$d = d\,(r) = \frac{d_2 - d_1}{r_2 - r_1}\,(r - r_1) + d_1 \tag{2.78}$$

is the radially varying thickness of the plate, G_S the shear modulus and

$$\sigma_e = \begin{cases} \sigma\ , & \text{if } \bar{d}/l_e \geq \Upsilon\ , \\ \sigma\left(\frac{\bar{d}}{l_e \Upsilon}\right)^2\ , & \text{if } \bar{d}/l_e < \Upsilon \end{cases} \tag{2.79}$$

an artificial finite element shear correction factor. It accounts for non-uniform distributions of transverse shear strains in local z-direction. The values $\sigma = 5/6$ according to REISSNER and $\sigma = \pi^2/12$ according to MINDLIN are historically motivated. The correction using the mean value of the thickness $\bar{d}$, the element diameter l_e and a numerical parameter $\Upsilon > 0$ introduces a virtual thicker plate if numerically necessary (p. 33). Further, it holds

$$K_S = \frac{E_S\, d^3}{12\,(1 - \mu_S^2)}\ . \tag{2.80}$$

According to the LAGRANGE II formalism (2.54), the internal right hand side of the equations of motion is given by the derivative of the potential energy with respect to the generalised coordinates. Neglecting the gravitational potential, the elastic potential

$$\begin{aligned} V_e &= \frac{1}{2}\left[\int_{\varphi_1}^{\varphi_2}\int_{r_1}^{r_2} \boldsymbol{\gamma}\cdot\boldsymbol{s}\, r\mathrm{d}r\mathrm{d}\varphi + \int_{\varphi_1}^{\varphi_2}\int_{r_1}^{r_2} \boldsymbol{\kappa}\cdot\boldsymbol{m}\, r\mathrm{d}r\mathrm{d}\varphi\right] \\ &= \frac{1}{2}\left[\int_{\varphi_1}^{\varphi_2}\int_{r_1}^{r_2} \boldsymbol{\gamma}\cdot\boldsymbol{D}_s\boldsymbol{\gamma}\, r\mathrm{d}r\mathrm{d}\varphi + \int_{\varphi_1}^{\varphi_2}\int_{r_1}^{r_2} \boldsymbol{\kappa}\cdot\boldsymbol{D}_m\boldsymbol{\kappa}\, r\mathrm{d}r\mathrm{d}\varphi\right] \end{aligned} \tag{2.81}$$

is a quadratic function of the strains. After discretisation

$$\varphi_r^h = \sum_j h_j\, \varphi_{rj}\ , \tag{2.82}$$

$$\varphi_\varphi^h = \sum_j h_j\, \varphi_{\varphi j}\ , \tag{2.83}$$

$$u_z^h = \sum_j h_j\, u_{zj} + h_{r,j}\, \varphi_{r_j} + h_{\varphi,j}\, \varphi_{\varphi_j} \tag{2.84}$$

with bilinear $\{h_j\}_j$ as well as biquadratic $\{h_{r,j}\}_j$, $\{h_{\varphi,j}\}_j$ finite element shape functions and nodal coordinates $\left\{\varphi_{rj}\right\}_j$, $\left\{\varphi_{\varphi j}\right\}_j$, $\left\{u_{zj}\right\}_j$ (p. 33), the energy functional preserves its structure with a constant finite element stiffness matrix $\boldsymbol{K}_e$:

$$V_e = \frac{1}{2}\boldsymbol{q}_e \cdot \boldsymbol{K}_e \boldsymbol{q}_e\ . \tag{2.85}$$

Finite element mass matrix: The kinetic energy

$$T = \frac{\rho_S}{2} \int\limits_V \left({}_I\dot{\boldsymbol{X}} + \boldsymbol{Q}_{IS} \left({}_S\boldsymbol{\omega} \times_S \boldsymbol{r} \right) \right) \cdot \left({}_I\dot{\boldsymbol{X}} + \boldsymbol{Q}_{IS} \left({}_S\boldsymbol{\omega} \times_S \boldsymbol{r} \right) \right) \mathrm{d}V \tag{2.86}$$

is structurally an integral of the squared plate velocity norm distribution in the inertial frame with respect to the finite element volume V. Thereby,

$$\boldsymbol{Q}_{IS} = \begin{pmatrix} \cos\left(\gamma_{C_I}\right) & -\sin\left(\gamma_{C_I}\right) & 0 \\ \sin\left(\gamma_{C_I}\right) & \cos\left(\gamma_{C_I}\right) & 0 \\ 0 & 0 & 1 \end{pmatrix} \tag{2.87}$$

is the rigid body transformation matrix between the inertial and the moving frame and

$${}_I\boldsymbol{X} = \begin{pmatrix} 0 \\ 0 \\ z_{C_I} \end{pmatrix} + \boldsymbol{Q}_{IS} \begin{pmatrix} r\cos\varphi \\ r\sin\varphi \\ u_z \end{pmatrix} \tag{2.88}$$

is the parametrised location of the midplane points resulting in

$${}_I\dot{\boldsymbol{X}} = \begin{pmatrix} -\dot{\gamma}_{C_I}\, r \sin\left(\gamma_{C_I} + \varphi\right) \\ \dot{\gamma}_{C_I}\, r \cos\left(\gamma_{C_I} + \varphi\right) \\ \dot{u}_z + \dot{z}_{C_I} \end{pmatrix} . \tag{2.89}$$

The angular velocity is given by

$${}_S\boldsymbol{\omega} = \begin{pmatrix} 0 \\ 0 \\ \dot{\gamma}_{C_I} \end{pmatrix} + \begin{pmatrix} \cos\varphi & -\sin\varphi & 0 \\ \sin\varphi & \cos\varphi & 0 \\ 0 & 0 & 1 \end{pmatrix} \begin{pmatrix} \dot{\varphi}_\varphi \\ \dot{\varphi}_r \\ 0 \end{pmatrix} \tag{2.90}$$

and the local translational parametrisation fulfills

$${}_S\boldsymbol{r}^T = (0, 0, z) \ . \tag{2.91}$$

With the plate symmetry assumption, the kinetic energy can be splitted in a translational and a rotational component

$$T_{\mathrm{trans}} = \frac{\rho_S}{2} \int\limits_V {}_I\dot{\boldsymbol{X}} \cdot {}_I\dot{\boldsymbol{X}} \ \mathrm{d}V = \frac{\rho_S}{2} \int\limits_{\varphi_1}^{\varphi_2} \int\limits_{r_1}^{r_2} \left(\dot{\gamma}_{C_I}^2\, r^2 + \left(\dot{u}_z + \dot{z}_{C_I} \right)^2 \right) d\, r \, \mathrm{d}r\mathrm{d}\varphi \ , \tag{2.92}$$

$$\begin{aligned} T_{\mathrm{rot}} &= \frac{\rho_S}{2} \int\limits_V \left(\boldsymbol{Q}_{IS} \left({}_S\boldsymbol{\omega} \times_S \boldsymbol{r} \right) \right) \cdot \left(\boldsymbol{Q}_{IS} \left({}_S\boldsymbol{\omega} \times_S \boldsymbol{r} \right) \right) \mathrm{d}V \\ &= \frac{\rho_S}{24} \int\limits_{\varphi_1}^{\varphi_2} \int\limits_{r_1}^{r_2} \left(\omega_2^2 + \omega_1^2 \right) d^3\, r \, \mathrm{d}r\mathrm{d}\varphi = \frac{\rho_S}{24} \int\limits_{\varphi_1}^{\varphi_2} \int\limits_{r_1}^{r_2} \left(\dot{\varphi}_\varphi^2 + \dot{\varphi}_r^2 \right) d^3\, r \, \mathrm{d}r\mathrm{d}\varphi \ . \end{aligned} \tag{2.93}$$

Discovering that there are only quadratic terms and no dependencies on the positions, one obtains after discretisation

$$T = \frac{1}{2}\dot{\boldsymbol{q}} \cdot \boldsymbol{M}\dot{\boldsymbol{q}} \tag{2.94}$$

with a constant finite element mass matrix $\boldsymbol{M}$. The only structural difference to the finite element stiffness matrix is that the kinetic energy not only contributes to the elastic but also to the rigid body coordinates.

Extensions for a robust integration: It is well-known that the standard Reissner/Mindlin plate model might induce shear locking effects during simulation [9]. These appear both mathematically in not uniform convergence concerning a critical parameter in the Céa lemma and mechanically in a too stiff behaviour in comparison to an exact reference solution applying patch tests.

Mixed finite element schemes based on the Hu-Washizu functional and the inf-sup condition evaluated for example by singular value calculations are a possibility to analyse and avoid locking of conform finite elements. These finite elements are more complicated and it is often possible to achieve a more robust but probably not locking-free behaviour by adaptation of the conform finite element scheme, as well. Such an idea is followed up by extending standard bilinear ansatz functions with biquadratic ones for a better representation of the bending modes but by also preserving the overall degree of freedom with additional constraints [37]. Further, the shear correction factor is adjusted to the specific finite element sizes and a selective integration is chosen. Altogether, this approach yields an admissible and effective improvement for a lot of practical applications and can also be used in the above situation.

2.2 Interactions

External borders, joints and contacts belong to interactions. A joint constraints two bodies bilaterally at a fixed point relative to the respective body without defining friction. With contacts even friction can be set and moveable points of reference are possible. For efficiency, the number of contacts should be minimised.

2.2.1 Pulley – Environment Interaction

For the output pulley, a kinetic excitation

$$\boldsymbol{L}_O = \begin{pmatrix} F_{CO} \\ M_O \end{pmatrix} \tag{2.95}$$

(Fig. 2.1) representing the clamping force and the load torque by linear interpolation of a time table is provided.

For the input pulley, the rotational setting is always done by the angular velocity $\dot{\gamma}_I$. As the position is given by initialisation, the clamping velocity $\dot{z}_{C_I}$ is defined. Again, both values are given by linear interpolation of time tables.

In the case of rigid pulleys, a linearly flexible joint is defined for the two tilting directions of the respective loose sheaves.

2.2.2 Sheave – Sheave Joint

The interface between a fixed and a loose sheave is defined by a translational joint ensuring the same angular velocity.

2.2.3 Element – Pulley Contacts

The interaction laws and contact kinematics have to be distinguished according to the different sheave models representing elasticity. Though, in both cases the normal contact law is unilateral and linearly flexible representing the axial stiffness of the elements. Friction is described by a three-dimensional STRIBECK-law. The friction coefficient is given by

$$\mu_P\left(\dot{\boldsymbol{g}}_{P_T}\right) := \mu_{P_0} + \frac{\mu_{P_1}}{1 + \mu_{P_2}\left\|\dot{\boldsymbol{g}}_{P_T}\right\|^{k_P}} \tag{2.96}$$

with the relative tangential velocity $\dot{\boldsymbol{g}}_{P_T}$ and the parameter values μ_{P_0} [−], μ_{P_1} [−], μ_{P_2} $\left[{}^{\mathrm{s}^{\mathrm{k_P}}}/_{\mathrm{m}^{\mathrm{k_P}}}\right]$ as well as k_P [−]. Furthermore, the element geometry remains the same. In order to simplify contact geometries and to allow for future developments, the shape of the left and right body side of the elements are described by two circular arcs, respectively, neglecting the influence of the rocking edge (Fig. 2.2). The contour points of the element are given by

$${}_E\boldsymbol{P}_{R_L} = {}_E\boldsymbol{M}_{R_{CP_L}} + r_P \begin{pmatrix} 0 \\ \sin(\beta-\alpha) \\ -\cos(\beta-\alpha) \end{pmatrix}, \quad {}_E\boldsymbol{P}_{F_L} = {}_E\boldsymbol{P}_{R_L} + \begin{pmatrix} t_B \\ 0 \\ 0 \end{pmatrix}, \tag{2.97}$$

$${}_E\boldsymbol{P}_{R_R} = {}_E\boldsymbol{M}_{R_{CP_R}} + r_P \begin{pmatrix} 0 \\ -\sin(\alpha-\beta) \\ \cos(\alpha-\beta) \end{pmatrix}, \quad {}_E\boldsymbol{P}_{F_R} = {}_E\boldsymbol{P}_{R_R} + \begin{pmatrix} t_B \\ 0 \\ 0 \end{pmatrix} \tag{2.98}$$

with

$$\beta \in [-\arccos(d_P/r_P), \arccos(d_P/r_P)] \tag{2.99}$$

being the contour parameter. The undeformed sheaves have always frustum contours. Thus, the contact points are at least assumed to be uniquely given and to characterise

three-dimensional motion of the elements even clamping between the sheaves and friction torques.

Rigid Sheaves

For each sheave, one has to parametrise the frustum contour:

$$ {}_S\boldsymbol{S}_F\,(z,\gamma) = \begin{pmatrix} r_{S_2}\cos\gamma + z\frac{r_{S_{1*}}-r_{S_2}}{t_{P_{F_*}}}\cos\gamma \\ r_{S_2}\sin\gamma + z\frac{r_{S_{1*}}-r_{S_2}}{t_{P_{F_*}}}\sin\gamma \\ -t_{P_{S_*}} + z \end{pmatrix} \tag{2.100} $$

with $z \in \left[0,t_{P_{F_*}}\right]$ and $\gamma \in [0,2\pi)$.

As the contact configuration between circle and frustum also occurs between adjacent elements at pin and hole, a general description follows.

First, it is roughly checked if contact is possible. A sphere is defined by the circle being its midplane and the frustum is estimated by a sphere from inside or from outside depending on the contact cases distinguished below. The distance in-between these spheres is evaluated. If the distance is below a threshold, the following detailed calculation is carried out.

A circle is given by its centre ${}_I\boldsymbol{M}_C$, a radius r_C and a binormal ${}_I\boldsymbol{b}_C$. A frustum is defined by the normed axis $\boldsymbol{a}_F$, the radii r_{F_1} and r_{F_2} in direction to the axis, the height h_F, the half apex angle

$$ \varphi_F := \arctan\left(\frac{r_{F_2}-r_{F_1}}{h_F}\right)\,, \tag{2.101} $$

and a starting point ${}_I\boldsymbol{P}_F$ at the centre of the bottom. The contact configuration in-between can be declared by root functions based on minimising problems or orthogonality relations as well as conic section theory [33]. In the following, conic section theory is discussed considering the different contact configurations.

Outer side of the circle and inner side of the frustum: First, it is checked if the kinematics can be simplified. One can consider a degenerated but probably interesting circle-to-circle contact if ${}_I\boldsymbol{a}_F$ is parallel to ${}_I\boldsymbol{b}_C$ so if $\| {}_I\boldsymbol{z}_{CF} \| = 0$ with

$$ t_{CF} := {}_I\boldsymbol{a}_F \cdot {}_I\boldsymbol{b}_C\,, \tag{2.102} $$

$$ {}_I\boldsymbol{z}_{CF} := {}_I\boldsymbol{b}_C - t_{CF}\,{}_I\boldsymbol{a}_F\,. \tag{2.103} $$

Then with the radius

$$ r_{F_h} = r_{F_1} + \frac{r_{F_2}-r_{F_1}}{h_F}u_{CF}, \quad u_{CF} := {}_I\boldsymbol{a}_F \cdot {}_I\boldsymbol{d}_{CF}\,, \quad {}_I\boldsymbol{d}_{CF} = {}_I\boldsymbol{M}_C - {}_I\boldsymbol{P}_F \tag{2.104} $$

of the affected frustum circle, the normal distance is given by

$$g_{CF} = [r_{F_h} - r_C - \| {}_I\boldsymbol{c}_{CF} \|] \cos(\varphi_F) , \quad {}_I\boldsymbol{c}_{CF} := {}_I\boldsymbol{d}_{CF} - u_{CF}\, {}_I\boldsymbol{a}_F \ . \tag{2.105}$$

The last and the next calculations are only relevant if $0 \leq u_{CF} \leq h_F$. As g_{CF} can be computed very early in this case, it can be used to identify open contacts $g_{CF} > 0$. If $\| {}_I\boldsymbol{c}_{CF} \| = 0$, there is an infinite number of possible contact points. Otherwise, the contact normal of the frustum is given by

$${}_I\boldsymbol{n}_F = \sin(\varphi_F)\, {}_I\boldsymbol{a}_F - \cos(\varphi_F) \frac{{}_I\boldsymbol{c}_{CF}}{\| {}_I\boldsymbol{c}_{CF} \|} \ . \tag{2.106}$$

If $\| {}_I\boldsymbol{z}_{CF} \| \neq 0$, the contact situation can be reduced to the contact between a circle and a cone section, especially an ellipse or hyperbola. The parabola case occurs only for single points (Fig. 2.11).

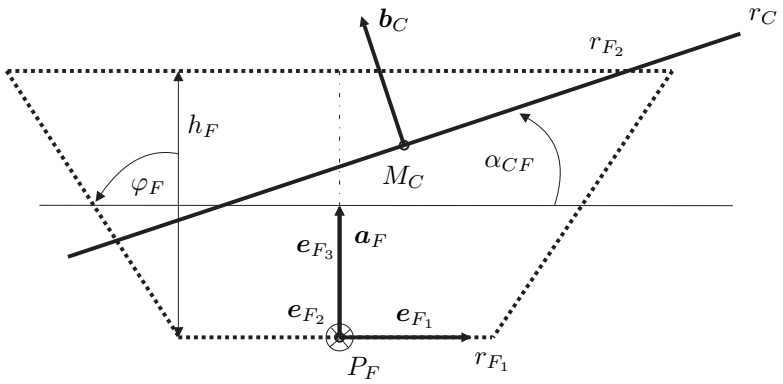

Figure 2.11: Frustum-to-circle contact.

However first, one recognises that the binormal of the circle is only given except for the sign. Hence without restriction, it is assumed that $t_{CF} \geq 0$. Otherwise, ${}_I\boldsymbol{b}_C$ can be multiplied by -1. Then with

$$\alpha_{CF} = \arccos(t_{CF}) \in [0,\pi/2] \tag{2.107}$$

and

$${}_I\boldsymbol{e}_{F_3} = {}_I\boldsymbol{a}_F \ , \ \ {}_I\boldsymbol{e}_{F_1} = -\frac{{}_I\boldsymbol{z}_{CF}}{\| {}_I\boldsymbol{z}_{CF} \|}, \ \ {}_I\boldsymbol{e}_{F_2} = {}_I\boldsymbol{e}_{F_3} \times {}_I\boldsymbol{e}_{F_1} \ , \tag{2.108}$$

the plane of the circle can be defined by an equation in the frustum's frame of reference

$$z = [x - \xi_1] \tan(\alpha_{CF}) + \xi_2 \ . \tag{2.109}$$

Thereby, $\xi_1 := {}_I\boldsymbol{d}_{CF} \cdot {}_I\boldsymbol{e}_{F_1}$ and $\xi_2 := {}_I\boldsymbol{d}_{CF} \cdot {}_I\boldsymbol{e}_{F_3}$. Contact of the plane with the frustum must only be tested if

$$-\sin(\alpha_{CF})\, r_C < \xi_2 < h_F + \sin(\alpha_{CF})\, r_C \ . \tag{2.110}$$

The frustum can be parametrised by

$$x := r_{F_h} \cos(\Psi_F), \quad y := r_{F_h} \sin(\Psi_F), \quad r_{F_h} := r_{F_1} + \tan(\varphi_F)\, z \tag{2.111}$$

with the circular $\Psi_F \in [0,2\pi]$ and the axial $z \in [0,h_F]$ contour parameters of the frustum. Then, the conic section is given by

$$x = \frac{p \cos(\Psi_F)}{1 - \cos(\Psi_F)\, q}\,, \tag{2.112}$$

$$y = \frac{p \sin(\Psi_F)}{1 - \cos(\Psi_F)\, q}\,, \tag{2.113}$$

$$z = \frac{1}{\tan(\varphi_F)} \left[\frac{p}{1 - \cos(\Psi_F)\, q} - r_{F_1} \right] \tag{2.114}$$

with

$$p := r_{F_1} + \tan(\varphi_F) \left[\xi_2 - \tan(\alpha_{CF})\, \xi_1 \right]\,, \tag{2.115}$$

$$q := \tan(\varphi_F) \tan(\alpha_{CF})\,. \tag{2.116}$$

This conic section defines part of an ellipse for $|q| < 1$ and part of a hyperbola for $|q| > 1$. Thus by additionally excluding the cylinder ($\tan(\varphi_F) \neq 0$) and assuming a full intersection, it is possible to define the centre and the semi-major as well as the semi-minor axis using the definition of r_{F_h}:

$${}_I\boldsymbol{M}_{CS} := {}_I\boldsymbol{P}_F + \frac{pq}{1-q^2}\, {}_I\boldsymbol{e}_{F_1} + \frac{1}{\tan(\varphi_F)} \left[\frac{p}{1-q^2} - r_{F_1} \right] {}_I\boldsymbol{e}_{F_3}\,, \tag{2.117}$$

$${}_I\boldsymbol{c}^*_{CS_1} := \frac{p}{1-q^2}\, {}_I\boldsymbol{e}_{F_1} + \frac{1}{\tan(\varphi_F)} \frac{pq}{1-q^2}\, {}_I\boldsymbol{e}_{F_3}\,, \tag{2.118}$$

$${}_I\boldsymbol{c}^*_{CS_2} := \frac{|p|}{\sqrt{|1-q^2|}}\, {}_I\boldsymbol{e}_{F_2}\,. \tag{2.119}$$

For a hyperbola, the transverse and imaginary axes are only defined except for the sign. The correct sign has to be chosen according to the affected cone comparing the z-values of the hyperbola peaks. For the ellipse nothing has to be changed. This results in

$${}_I\boldsymbol{c}^*_{E_1} = {}_I\boldsymbol{c}^*_{CS_1}\,, \qquad {}_I\boldsymbol{c}^*_{E_2} = {}_I\boldsymbol{c}^*_{CS_2}\,, \tag{2.120}$$

$${}_I\boldsymbol{c}^*_{H_1} = \frac{-pq}{|pq|}\, {}_I\boldsymbol{c}^*_{CS_1}\,, \qquad {}_I\boldsymbol{c}^*_{H_2} = \frac{-pq}{|pq|}\, {}_I\boldsymbol{c}^*_{CS_2}\,. \tag{2.121}$$

With the definitions from above, the ellipse and hyperbola are given by

$${}_I\boldsymbol{E}(\rho) = {}_I\boldsymbol{M}_E + \cos\rho\, {}_I\boldsymbol{c}^*_{E_1} + \sin\rho\, {}_I\boldsymbol{c}^*_{E_2}\,, \tag{2.122}$$

$${}_I\boldsymbol{H}(\rho) = {}_I\boldsymbol{M}_H + \cosh\rho\, {}_I\boldsymbol{c}^*_{H_1} + \sinh\rho\, {}_I\boldsymbol{c}^*_{H_2} \tag{2.123}$$

with $\rho \in [0,2\pi]$ for the ellipse and $\rho \in [-\sigma,\sigma]$ for the hyperbola. Thereby, σ is

defined by the intersection of the circle plane with the larger frustum base area. The possible contact points on the circle are parametrised by

$$ {}_I\boldsymbol{C}_C(\rho) = {}_I\boldsymbol{M}_C + r_C\, {}_I\boldsymbol{n}_{CS}(\rho) \tag{2.124} $$

with the normal ${}_I\boldsymbol{n}_{CS}$ of the respective cone section. The contact points can be restricted by the necessary condition

$$ {}_I\boldsymbol{t}_{CS}(\rho) \cdot [{}_I\boldsymbol{C}_C(\rho) - {}_I\boldsymbol{CS}(\rho)] = 0 \tag{2.125} $$

with the tangent ${}_I\boldsymbol{t}_{CS}$ and the parametrisations (2.122) or (2.123) of the respective cone section. This results in the root functions

$$ \left.\begin{aligned} 0 = {} & 2\left[-\sin\rho\ {}_I\boldsymbol{c}^*_{E_1} + \cos\rho\ {}_I\boldsymbol{c}^*_{E_2}\right] \cdot [{}_I\boldsymbol{M}_C - {}_I\boldsymbol{M}_E] \\ & + \sin(2\rho)\left[\| {}_I\boldsymbol{c}^*_{E_1} \|^2 - \| {}_I\boldsymbol{c}^*_{E_2} \|^2\right] \end{aligned}\right\} \quad \text{(ellipse)}\ , \tag{2.126} $$

$$ \left.\begin{aligned} 0 = {} & 2\left[\sinh\rho\ {}_I\boldsymbol{c}^*_{H_1} + \cosh\rho\ {}_I\boldsymbol{c}^*_{H_2}\right] \cdot [{}_I\boldsymbol{M}_C - {}_I\boldsymbol{M}_H] \\ & - \sinh(2\rho)\left[\| {}_I\boldsymbol{c}^*_{H_1} \|^2 - \| {}_I\boldsymbol{c}^*_{H_2} \|^2\right] \end{aligned}\right\} \quad \text{(hyperbola)} \tag{2.127} $$

being solved with a NEWTON-method using analytical JACOBIANs and a globalisation with regula falsi. Assuming continuous contact point transition, a local search is done after a first global contact detection. Selecting the contact parameter with the minimum distance

$$ g_{CE} = \| {}_I\boldsymbol{M}_E - {}_I\boldsymbol{M}_C + \cos\rho\ {}_I\boldsymbol{c}^*_{E_1} + \sin\rho\ {}_I\boldsymbol{c}^*_{E_2} \| - r_C\ , \tag{2.128} $$

$$ g_{CH} = \| {}_I\boldsymbol{M}_H - {}_I\boldsymbol{M}_C + \cosh\rho\ {}_I\boldsymbol{c}^*_{H_1} + \sinh\rho\ {}_I\boldsymbol{c}^*_{H_2} \| - r_C \tag{2.129} $$

between circle and respective cone section is sufficient if multiple contacts are excluded. The resulting contact parameter $\rho_\star$ allows calculating the contact points on the circle

$$ {}_I\boldsymbol{C}_C = {}_I\boldsymbol{M}_C + r_C \frac{{}_I\boldsymbol{CS}(\rho_\star) - {}_I\boldsymbol{M}_C}{\| {}_I\boldsymbol{CS}(\rho_\star) - {}_I\boldsymbol{M}_C \|}\ . \tag{2.130} $$

Then after checking if the selecting gap function (2.128) or (2.129) is negative, the contact point on the frustum and the normals can be calculated with the ideas of the point-to-frustum contact from below.

Inner side of the circle and outer side of the frustum: The circle-to-circle contact only differs in the distance and the normal

$$ g_{CF} = [r_C - r_{F_h} - \| {}_I\boldsymbol{c}_{CF} \|] \cos(\varphi_F)\ , \tag{2.131} $$

$$ {}_I\boldsymbol{n}_F = -\sin(\varphi_F)\, {}_I\boldsymbol{a}_F - \cos(\varphi_F) \frac{{}_I\boldsymbol{c}_{CF}}{\| {}_I\boldsymbol{c}_{CF} \|}\ . \tag{2.132} $$

The circle-to-hyperbola contact cannot appear.

For the circle-to-ellipse contact only the selecting gap function

$$g_{CE} = r_C - \| {}_I\boldsymbol{M}_E - {}_I\boldsymbol{M}_C + \cos(\rho)\, {}_I\boldsymbol{c}^*_{E_1} + \sin(\rho)\, {}_I\boldsymbol{c}^*_{E_2} \| \tag{2.133}$$

is different.

Outer side of the circle and outer side of the frustum: This contact setting yields

$$g_{CF} = [\| {}_I\boldsymbol{c}_{CF} \| - r_C - r_{F_h}] \cos(\varphi_F) \ , \tag{2.134}$$

$${}_I\boldsymbol{n}_F = -\sin(\varphi_F)\, {}_I\boldsymbol{a}_F + \cos(\varphi_F) \frac{{}_I\boldsymbol{c}_{CF}}{\| {}_I\boldsymbol{c}_{CF} \|} \tag{2.135}$$

for the circle-to-circle contact and the same selecting gap functions (2.128) or (2.129) as for the first contact case.

All other contact combinations are physically not possible.

Cylinder: In the case of a cylinder only the circle-to-ellipse contact occurs. Defining the ellipse in its local coordinate system yields the parametrisation

$$x = r_F \cos(\Psi_F)\,,\ y = r_F \sin(\Psi_F)\,,\ z = [r_F \cos(\Psi_F) - \xi_1] \tan(\alpha_{CF}) + \xi_2 \tag{2.136}$$

with the radius r_F of the cylinder. Transforming it into the inertial frame of reference gives the centre and the semi-major as well as the semi-minor axis

$${}_I\boldsymbol{M}_E := {}_I\boldsymbol{P}_F + [\xi_2 - \tan(\alpha_{CF})\, \xi_1]\, {}_I\boldsymbol{e}_{F_3} \ , \tag{2.137}$$

$${}_I\boldsymbol{c}^*_{E_1} := \frac{r_F}{\cos(\alpha_{CF})} [\cos(\alpha_{CF})\, {}_I\boldsymbol{e}_{F_1} + \sin(\alpha_{CF})\, {}_I\boldsymbol{e}_{F_3}] \ , \tag{2.138}$$

$${}_I\boldsymbol{c}^*_{E_2} := r_F\, {}_I\boldsymbol{e}_{F_2} \tag{2.139}$$

of the ellipse. Then with the adapted restrictions from above concerning full ellipse and no multiple contacts, the same procedure can be used for the following calculations.

Point and frustum: Only the general contact between a point ${}_I\boldsymbol{Q}$ and a frustum remains (Fig. 2.12).

Defining

$${}_I\boldsymbol{d} := {}_I\boldsymbol{Q} - {}_I\boldsymbol{P}_F \ , \tag{2.140}$$

$$s := {}_I\boldsymbol{a}_F \cdot {}_I\boldsymbol{d} \ , \tag{2.141}$$

$${}_I\boldsymbol{b} := \frac{{}_I\boldsymbol{d} - s\, {}_I\boldsymbol{a}_F}{\| {}_I\boldsymbol{d} - s\, {}_I\boldsymbol{a}_F \|} \ , \tag{2.142}$$

$$r_{F_h} := r_{F_1} + \frac{r_{F_2} - r_{F_1}}{h_F} s \tag{2.143}$$

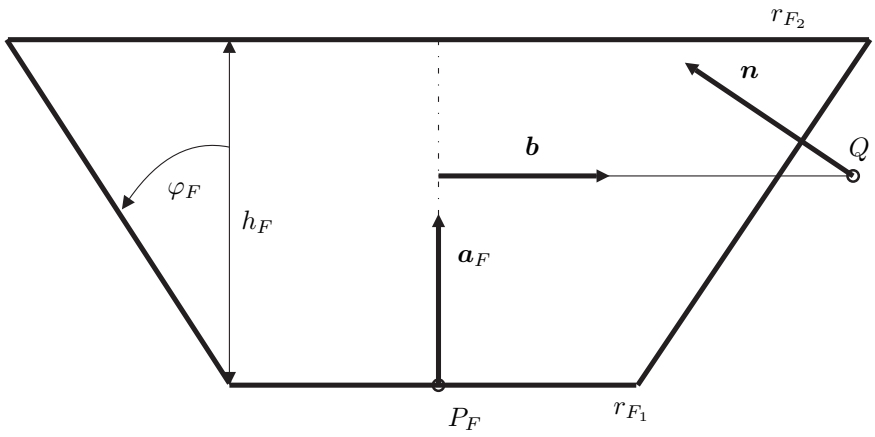

Figure 2.12: Frustum-to-point contact.

it can be tested with

$$\| {}_I\boldsymbol{d} - s\,{}_I\boldsymbol{a}_F \| - \epsilon_{PF} \leq r_{F_h} \leq \| {}_I\boldsymbol{d} - s\,{}_I\boldsymbol{a}_F \| + \epsilon_{PF} \tag{2.144}$$

and $0 \leq s \leq h_F$ if there is contact possible. Thereby, ϵ_{PF} denotes a tolerance value. Then, the inward and outward pointing normals for contact from inside and from outside can be calculated by

$${}_I\boldsymbol{n}_i = \sin(\varphi_F)\,{}_I\boldsymbol{a}_F - \cos(\varphi_F)\,{}_I\boldsymbol{b} \;, \quad {}_I\boldsymbol{n}_o = -\,{}_I\boldsymbol{n}_i \tag{2.145}$$

and the gaps are given by

$$g_i = [\| {}_I\boldsymbol{d} - s\,{}_I\boldsymbol{a}_F \| - r_{F_h}] \cos(\varphi_F) \;, \quad g_o = -g_i \;. \tag{2.146}$$

With

$${}_I\boldsymbol{t}_{i_1} = \frac{1}{\cos(\varphi_F)}\,{}_I\boldsymbol{a}_F - \frac{\sin(\varphi_F)}{\cos(\varphi_F)}\,{}_I\boldsymbol{n}_i \;, \tag{2.147}$$

$${}_I\boldsymbol{t}_{o_1} = \frac{1}{\cos(\varphi_F)}\,{}_I\boldsymbol{a}_F + \frac{\sin(\varphi_F)}{\cos(\varphi_F)}\,{}_I\boldsymbol{n}_o \;, \tag{2.148}$$

$${}_I\boldsymbol{t}_{*_2} = {}_I\boldsymbol{n}_* \times {}_I\boldsymbol{t}_{*_1} \;, \tag{2.149}$$

one gets the radial and azimuthal tangents. The velocity values are calculated as usual (Sect. 1.2.3).

Elastodynamic Sheave

Lower order finite element shape functions are suitable for the efficient description of the internal sheave dynamics. For contour definitions, however, this approach would induce a discontinuous normal vector characteristics [88]. Acceleration jumps, oscillating contact forces, cyclic changing contact points and suboptimal convergence rates of contact solvers might appear. Two-times continuously differential surface

parametrisations are necessary and sufficient to solve these drawbacks. Though, local shading known from computer graphics often yields sensitive solution behaviour due to discontinuous changes of charts [88]. That is why, only global approximations are reasonable for the underlying problem. The awarded adaptive algorithm of CATMULL-CLARK would be a solution for nearly arbitrary topologies [75]. However, the discretisation reduces to a global B-spline surface for the applied regular finite element grid. The advantages of CATMULL-CLARK concerning adaptivity would not have an effect. Finally, a global NURBS-based interpolation of finite element surface nodes is chosen as a relatively easy but local, affine invariant, efficient, accurate and stable contour definition [76, 57].

NURBS: As surface parametrisations can be defined in a tensor product space of curve representations, it is sufficient to discuss one dimensional structures.

Each B-spline curve is given by n control points $\{{}_I\boldsymbol{P}_j\}_j$ and recursively defined spline basis functions $\{N_{j,p}\}_j$ of degree p being parametrised by the real, ordered, non-periodic knot vector

$$\boldsymbol{S} = \left[\underbrace{a,\ldots,a}_{p+1}, s_{p+2},\ldots,s_{m-p-1},\underbrace{b,\ldots,b}_{p+1}\right] \tag{2.150}$$

of length m. As a reason of the global differentiability requirement, it is $m = n+p+1$. Then, the associated curve representation is given by

$${}_I\boldsymbol{C}(s) = \sum_{j=1}^{n} N_{j,p}(s)\,{}_I\boldsymbol{P}_j \quad , \quad s \in [a,b] \tag{2.151}$$

also allowing for smooth curve closing conditions. The dimension of the linear spline space is given by $m-p-1$. The generalisation to the projective space is called non-uniform rational B-spline (NURBS) curve

$${}_I\boldsymbol{C}(s) = \frac{\sum_{j=1}^{n} N_{j,p}(s)\,w_j\,{}_I\boldsymbol{P}_j}{\sum_{k=1}^{n} N_{k,p}(s)\,w_k} = \sum_{j=1}^{n} R_{j,p}(s)\,{}_I\boldsymbol{P}_j \quad , \quad s \in [a,b] \tag{2.152}$$

because of its representation by rational basis functions $\{R_{j,p}\}_j$, using additional positive weights $\{w_j\}_j$. As cone sections are represented exactly, the accuracy increases in spite of still using the efficient evaluation algorithms of the B-spline theory, for example the one of Cox-deBoor [57].

Curve fitting is of special interest in the current situation and can be done by least square or interpolation algorithms. Focusing on global interpolation for exact node representation, the amount per time step can be reduced to the solution of only one sparse, positive and banded linear system of equations. If $\left\{{}_I\boldsymbol{Q}_j\right\}_j$ are for instance

the finite element surface points to be interpolated, it is given by

$$\begin{pmatrix} N_{1,p}(\tilde{s}_1) & \cdots & N_{n,p}(\tilde{s}_1) \\ \vdots & & \vdots \\ N_{1,p}(\tilde{s}_n) & \cdots & N_{n,p}(\tilde{s}_n) \end{pmatrix} \begin{pmatrix} {}_I\boldsymbol{P}_1 \\ \vdots \\ {}_I\boldsymbol{P}_n \end{pmatrix} = \begin{pmatrix} {}_I\boldsymbol{Q}_1 \\ \vdots \\ {}_I\boldsymbol{Q}_n \end{pmatrix} \tag{2.153}$$

with $\{\tilde{s}_j\}_j$ being the evaluation points of the interpolated nodes in the parameter space declared by an iterative chord length projection. This ansatz is based on the heuristics that also the knot vector is defined according to the chord length of the interpolation points. The polynomial degree p is chosen to be larger than the local smoothness demands and the weights are selected representing an initially most accurate approximation. A simplification is the calculation of the knot vector and the computation of the parameter space evaluation points once for the undeformed disk. Then, the system matrix in (2.153) has to be decomposed only in the initialisation and forward/backward substitutions suffice for the solution of (2.153) in each time step.

Contact kinematics to a point: For the numerical calculation of contact kinematics, the expected position, tangents, normal, velocities and JACOBIANs have to be computed. Assuming a point ${}_I\boldsymbol{p}$ with velocity ${}_I\dot{\boldsymbol{p}}$ as contact partner, this must only be done concerning the sheave contour. It is satisfactory to compute the control polygon concerning finite element surface node positions, translational velocities and JACOBIANs once per time step. The position of the k-th surface node is given by (Sect. 2.1.3)

$${}_I\boldsymbol{r}_k = \begin{pmatrix} \begin{pmatrix} \cos\gamma_{C_I} & -\sin\gamma_{C_I} \\ \sin\gamma_{C_I} & \cos\gamma_{C_I} \end{pmatrix} \begin{pmatrix} \cos\varphi_k & -\sin\varphi_k \\ \sin\varphi_k & \cos\varphi_k \end{pmatrix} \begin{pmatrix} r_k + \frac{d}{2}\varphi_{r_k} \\ -\frac{d}{2}\varphi_{\varphi_k} \end{pmatrix} \\ z_{C_I} + u_{z_k} + \frac{d}{2} \end{pmatrix} . \tag{2.154}$$

The corresponding velocity fulfills

$$\begin{aligned} {}_I\dot{\boldsymbol{r}}_k = & \begin{pmatrix} \dot{\gamma}_{C_I} \begin{pmatrix} -\sin\gamma_{C_I} & -\cos\gamma_{C_I} \\ \cos\gamma_{C_I} & -\sin\gamma_{C_I} \end{pmatrix} \begin{pmatrix} \cos\varphi_k & -\sin\varphi_k \\ \sin\varphi_k & \cos\varphi_k \end{pmatrix} \begin{pmatrix} r_k + \frac{d}{2}\varphi_{r_k} \\ -\frac{d}{2}\varphi_{\varphi_k} \end{pmatrix} \\ \dot{z}_{C_I} + \dot{u}_{z_k} \end{pmatrix} \\ & + \begin{pmatrix} \begin{pmatrix} \cos\gamma_{C_I} & -\sin\gamma_{C_I} \\ \sin\gamma_{C_I} & \cos\gamma_{C_I} \end{pmatrix} \begin{pmatrix} \cos\varphi_k & -\sin\varphi_k \\ \sin\varphi_k & \cos\varphi_k \end{pmatrix} \begin{pmatrix} \frac{d}{2}\dot{\varphi}_{r_k} \\ -\frac{d}{2}\dot{\varphi}_{\varphi_k} \end{pmatrix} \\ 0 \end{pmatrix} . \end{aligned} \tag{2.155}$$

The surface position ${}_I\boldsymbol{r}(\boldsymbol{s})$, translational velocity ${}_I\dot{\boldsymbol{r}}(\boldsymbol{s})$ and JACOBIAN $\boldsymbol{J}(\boldsymbol{s})$ distribution are evaluated by interpolation. They are explicitly depending on the surface parametrisation $\boldsymbol{s} \in \mathbb{R}^2$ and implicitly on the overall disk generalised coordinates $\boldsymbol{q}_g$ or velocities $\dot{\boldsymbol{q}}_g$. Then, the tangents and the normal can be used for finding the possible contact point $\boldsymbol{s}_c$ by root functions according to Sect. 1.2.3. It would be a further simplification to directly interpret the representation of the point ${}_I\boldsymbol{p}$ in the

sheave cylinder coordinate system

$$\boldsymbol{u}_c := \begin{pmatrix} r_c \\ \Phi_c \\ z_c \end{pmatrix} = \Pi\left({}_I\boldsymbol{p}\right) \tag{2.156}$$

as a possible contact point. The measure differential equation of the disk [90] again results with the ideas from Sect. 1.2.3.

Contact kinematics to a circle: Using the technique (2.156) for the sheave surface to point contact, the possible contact points only have to be examined on the circle. Let ${}_I\boldsymbol{p}\left(\alpha\right)$ be the contour points on the circle and ${}_I\boldsymbol{q}\left(\alpha\right)$ be the one on the sheave surface with $\alpha \in [0,2\pi]$ and ${}_I\boldsymbol{z}_S$ as the axis of the sheave. Then from

$$\min_{\alpha\in[0,2\pi]} {}_I\boldsymbol{z}_S \cdot \left({}_I\boldsymbol{p}\left(\alpha\right) - {}_I\boldsymbol{q}\left(\alpha\right)\right) \ , \tag{2.157}$$

a necessary condition is given by

$${}_I\boldsymbol{z}_S \cdot \left({}_I\boldsymbol{p}'\left(\alpha\right) - {}_I\boldsymbol{q}'\left(\alpha\right)\right) = 0 \ . \tag{2.158}$$

A prime denotes the derivative with respect to the circle parametrisation α and with the radius r_C and the tangent ${}_I\boldsymbol{t}_C\left(\alpha\right)$ of the circle, it is

$${}_I\boldsymbol{p}'\left(\alpha\right) = r_C \, {}_I\boldsymbol{t}_C\left(\alpha\right) \ . \tag{2.159}$$

Further,

$$\begin{aligned} {}_I\boldsymbol{q}'\left(\alpha\right) &= \begin{pmatrix} \frac{\partial_I \boldsymbol{q}}{\partial r_c} & \frac{\partial_I \boldsymbol{q}}{\partial \Phi_c} & \boldsymbol{0} \end{pmatrix} \boldsymbol{u}_c'\left(\alpha\right) \\ &= \begin{pmatrix} \frac{\partial_I \boldsymbol{q}}{\partial r_c} & \frac{\partial_I \boldsymbol{q}}{\partial \Phi_c} & \boldsymbol{0} \end{pmatrix} \frac{\partial \Pi}{\partial \, {}_I\boldsymbol{p}} \, {}_I\boldsymbol{p}'\left(\alpha\right) \\ &= \begin{pmatrix} \frac{\partial_I \boldsymbol{q}}{\partial r_c} & \frac{\partial_I \boldsymbol{q}}{\partial \Phi_c} & \boldsymbol{0} \end{pmatrix} \begin{pmatrix} \cos\Phi_c & \sin\Phi_c & 0 \\ -\frac{\sin\Phi_c}{r_c} & \frac{\cos\Phi_c}{r_c} & 0 \\ 0 & 0 & 1 \end{pmatrix} \boldsymbol{Q}_{IS}^T \, {}_I\boldsymbol{p}'\left(\alpha\right) \end{aligned} \tag{2.160}$$

results due to the chain rule, the sheave cylinder coordinate system and the transformation matrix $\boldsymbol{Q}_{IS}$ from the sheave moving frame to the world inertial frame of reference.

2.2.4 Element – Ring Package Contacts

Assuming only very small clearance between the elements in longitudinal direction and the guidance of the elements by the ring packages avoiding detachment, two contact points in the middle of the element saddles and at the element pillar define

the contact behaviour of the elements (Fig. 2.2):

$$
{}_E\boldsymbol{R}_{P_L} = \begin{pmatrix} t_T/2 - t_S \\ \tilde{h}_R/2 + h_P - h_S \\ -w_P/4 - w_S/4 + \tilde{w}_R/2 \end{pmatrix} , \; {}_E\boldsymbol{R}_{P_R} = \begin{pmatrix} t_T/2 - t_S \\ \tilde{h}_R/2 + h_P - h_S \\ w_P/4 + w_S/4 - \tilde{w}_R/2 \end{pmatrix} ,
$$

$$
{}_E\boldsymbol{R}_{S_L} = \begin{pmatrix} t_T/2 - t_S \\ h_P - h_S \\ -w_P/4 - w_S/4 \end{pmatrix} , \qquad {}_E\boldsymbol{R}_{S_R} = \begin{pmatrix} t_T/2 - t_S \\ h_P - h_S \\ w_P/4 + w_S/4 \end{pmatrix} .
$$

This neglects a rotational influence between the elements and the ring packages. For each element contact point an individual flexible band contour is defined with respect to the parametrisation of the neutral fibre of the ring packages ${}_I\boldsymbol{r}(x)$:

$$
\begin{aligned}
{}_I\boldsymbol{B} &: \left[0,\tilde{l}_R\right] \times \left[-\frac{b}{2},\frac{b}{2}\right] \to \mathbb{R}^3 , \\
&(x,\mu) \mapsto {}_I\boldsymbol{r}(x) + d_N \frac{\theta_1 \, {}_I\boldsymbol{n}(x) + \theta_2 \, {}_I\boldsymbol{b}(x)}{\sqrt{\theta_1^2 + \theta_2^2}} + \mu \frac{\theta_1 \, {}_I\boldsymbol{b}(x) - \theta_2 \, {}_I\boldsymbol{n}(x)}{\sqrt{\theta_1^2 + \theta_2^2}} .
\end{aligned} \tag{2.161}
$$

As for contour descriptions the normal plays a special role, the accompanying trihedral is defined as $\boldsymbol{n} - \boldsymbol{t} - \boldsymbol{b}$ (Sect. 2.1.2). With the width of the flexible band b, the normal distance d_N and the outward pointing normal direction $\theta_1 \, {}_I\boldsymbol{n} + \theta_2 \, {}_I\boldsymbol{b}$ as linear combination, the setting in Tab. 2.1 is chosen for the specific element contact points.

Table 2.1: Setting for the flexible band contours.

element contour point	ring package	θ_1	θ_2	b	d_N
${}_E\boldsymbol{R}_{P_L}$	left	0	1	$\tilde{h}_R$	$\tilde{w}_R/2$
${}_E\boldsymbol{R}_{P_R}$	right	0	-1	$\tilde{h}_R$	$\tilde{w}_R/2$
${}_E\boldsymbol{R}_{S_L}$	left	-1	0	$\tilde{w}_R$	$\tilde{h}_R/2$
${}_E\boldsymbol{R}_{S_R}$	right	-1	0	$\tilde{w}_R$	$\tilde{h}_R/2$

With the tangent ${}_I\boldsymbol{t}$ of the neutral fibre and an arbitrary contact point ${}_I\boldsymbol{Q}$, the root function for searching contact parameters is given by

$$
0 = {}_I\boldsymbol{t}(x) \cdot [{}_I\boldsymbol{Q} - {}_I\boldsymbol{B}(x,\mu)] = {}_I\boldsymbol{t}(x) \cdot [{}_I\boldsymbol{Q} - {}_I\boldsymbol{r}(x)] \tag{2.162}
$$

yielding x_c. The parameter μ_c can be computed by projection onto the second tangent of the flexible band. Altogether, the normal distance is

$$
g = \left[\frac{\theta_1 \, {}_I\boldsymbol{n} + \theta_2 \, {}_I\boldsymbol{b}}{\sqrt{\theta_1^2 + \theta_2^2}} \right] \cdot [{}_I\boldsymbol{Q} - {}_I\boldsymbol{B}(x_c,\mu_c)] . \tag{2.163}
$$

A bilateral rigid body contact law with two-dimensional STRIBECK-friction is used for the saddle contact and a bilateral rigid contact law without friction is used for

the pillar contact. The friction coefficient

$$\mu_R\left(\dot{\boldsymbol{g}}_{R_T}\right) = \mu_{R_0} + \frac{\mu_{R_1}}{1 + \mu_{R_2}\left\|\dot{\boldsymbol{g}}_{R_T}\right\|^{k_R}} \tag{2.164}$$

is based on the parameters μ_{R_0} [−], μ_{R_1} [−], μ_{R_2} $\left[\mathrm{s}^{\mathrm{k_R}}/\mathrm{m}^{\mathrm{k_R}}\right]$ and k_R [−] as well as the relative velocity $\dot{\boldsymbol{g}}_{R_T}$.

2.2.5 Element – Element Contacts

The element – element contacts can be summarised as follows.

Contour description

Between two adjacent elements the contact point E_B is located at the front bottom and E_T at the front head (Fig. 2.2). Additionally, there are two circular arcs with radius r_R near the left and right front rocking edges

$$\begin{aligned} {}_E\boldsymbol{E}_L &= {}_E\boldsymbol{C}_{F_{A_L}} - \begin{pmatrix} r_R \\ 0 \\ 0 \end{pmatrix} + r_R \begin{pmatrix} 1 & 0 & 0 \\ 0 & \cos\alpha & \sin\alpha \\ 0 & -\sin\alpha & \cos\alpha \end{pmatrix} \begin{pmatrix} \cos\gamma \\ \sin\gamma \\ 0 \end{pmatrix} \\ &= {}_E\boldsymbol{M}_{F_{A_L}} + r_R \begin{pmatrix} \cos\gamma \\ \cos\alpha\sin\gamma \\ -\sin\alpha\sin\gamma \end{pmatrix} , \end{aligned} \tag{2.165}$$

$$\begin{aligned} {}_E\boldsymbol{E}_R &= {}_E\boldsymbol{C}_{F_{A_R}} - \begin{pmatrix} r_R \\ 0 \\ 0 \end{pmatrix} + r_R \begin{pmatrix} 1 & 0 & 0 \\ 0 & \cos\alpha & -\sin\alpha \\ 0 & \sin\alpha & \cos\alpha \end{pmatrix} \begin{pmatrix} \cos\gamma \\ \sin\gamma \\ 0 \end{pmatrix} \\ &= {}_E\boldsymbol{M}_{F_{A_R}} + r_R \begin{pmatrix} \cos\gamma \\ \cos\alpha\sin\gamma \\ \sin\alpha\sin\gamma \end{pmatrix} \end{aligned} \tag{2.166}$$

with $\gamma \in [-\gamma^*,0]$. The binormals of the circles are given by

$${}_E\boldsymbol{b}_L = \begin{pmatrix} 0 \\ -\cos\alpha \\ -\sin\alpha \end{pmatrix} , \quad {}_E\boldsymbol{b}_R = \begin{pmatrix} 0 \\ -\cos\alpha \\ \sin\alpha \end{pmatrix} . \tag{2.167}$$

A plane contour for the rear side is the counterpart for the contours described above. The pin-hole dynamics is modelled with two circle-frustum contacts (Fig. 2.13).

The curved contour of pin and hole satisfies

$${}_E\boldsymbol{E}_P = {}_E\boldsymbol{M}_{F_H} + \begin{pmatrix} x \\ r_{P_2}\cos\psi + x\frac{r_{P_1}-r_{P_2}}{t_T-t_P}\cos\psi \\ r_{P_2}\sin\psi + x\frac{r_{P_1}-r_{P_2}}{t_T-t_P}\sin\psi \end{pmatrix} \qquad \text{with } x \in [t_T - t_P,0] , \tag{2.168}$$

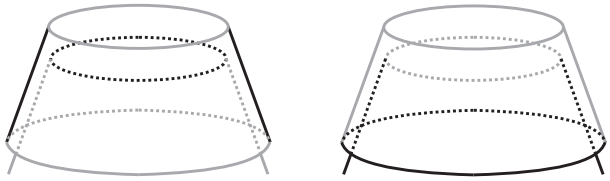

Figure 2.13: Pin – hole contact configuration.

$$ {}_E\boldsymbol{E}_H = {}_E\boldsymbol{M}_{R_H} + \begin{pmatrix} x \\ r_{H_1}\cos\psi + x\frac{r_{H_2}-r_{H_1}}{t_H}\cos\psi \\ r_{H_1}\sin\psi + x\frac{r_{H_2}-r_{H_1}}{t_H}\sin\psi \end{pmatrix} \qquad \text{with } x \in [0,t_H] \tag{2.169} $$

and $\psi \in [0,2\pi)$.

Contact kinematics

With a point ${}_I\boldsymbol{Q}$, the starting point ${}_I\boldsymbol{P}$ and the inward normal vector ${}_I\boldsymbol{n}$ of a general plane the formula for the gap

$$ g = ({}_I\boldsymbol{P} - {}_I\boldsymbol{Q}) \cdot {}_I\boldsymbol{n} \tag{2.170} $$

is easy to derive.

The general contact kinematics between a circle with binormal ${}_I\boldsymbol{b}_C$, centre ${}_I\boldsymbol{M}_C$ as well as radius r_C and a plane with normal ${}_I\boldsymbol{n}_P$ and starting point ${}_I\boldsymbol{P}$ can be defined as follows. Let

$$ t_{PC} = {}_I\boldsymbol{n}_P \cdot {}_I\boldsymbol{b}_C \leq 0 \; . \tag{2.171} $$

Otherwise, one multiplies t_{PC} and ${}_I\boldsymbol{b}_C$ with -1. With

$$ {}_I\boldsymbol{z}_{PC} = {}_I\boldsymbol{n}_P - t_{PC}\,{}_I\boldsymbol{b}_C \;\; , \tag{2.172} $$

$\| {}_I\boldsymbol{z}_{PC} \| = 0$ describes the case of infinite possible contact points. If $\| {}_I\boldsymbol{z}_{PC} \| \neq 0$, the circle possible contact point is given by

$$ {}_I\boldsymbol{M}_C + r_C \frac{{}_I\boldsymbol{z}_{PC}}{\| {}_I\boldsymbol{z}_{PC} \|} \; . \tag{2.173} $$

This reduces the contact back to the contact between point and plane.

The pin-hole dynamics is conceptually the same as the one described for the element – pulley contact in Sect. 2.2.3.

Contact law

The contact law is frictionless, flexible and unilateral. It approximates experimental stiffness measurements of the whole pushbelt in longitudinal direction. The stiffness

at the top, at the rocking edge and at the bottom is

$$\lambda_{E_N}\left(g_{E_N}\right) = \begin{cases} \dfrac{c_{E_1}}{2}\left(\dfrac{N_E}{l_E}\left|g_{E_N}\right| - g_{E_{N_0}}\right) & \text{for} \quad g_{E_N} \leq -g_{E_{N_1}} \ , \\ \dfrac{A}{2}\left|g_{E_N}\right|^{k_{E_1}} & \text{for} \quad -g_{E_{N_1}} < g_{E_N} < 0 \ , \\ 0 & \text{for} \quad g_{E_N} \geq 0 \end{cases} \tag{2.174}$$

using

$$g_{E_{N_1}} = \frac{k_{E_1}}{k_{E_1}-1}\frac{l_E}{N_E} g_{E_{N_0}} \ , \tag{2.175}$$

$$A = \frac{c_{E_1}}{k_{E_1}}\left(\frac{k_{E_1}}{k_{E_1}-1} g_{E_{N_0}}\right)^{1-k_{E_1}}\left(\frac{N_E}{l_E}\right)^{k_{E_1}} \tag{2.176}$$

and the global parameters $g_{E_{N_0}}$ [m], c_{E_1} [N/m], k_{E_1} [−], l_E [−] following the general approach for serial spring connections. The stiffness at the pin-hole contact fulfills

$$\lambda_{E_N}\left(g_{E_N}\right) = \begin{cases} c_{E_2}\left|g_{E_N}\right|^{k_{E_2}} & \text{for} \quad g_{E_N} < 0 \ , \\ 0 & \text{for} \quad g_{E_N} \geq 0 \end{cases} \tag{2.177}$$

with c_{E_2} [N/m$^{k_{E_2}}$] and k_{E_2} [−].

2.3 Assembling and Initialisation

The analysis of a stationary target state is of primary interest in the majority of industrially relevant cases for oscillatory mechanical problems. Thus, it is preferable to calculate a suitable initial value for positions and velocities fulfilling a stationary equality of forces and torques. This reduces at least the decay time of high-frequency vibrations at the beginning of the time dependent simulation. The calculation of such an initial value depends on the specific simulation model. One possibility is to derive a further abstraction of the dynamic model equations. Within the thematic scope, one can for instance consider the various stationary continuous belt models [65, 59] which promise to save about 0.2 s unnecessary real simulation time. Though, implications for the computing time depend on the relationship of the complexity of the dynamic and the stationary model.

2.3.1 Kinematics

With Fig. 2.14, it is

$$t_L = \sqrt{\sin^2\left(\varphi\right) d_A^2 + d_{\text{align}}^2} \tag{2.178}$$

the trum length as well as the arc lengths

$$b_I = 2r_I\,(\pi - \varphi)\ , \tag{2.179}$$
$$b_O = 2r_O\varphi\ . \tag{2.180}$$

The angle φ describes the tangential connection between the arcs. The alignment d_{align} has to be calculated with the relative position of in- and output pulley again depending on the transmission ratio (2.224).

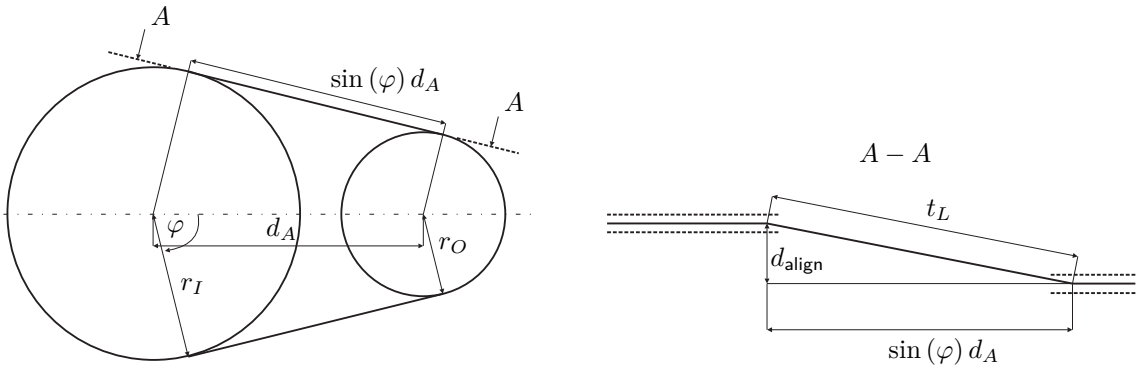

Figure 2.14: Initialisation (axial view and view A-A).

It holds

$$r_I - r_O = \cos(\varphi)\, d_A\ , \tag{2.181}$$
$$\tilde{l}_R = 2t_L + b_I + b_O\ . \tag{2.182}$$

The system of nonlinear equations (2.181)-(2.182) in the unknowns r_I and $\varphi \in [0,2\pi)$ is solved with a NEWTON-method using numerical JACOBIAN evaluations and the initial values

$$r_{I_S} = \left(0.5\,\tilde{l}_R - d_A\right)/\pi\ , \tag{2.183}$$
$$\varphi_S = \pi/2 \tag{2.184}$$

from a setting with $i_r = 1$. The results are used to define position values of the specific pushbelt CVT parts and to form a basis for the calculation of velocity estimates in the next sections.

2.3.2 Kinetics

In [65, chapter 3.5], a planar velocity initialisation of a CVT system is done successfully using a stationary kinetic belt model [59, 28]. In the following, the missing velocity description is derived in a similar way also neglecting outer plane effects. Concerning the belt model, the following assumptions have to be kept in mind:

- planar continuum belt model with only longitudinal elasticity ,

- circle shaped pulley enlacement ,
- symmetrised wedge angle at the pulleys ,
- constant average COULOMB friction in the belt sheave contact ,
- the influence of belt enlargement on radius change is neglected .

In particular, this means to have a mapping between the pushbelt CVT parameters and the belt characteristics. One defines

$$E = \tilde{E}_R \,, \quad A = \tilde{A}_R \,, \quad m^* = \left[N_E m_E + \tilde{\rho}_R \tilde{l}_R \tilde{h}_R 2\tilde{w}_R\right] / \tilde{l}_R \tag{2.185}$$

with Young's modulus E, cross-section A and local mass distribution of the undeformed belt m^*.

From the kinetic point of view, the load torque induces different longitudinal forces in the trums because of friction forces between sheaves and belt. The difference between these forces compensates the excitation and is the same for the input and output pulley. First, the associated force propagation along an arc is derived; last, global estimations yield the final equations.

Geometry of the excitation

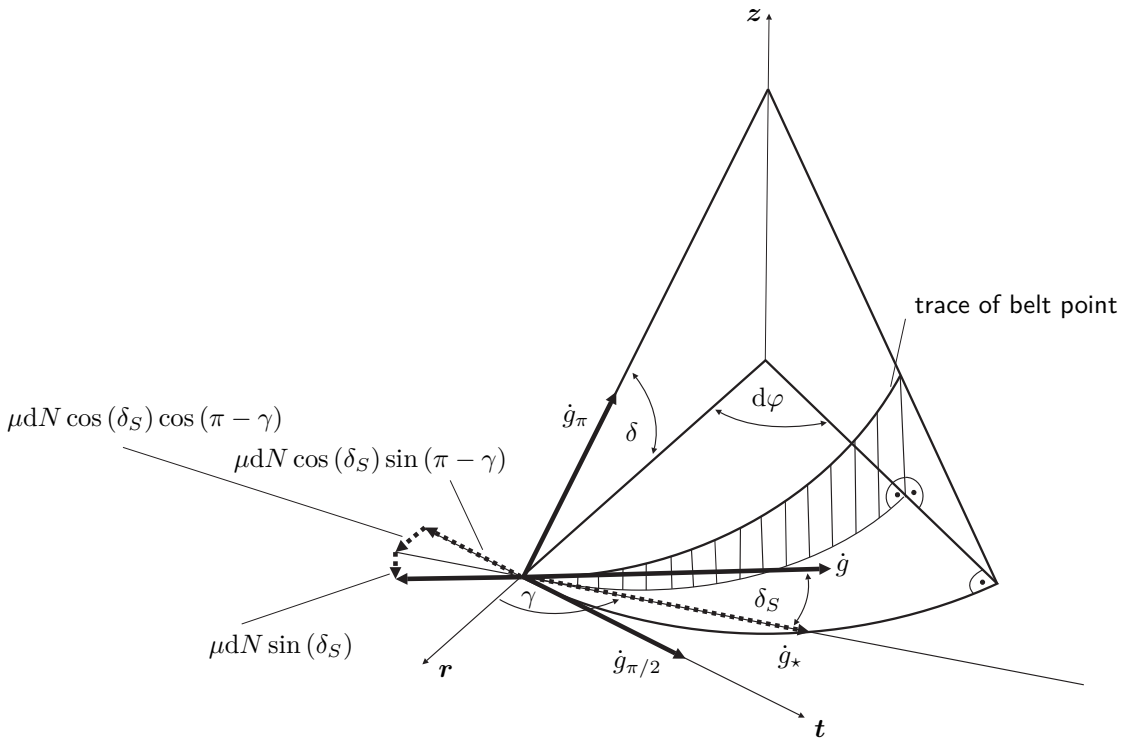

Figure 2.15: Belt slip at sheave.

Using Fig. 2.15 of an infinitesimal sheave sector with opening angle $\mathrm{d}\varphi$, axis $\boldsymbol{z}$, tangent $\boldsymbol{t}$ and radius direction $\boldsymbol{r}$ in the disk rotating coordinate system, it is $\dot{g}$ the

relative elastic slip velocity at the cone surface. The relative elastic slip velocity in the projection plane is $\dot{g}_\star$ with γ being the angle of elastic slip, δ the local half wedge angle including deformation and δ_S its effective part. The decomposition of the friction force $\mu \mathrm{d}N$ in the axial, tangential and radial direction is given by

$$\mu \mathrm{d}N \sin(\delta_S) \ , \tag{2.186}$$
$$\mu \mathrm{d}N \cos(\delta_S) \sin(\pi - \gamma) \ , \tag{2.187}$$
$$\mu \mathrm{d}N \cos(\delta_S) \cos(\pi - \gamma) \ . \tag{2.188}$$

Comparing the direction of $\dot{g}$ for $\gamma = \pi$ given by $\dot{g}_\pi$ and for $\gamma = \pi/2$ given by $\dot{g}_{\pi/2}$ yields

$$\tan(\delta_S) = -\tan(\delta)\cos(\gamma) \ . \tag{2.189}$$

Relationship of tangential and radial belt velocity

In Fig. 2.16, one can see the trace of a belt point from an axial point of view in a global coordinate system.

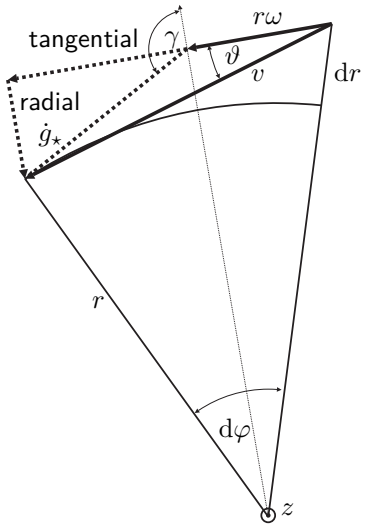

Figure 2.16: Absolute velocity.

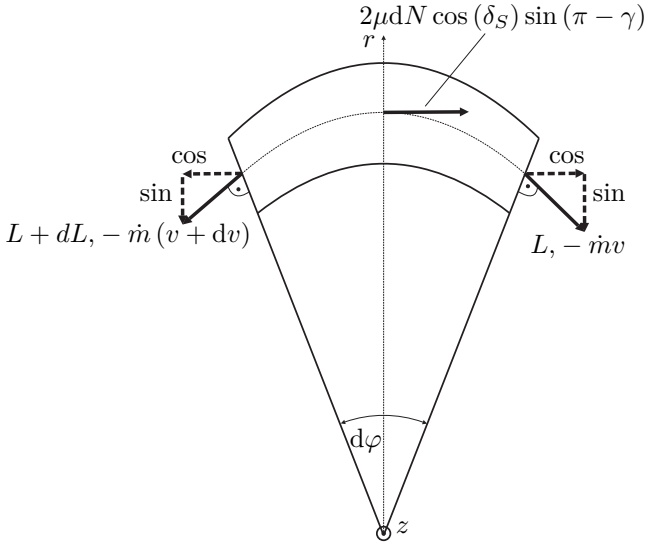

Figure 2.17: Axial view.

Thus in addition to the relative velocities of Fig. 2.15, the rotational velocity of the sheave $r\omega$ is drawn as a positive initial velocity and the curvature angle ϑ describing the change of the running radius r with respect to φ is defined. This results in formulas for the relative tangential and radial velocity

$$\dot{g}_{\star_{\mathrm{tan}}} = v\cos(\vartheta) - r\omega \doteq v - r\omega \ , \tag{2.190}$$
$$\dot{g}_{\star_{\mathrm{rad}}} = \frac{\mathrm{d}r}{\mathrm{d}t} = r'\omega \tag{2.191}$$

with the linearised belt velocity

$$v \doteq \left[1 + \frac{L}{EA}\right] v_0 \tag{2.192}$$

depending on its undeformed part v_0, the longitudinal stiffness EA and the tensile force L. Hereby, a prime denotes the derivative with respect to φ. Together, it is

$$\tan(\gamma) = -\frac{\dot{g}_{\star\tan}}{\dot{g}_{\star\mathrm{rad}}} = -\frac{[EA + L]\, C_S - r}{r'} \tag{2.193}$$

with the elastic slip constant

$$C_S := \frac{v_0}{EA\omega} \tag{2.194}$$

assuming $\omega \neq 0$.

Tangential balance of forces

Figure 2.17 shows the axial view to write down the equality of forces in tangential direction

$$[\mathrm{d}L - \dot{m}\mathrm{d}v]\cos(\mathrm{d}\varphi/2) = 2\mu\mathrm{d}N\cos(\delta_S)\sin(\pi - \gamma) \tag{2.195}$$

involving the double tangential friction force from (2.187) on the right hand side because of a planar description and the constant stationary temporal mass distribution

$$\dot{m} = m^\star v_0 \ . \tag{2.196}$$

This is needed both to simplify the equations and to improve their entropy [65, chapter 3.5.1]. As a result of (2.192), it is

$$\mathrm{d}v = \frac{\mathrm{d}L}{EA} v_0 \ . \tag{2.197}$$

Radial balance of forces

Figure 2.18 can be used to describe the balance of forces in radial direction

$$[2L + \mathrm{d}L - \dot{m}\,(2v + \mathrm{d}v)]\sin(\mathrm{d}\varphi/2) = 2\mathrm{d}N\left[\sin(\delta) + \mu\cos(\delta_S)\cos(\pi - \gamma)\right] \ . \tag{2.198}$$

The internal values appear on the left hand side whereas the radial component of the friction from (2.188) and of the normal force contribute to the right hand side.

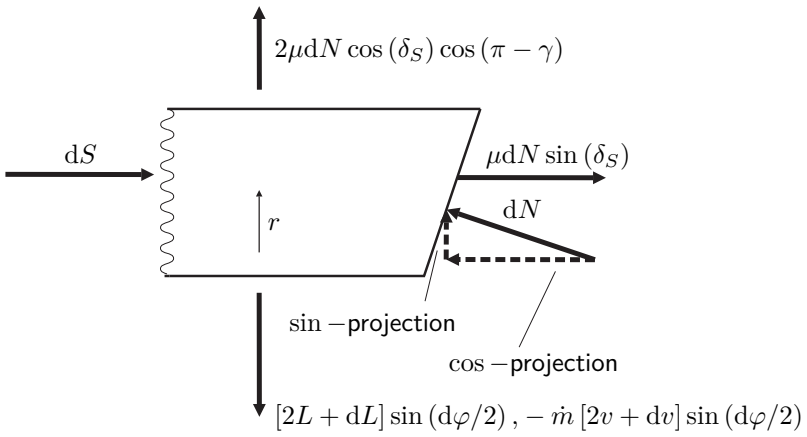

Figure 2.18: Radial view.

Axial balance of forces

The axial equilibrium of forces can be explained with Fig. 2.18 as well. With the sheave expansion force S, it is

$$\mathrm{d}S = \mathrm{d}N\,[\cos(\delta) - \mu \sin(\delta_S)]\ . \tag{2.199}$$

Change of the running radius

Equations (2.186)-(2.199) show the framework of [59, 65, 28] in its full generality. In contrast, changing of the running radius due to sheave tilting, transverse belt elasticity and axial sheave elasticity is not considered in the following because of the minor influence for the initialisation [65, Fig. 2.8 and 4.10]. These assumptions involve

$$\delta' \equiv 0\ , \quad r' \equiv 0\ , \quad \gamma \equiv \pm\pi/2\ , \quad \delta_S \equiv 0 \tag{2.200}$$

and avoid numerical difficulties [65].

Summary of the stationary belt model and environment interaction

From (2.195) and (2.198), it follows by means of the linearisations

$$\cos\left(\frac{\mathrm{d}\varphi}{2}\right) \doteq 1\ ,\ \sin\left(\frac{\mathrm{d}\varphi}{2}\right) \doteq \frac{\mathrm{d}\varphi}{2}\ ,\ \mathrm{d}L\frac{\mathrm{d}\varphi}{2} \doteq 0\ , \tag{2.201}$$

some addition theorems and the consequences of the last paragraph

$$L' = \frac{\pm\mu\,[L - \dot{m}v]}{[1 - \dot{m}\omega C_S] \sin(\delta_0)} = \pm\frac{\mu}{\sin(\delta_0)}L \mp \frac{\dot{m}\mu v_0 EA}{[EA - \dot{m}v_0] \sin(\delta_0)} \tag{2.202}$$

using the intermediate step

$$\mathrm{d}L = \dot{m}\mathrm{d}v + 2\mu\mathrm{d}N\cos(\delta_S)\sin(\gamma) = \dot{m}\mathrm{d}v \pm 2\mu\mathrm{d}N\ , \tag{2.203}$$

$$\begin{aligned} L\mathrm{d}\varphi &= \dot{m}v\mathrm{d}\varphi + 2\mathrm{d}N\left[\sin(\delta) - \mu\cos(\delta_S)\cos(\gamma)\right] \\ &= \dot{m}v\mathrm{d}\varphi + 2\mathrm{d}N\sin(\delta_0)\ . \end{aligned} \tag{2.204}$$

Equation (2.202) is an Euler-Eytelwein description of the longitudinal force propagation along an arc resulting in

$$L(\varphi) = [L_0 - K]\,\mathrm{e}^{\pm\mu^*(\varphi-\varphi_0)} + K \tag{2.205}$$

with

$$\mu^* := \frac{\mu}{\sin(\delta_0)}\ , \quad K := \frac{m^* v_0^2 EA}{EA - m^* v_0^2}\ .$$

If the denominator in the definition of K equaled zero, this would be a contradiction to (2.203) and (2.204).

The global belt setting is drawn in Fig. 2.19.

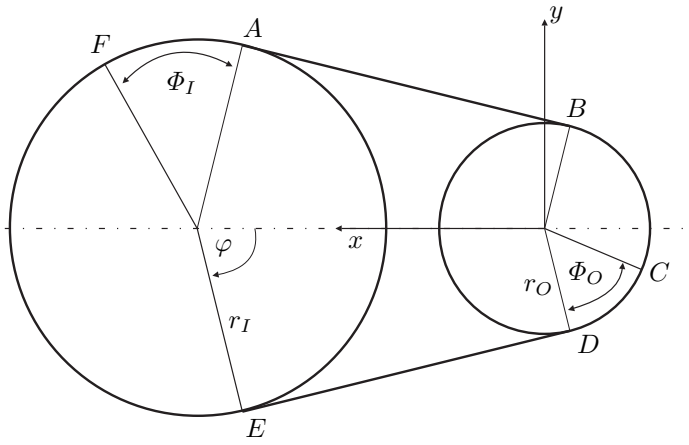

Figure 2.19: Belt kinematics.

The input arc $E - A$, the output arc $B - D$, the tight span $D - E$ and the slack span $A - B$ are canonical notations. The longitudinal force at the end of the input arc $L_{I_{\mathrm{out}}}$ occurs at point A. Similarly, $L_{I_{\mathrm{in}}}$ can be found at E, F and D, $L_{O_{\mathrm{in}}}$ at B and C as well as $L_{O_{\mathrm{out}}}$ at D, E and F. The longitudinal force increases generally at the output arc and decreases at the input arc only in an active part Φ but is always positive [65, chapter 4.1.1]. When modelling elastic sheaves, the points F and C are called orthogonal points [59]. Altogether, this yields a consistent longitudinal force equivalence

$$L_{O_{\mathrm{in}}} = L_{I_{\mathrm{out}}} = (L_{O_{\mathrm{in}}} - K)\,\mathrm{e}^{\mu^*(\Phi_O - \Phi_I)} + K \tag{2.206}$$

resulting in

$$L_{O_{\text{in}}} = K \quad \vee \quad \Phi_O = \Phi_I \ . \tag{2.207}$$

Sticking implies two additional equations

$$\begin{aligned} r_I\omega_I &= v_0\left(1+\frac{L_{I_{\text{in}}}}{EA}\right) \\ &= v_0\left[1+\frac{(L_{O_{\text{in}}}-K)\,\mathrm{e}^{\mu^*\Phi_O}+K}{EA}\right] \quad \text{(points } E-F\text{)} \ , \end{aligned} \tag{2.208}$$

$$r_O\omega_O = v_0\left(1+\frac{L_{O_{\text{in}}}}{EA}\right) \qquad \text{(points } B-C\text{)} \ . \tag{2.209}$$

The equality of torques

$$M_O = r_O\left(L_{O_{\text{out}}}-L_{O_{\text{in}}}\right) = r_O\left(L_{O_{\text{in}}}-K\right)\left(\mathrm{e}^{\mu^*\Phi_O}-1\right) \tag{2.210}$$

with M_O being the positive load torque and the axial equality of forces

$$\begin{aligned} F_{C_O} &= \int_{\varphi_O} S'\mathrm{d}\varphi \\ &= \int_{\varphi_O} \frac{L\left[EA-m^\star v_0^2\right]-m^*v_0^2EA}{2\tan\left(\delta_0\right)EA}\mathrm{d}\varphi \\ &= \frac{EA-m^\star v_0^2}{2\tan\left(\delta_0\right)EA}\left[\int_{-\varphi}^{\varphi-\Phi_O} L\mathrm{d}\varphi+\int_{\varphi-\Phi_O}^{\varphi} L\mathrm{d}\varphi\right]-\frac{m^*v_0^2}{\tan\left(\delta_0\right)}\varphi \\ &= \frac{EA-m^\star v_0^2}{2\tan\left(\delta_0\right)EA}\left[2L_{O_{\text{in}}}\varphi+\left(L_{O_{\text{in}}}-K\right)\left(\frac{\mathrm{e}^{\mu^*\Phi_O}-1}{\mu^*}-\Phi_O\right)\right]-\frac{m^*v_0^2\varphi}{\tan\left(\delta_0\right)} \end{aligned} \tag{2.211}$$

have to be solved concerning the output pulley. Hereby, (2.204) and (2.199) yield the expression for S'.

Reduction of the final equations

Goal of this paragraph is the computation of ω_O, v_0, Φ_I, Φ_O and $L_{O_{\text{in}}}$ for initialising velocity values. Of course, it is $E>0$, $A>0$, $\delta_0>0$, $\varphi>0$, $m^*>0$, $r_I>0$, $r_O>0$, $\omega_I>0$ and thus $v_0>0$ for practical settings. Then clearly,

$$L_{O_{\text{in}}} = \frac{EAr_O\omega_O}{v_0}-EA \tag{2.212}$$

according to (2.209). Concerning (2.207)-(2.211), one has to distinguish two cases:

1. For $L_{O_{\text{in}}}=K$, it follows necessarily $M_O=0$ and $F_{C_O}=0$. The condition $F_{C_O}=0$ means that there is no sheave-belt contact which is practically not

relevant. Furthermore, $M_O = 0$ yields $L_{O_{\text{in}}} = K$ or $\Phi_O = 0$ from the mathematical viewpoint assuming $\mu > 0$. From the physical viewpoint, $\Phi_O = 0$ and so also $\Phi_I = 0$ are interesting. Thus, it is

$$\omega_O = \frac{r_I}{r_O}\omega_I \,, \tag{2.213}$$

$$v_0 = \frac{\sqrt{\left(F_{C_O}\tan\left(\delta_0\right) + EA\varphi\right)^2 + 4EAm^* r_I^2\omega_I^2\varphi^2} - EA\varphi - F_{C_O}\tan\left(\delta_0\right)}{2m^* r_I\omega_I\varphi} \,. \tag{2.214}$$

2. If $M_O \neq 0$, it is necessarily $\Phi_I = \Phi_O$ and $L_{O_{\text{in}}} \neq K$. Hence,

$$\Phi_O = \frac{1}{\mu^*}\ln\left[\frac{M_O}{r_O\left(L_{O_{\text{in}}} - K\right)} + 1\right] \tag{2.215}$$

is only defined for $M_O > r_O\left(K - L_{O_{\text{in}}}\right)$. This condition depends on the kinematic and kinetic setting and states the physical application in the same way as the inequalities

$$\Phi_I < 2\left(\pi - \varphi\right) \,, \quad \Phi_O < 2\varphi \tag{2.216}$$

define the active arcs. Equations (2.208) and (2.211) remain only depending on ω_O and v_0. They can be solved by a generalised NEWTON method with numerical JACOBIAN evaluation and starting values from the $M_O = 0$ case.

Now, ω_I and ω_O can be used for the initialisation of the pulleys' and ring packages' angular velocities. According to (2.192) and (2.205), the expression

$$v = \left[1 + \frac{\left(EA\left(\frac{v_{\text{in}}}{v_0} - 1\right) - K\right)\mathrm{e}^{\mu^*(\varphi - \varphi_0)} + K}{EA}\right] v_0 \tag{2.217}$$

explains the behaviour of the ring package belt velocity in an active arc starting from v_{in} at $\varphi = \varphi_0$. Element velocities have to be inherited from the ring packages.

2.3.3 Pulleys

Of course, the centres of gravity of the fixed sheaves are always at the same position given by

$${}_I\boldsymbol{r}_{O_F} = \begin{pmatrix} 0 \\ 0 \\ w_V/2 + t_{P_{S_O}} \end{pmatrix}, \quad {}_I\boldsymbol{r}_{I_F} = \begin{pmatrix} d_A \\ 0 \\ -w_V/2 - t_{P_{S_I}} \end{pmatrix} \tag{2.218}$$

but the loose sheaves depend on the transmission ratio and on the curved geometry of the elements. Figure 2.20 shows the situation neglecting the thickness of the elements.

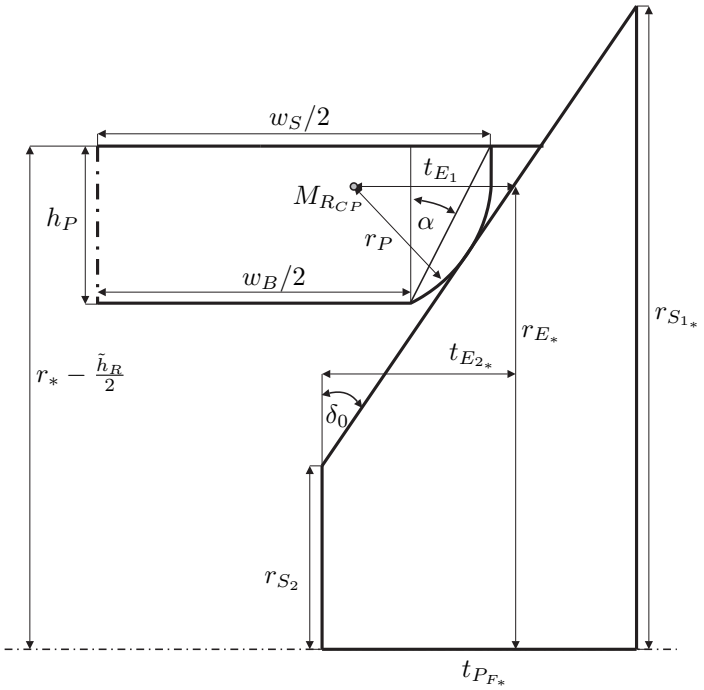

Figure 2.20: Initialisation of loose sheave.

With the centre of the curved element flank $\boldsymbol{M}_{R_{CP}}$ and $* \in \{I, O\}$:

$$r_{E_*} = r_* - \frac{\tilde{h}_R}{2} - \frac{h_P}{2} + d_P \sin\alpha \geq 0 \,, \tag{2.219}$$

$$t_{E_1} = \frac{r_P}{\cos(\delta_0)} \geq 0 \,, \tag{2.220}$$

$$t_{E_{2_*}} = [r_{E_*} - r_{S_2}] \tan(\delta_0) \geq 0 \,. \tag{2.221}$$

Then,

$${}_I\boldsymbol{r}_{O_L} = \begin{pmatrix} 0 \\ 0 \\ \frac{w_V}{2} - t_{P_{S_O}} + 2\left[t_{E_{2_O}} - t_{E_1} - \frac{w_B}{4} - \frac{w_S}{4} + d_P\cos\alpha\right] - 2g_P \end{pmatrix} \,, \tag{2.222}$$

$${}_I\boldsymbol{r}_{I_L} = \begin{pmatrix} d_A \\ 0 \\ -\frac{w_V}{2} + t_{P_{S_I}} - 2\left[t_{E_{2_I}} - t_{E_1} - \frac{w_B}{4} - \frac{w_S}{4} + d_P\cos\alpha\right] + 2g_P \end{pmatrix} \tag{2.223}$$

with g_P being an additional gap used during run-up in such a fashion that there is no contact between pulleys and elements from beginning. Altogether,

$$d_{\text{align}} = w_V + t_{E_{2_O}} + t_{E_{2_I}} - 2t_{E_1} - \frac{w_B}{2} - \frac{w_S}{2} + 2d_P\cos\alpha \tag{2.224}$$

is the difference of the mean values of loose and fixed sheave $\boldsymbol{z}_I$-position concerning input and output pulley. As $t_{E_{2_O}} + t_{E_{2_I}} \neq \text{const.}$, (2.224) explains that it is always necessary to consider a three-dimensional initialisation. Figure 2.21 shows d_{align} as

a typical function of the transmission ratio and confirms its usage as a measure for the misalignment of the pushbelt (Sect. 3.2.3).

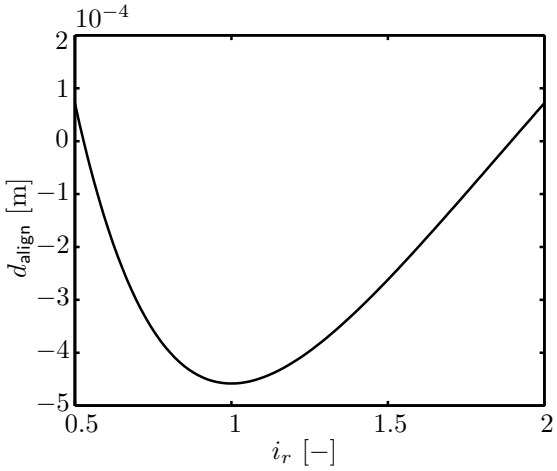

Figure 2.21: Misalignment with respect to the transmission ratio.

The rotational matrices

$$\boldsymbol{A}_{IO_F} = \begin{pmatrix} 1 & 0 & 0 \\ 0 & 1 & 0 \\ 0 & 0 & 1 \end{pmatrix} = \boldsymbol{A}_{II_L}, \quad \boldsymbol{A}_{IO_L} = \begin{pmatrix} -1 & 0 & 0 \\ 0 & 1 & 0 \\ 0 & 0 & -1 \end{pmatrix} = \boldsymbol{A}_{II_F} \tag{2.225}$$

and the angular velocities from the last section are always the same.

2.3.4 Ring Packages

The initialisation of the ring packages is done concerning the inertial frame of reference. According to (2.64), one has to distinguish the initialisation of the global translational, rotational and bending coordinates as well as velocities. In each case, one starts the definition in the output pulley at the beginning of the upper trum in direction of the LAGRANGIAN coordinate (Sect. 2.1.2).

Translational coordinates

The translations in the plane of motion, x and y, can be set canonically along the idealised analytical description from Sect. 2.3.1.

For the z-translation, the determining factors are the mean values of loose and fixed sheave $\boldsymbol{z}_I$-position concerning input and output pulley. They are given by

$$q_{0_{I_M}} = -\frac{w_V}{2} - t_{E_{2_I}} + t_{E_1} + \frac{w_B}{4} + \frac{w_S}{4} - d_P \cos\alpha + g_P \,, \tag{2.226}$$

$$q_{0_{O_M}} = \frac{w_V}{2} + t_{E_{2_O}} - t_{E_1} - \frac{w_B}{4} - \frac{w_S}{4} + d_P \cos\alpha - g_P \,. \tag{2.227}$$

The mean ring package $\boldsymbol{z}_I$-position of the k-th finite element of length l_0 is given by the formula

$$q_{0_{Mz}} = \frac{kl_0}{t_L} q_{0_{I_M}} + \left(1 - \frac{kl_0}{t_L}\right) q_{0_{O_M}} \quad \text{for} \quad kl_0 \leq t_L \tag{2.228}$$

exemplary in the upper trum. Then, for the left or right ring package only the summands $\frac{w_S+w_P}{4}$ or $\frac{-w_S-w_P}{4}$ have to be added, respectively.

The translational velocities are only defined in the plane of motion. They are projections of the longitudinal belt velocity from Sect. 2.3.2 on the ring package coordinate system.

Rotational coordinates

Concerning the two rotational directions, a decoupling results for $|d_{\text{align}}| \ll 1$. Hence, the single tasks can again be done canonically along the idealised analytical description from Sect. 2.3.1.

The angular velocity according to Sect. 2.3.2 is only defined in the plane of motion of the CVT.

Deflection coordinates

Regarding the deflections (Sect. 2.1.2) for $|d_{\text{align}}| \ll 1$, it holds the linearised relationship

$$\hat{w}_1 \doteq w_2 \,, \tag{2.229}$$

$$\hat{w}_2 \doteq -w_1 \tag{2.230}$$

between the bending and angle polynomials (Sect. 2.1.2). Thus as expected, both directions can be discussed separately.

For the geometry in the plane of motion, the deflections of the k-th finite element (FE) of length l_0 are given for example in the input pulley by

- $kl_0 - t_L \geq \frac{3l_0}{4}$ (at least three fourth of the FE is inside the pulley)

$$c_{L_2} = r_I \left[\cos\left(\frac{l_0}{4r_I}\right) - 1\right] \,, \tag{2.231}$$

$$c_{R_2} = r_I \left[\cos\left(\frac{l_0}{4r_I}\right) - 1\right] \tag{2.232}$$

- $\frac{l_0}{2} < kl_0 - t_L < \frac{3l_0}{4}$ (more than one half of the FE is inside the pulley)

$$c_{L_2} = r_I \left[\cos\left(\frac{kl_0 - t_L - \frac{l_0}{2}}{r_I}\right) - 1\right]$$

$$- \left(\frac{3l_0}{4} - kl_0 + t_L \right) \sin \left(\frac{kl_0 - t_L - \frac{l_0}{2}}{r_I} \right) \ , \tag{2.233}$$

$$c_{R_2} = r_I \left[\cos \left(\frac{l_0}{4r_I} \right) - 1 \right] \tag{2.234}$$

- $\frac{l_0}{4} < kl_0 - t_L \leq \frac{l_0}{2}$ (more than one fourth of the FE is inside the pulley)

$$c_{L_2} = 0 \ , \tag{2.235}$$

$$c_{R_2} = r_I \left[\cos \left(\frac{kl_0 - t_L - \frac{l_0}{4}}{r_I} \right) - 1 \right] \tag{2.236}$$

- $kl_0 - t_L \leq \frac{l_0}{4}$ (at most one fourth of the FE is inside the pulley)

$$c_{L_2} = 0 \ , \tag{2.237}$$

$$c_{R_2} = 0 \ . \tag{2.238}$$

The outer plane deflections fulfill for instance in the input pulley

- $kl_0 - t_L \geq \frac{3l_0}{4}$ (at least three fourth of the FE is inside the pulley)

$$c_{L_1} = 0 \ , \tag{2.239}$$

$$c_{R_1} = 0 \tag{2.240}$$

- $\frac{l_0}{2} < kl_0 - t_L < \frac{3l_0}{4}$ (more than one half of the FE is inside the pulley)

$$c_{L_1} = - \sin \left(\beta_{\text{align}} \right) \left[t_L - (k-1)\, l_0 - \frac{l_0}{4} \right] \ , \tag{2.241}$$

$$c_{R_1} = 0 \tag{2.242}$$

- $\frac{l_0}{4} < kl_0 - t_L \leq \frac{l_0}{2}$ (more than one fourth of the FE is inside the pulley)

$$c_{L_1} = 0 \ , \tag{2.243}$$

$$c_{R_1} = - \sin \left(\beta_{\text{align}} \right) \left[(k-1)\, l_0 + \frac{3}{4} l_0 - t_L \right] \tag{2.244}$$

- $kl_0 - t_L \leq \frac{l_0}{4}$ (at most one fourth of the FE is inside the pulley)

$$c_{L_1} = 0 \ , \tag{2.245}$$

$$c_{R_1} = 0 \tag{2.246}$$

with

$$\beta_{\text{align}} = -\arctan\left(\frac{q_{0_{I_M}} - q_{0_{O_M}}}{d_A \sin\varphi}\right) . \tag{2.247}$$

Bending velocities are neglected.

2.3.5 Elements

Last, the elements are initialised by setting their initial translational vector and their rotational matrix. It is assumed that the elements are perpendicular to the virtual mean value of the ring packages at the virtual saddle. The only problem is to increase the LAGRANGIAN coordinate x during initialisation of the elements. This is done in three steps:

1. Calculate a planar initial value (cf. below) .
2. Satisfy a previously defined criterion $\epsilon_E \leq g_E < 2\epsilon_E$ with a small parameter ϵ_E and the element gap g_E, which is the maximum of the negative or if there is none the minimum of the positive single gaps, by an iterative spatial improvement of the planar guess using the exact element contact geometry (Sect. 2.2.5) .
3. Scrutinise the whole remaining gap g_{E_r} according to a weak numerical requirement [27]

   $$0\,\text{m} < g_{E_r} < 160 \cdot 10^{-5}\,\text{m} \tag{2.248}$$

   and incorporate by distributing to all the elements .

For the planar initial value, the first element is defined at the ring package position $x = \epsilon_E$. Then of course in the trums, the step size of the LAGRANGIAN coordinate equals t_T. For at least one of two contacting elements being in the arcs, the following approach shown for the input pulley is reasonable (Fig. 2.22).

With the centre M of the rocking edge radius, the ring package contact point R_S and $l = r_R - t_T/2$ assuming $r_R > t_T/2$, the gap angle Ψ is of special interest for initialising one element with step size $\Delta x = \Psi r_I$ after its predecessor. For both elements in the ideal circle shaped arc, $0 \leq \Psi < \pi/2$ and no additional gaps between adjacent elements, it is

$$l\cos\Psi + \left[r_I - \frac{\tilde{h}_R}{2} - h_P + h_R\right]\sin\Psi = r_R + \frac{t_T}{2} . \tag{2.249}$$

If the centre of the predecessor is not in the arc,

$$\Delta x = t_L - x_{\text{pre}} + \Psi r_I \tag{2.250}$$

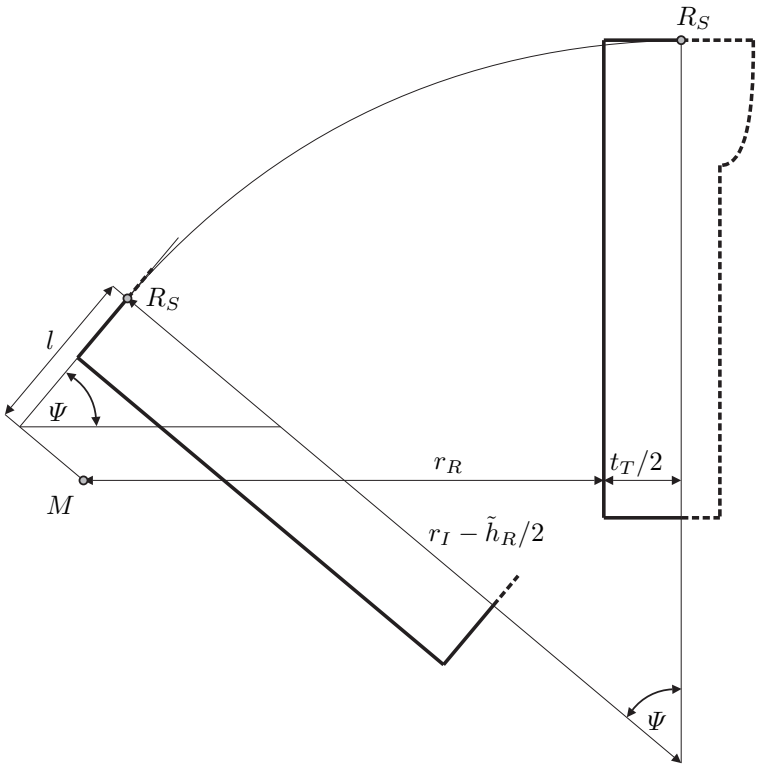

Figure 2.22: Initialisation of elements in pulley arc.

consists of a part in the trum and one in the arc with the position of the ring contact point of the predecessor x_{pre}. Both if the contacting surface is in the arc and if it is outside, the related angle Ψ is given by the root function

$$l\cos\Psi + \left[r_I - \frac{\tilde{h}_R}{2} - h_P + h_R\right]\sin\Psi = r_R - t_L + x_{\text{pre}} + \frac{t_T}{2}\ . \tag{2.251}$$

If the successor centre is not in the arc, the angle Ψ is known. One gets for the trum and arc part

$$\Delta x = \frac{1}{\cos\Psi}\left[r_R + \frac{t_T}{2}\right] - l + \tan\Psi\left[h_P - h_R - r_I + \frac{\tilde{h}_R}{2}\right] + \Psi r_I\ . \tag{2.252}$$

With the above described concept, it is even possible to detect the current element situation by using the gap Δx of the last step for testing.

The transformation matrix between the inertial and element frame of reference is given by

$$\boldsymbol{A}_{IE} = \underbrace{\begin{pmatrix} {}_I\boldsymbol{n}_{R_v} & {}_I\boldsymbol{t}_{R_v} & {}_I\boldsymbol{b}_{R_v} \end{pmatrix}}_{\boldsymbol{A}_{IE'}} \underbrace{\begin{pmatrix} 0 & 1 & 0 \\ -1 & 0 & 0 \\ 0 & 0 & 1 \end{pmatrix}}_{\boldsymbol{A}_{E'E}}\ . \tag{2.253}$$

Further, the position of the elements can be calculated with the position ${}_I\boldsymbol{r}_{R_v}$ of the virtual ring package at the given value of the LAGRANGIAN coordinate

$$ {}_I\boldsymbol{r}_E = {}_I\boldsymbol{r}_{R_v} + \boldsymbol{A}_{IE} \begin{pmatrix} t_S - t_T/2 \\ -h_P + h_S - \tilde{h}_R/2 \\ 0 \end{pmatrix} . \tag{2.254} $$

The velocities can also be taken from the ring package.

2.4 Summary

The overall model equations of the variator have the structure of Sect. 1.2.1 and are characterised by a large degree of freedom of about 3500 and 5500 contacts. In [27] the degree of freedom and the number of contacts of the related planar model based on the nonsmooth mechanics approach are summarised with 1500 and 3500, respectively. Nevertheless, the modular structure of both models allows for refinements or even substitutions of sub-models. A detailed comparison is given in Tab. 2.2.

It is clear, that Young's modulus of the ring packages influences the numerical stiffness of the whole CVT and furthermore the global time step size of explicit integration schemes (Sect. 1.3). However, the high contact closing frequency has to be resolved in a certain level to represent the variator dynamics. Together with the large degree of freedom of the system, this causes long simulation times especially for the spatial model. With the techniques of Sect. 2.5 these challenges shall be eliminated and the simulation model shall be prepared for reasonable validation.

Further, the initialisation results in additional instabilities for instance because of a jump from curvature 0 in the trum to a constant curvature $\neq 0$ in the arcs not being represented exactly by the bending polynomials. To minimise the effects on the rest of the simulation, a special pre-integration perhaps with reduced integration time step size or with additional damping values in between the elements has to be performed to get a physically valid, stationary state of the system.

2.5 CPU Time Reduction

The computational amount during the integration of a differential equation can be divided into the amount per time step and the number of time steps as a multiplier. In the following the spatial simulation of a chain of pearls, a flexible belt with 30 rigid elements that are linearly arranged, is chosen as a first benchmark problem (cp. Fig. 2.23). The elements' kinematics is described relatively to the belt, 20 finite elements have been used for its discretisation and an half-explicit timestepping scheme [25] is applied. The main effort per time step is defined by the kinematic

Table 2.2: Comparison between the current spatial and the planar model [27].

model facet	**planar model**	**spatial model**	**conclusion**
elements	rigid with $\mathrm{dof} = 3$	rigid with $\mathrm{dof} = 6$	canonic extension
ring packages	1 planar co-rotational beam with large deflection	2 spatial co-rotational beams with large deflection	canonic extension
pulley sheaves	2 rigid sheaves with $\mathrm{dof} = 1$ or $\mathrm{dof} = 2$	4 rigid sheaves with $\mathrm{dof} = 1$ or $\mathrm{dof} = 4$ 4 elastodynamic moving frame of reference sheaves	more detailed *spatial* model more detailed *spatial* model
sheave – sheave joint	not necessary	translational joint	canonic extension
pulley – environment	kinematic at input and kinetic at output pulley	kinematic at input and kinetic at output pulley	no difference
element – pulley	1 contour point per element rigid contact with friction Maxwell contact with friction	4 contour circles per element rigid contact with friction decoupled flexible contact with friction	more detailed *spatial* model no difference more detailed *planar* model
element – ring package	1 contour point per element bilateral contact with friction	4 contour points per element bilateral contact with friction	canonic extension no difference
element – element	2 point – line contacts 3 point – line contacts 1 circle – line contact flexible contact	2 point – plane contacts 2 circle – frustum contacts 2 circle – plane contacts flexible contact	canonic extension canonic extension canonic extension no difference
assembling	planar kinematic	spatial kinematic and kinetic using the exact contact kinematics	more detailed *spatial* model

element and finite element update. The time step size itself is declared by the numerical stiffness of the flexible part. In the following, the update loop parallelisation and the ring package model stabilisation are analysed to reduce the overall central processing unit (CPU) time.

2.5.1 Stabilisation of the Ring Package

When increasing the number of finite elements in an explicit integration scheme, it has been recognized that NEWTON's method does not succeed in the solution of the transformation between internal and global coordinates although an analytical JACOBIAN and double machine precision are used for the nonlinear equations' solver (Sect. 2.1.2). A solution can be found by decreasing the integrator time step size or using a linear implicit scheme with the necessary evaluation of finite element JACOBIAN matrices of the right hand side being the drawback. To avoid this additional effort the problem is analysed by linearising the transformation around the

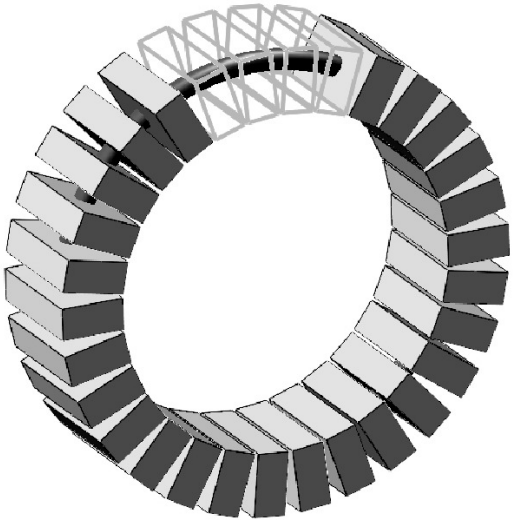

Figure 2.23: Chain of pearls: rigid elements with unilateral contacts on flexible belt.

$\mathbf{x}^I$-$\mathbf{y}^I$-plane. This changes the following equations from Sect. 2.1.2

$$\tilde{\mathbf{F}}_1 := \varphi_{S_0} - \frac{\varphi_{L_0} + \varphi_{R_0}}{2} = 0 \,, \tag{2.255}$$

$$\tilde{\mathbf{F}}_6 := d_{R_2} - d_{L_2} + (x_R - x_L)\sin(\varphi_{S_2}) - (y_R - y_L)\cos(\varphi_{S_2}) = 0 \,, \tag{2.256}$$

$$\tilde{\mathbf{F}}_7 := d_{L_1} - d_{R_1} - (z_R - z_L) = 0 \tag{2.257}$$

and yields a decoupling of the spatial motion. Finally, it results in a nonlinear equation

$$\begin{aligned} F(\varphi_{S_2}) := {} & (x_R - x_L)\sin(\varphi_{S_2}) - (y_R - y_L)\cos(\varphi_{S_2}) \\ & + \frac{64}{17}\left[\frac{3l_0}{64}\left(\frac{\varphi_{L_2} + \varphi_{R_2}}{2} - \varphi_{S_2}\right) - c_{L_2} + c_{R_2}\right] = 0 \end{aligned} \tag{2.258}$$

in φ_{S_2} comprising an affine equation and a superposed oscillation. Figure 2.24 shows this nonlinear function and its affine part in different settings.

The solution of the last iteration and so the canonical starting value (marked with a cross) is always in the antinode around $\varphi_{S_2} = 0$. If the integrator time step size is small enough (left figure), this yields a new solution (marked with a circle). For large time step sizes (right figure) for instance when global input parameters (axis intercept) blow up for increasing simulation time due to instability, the starting value for NEWTON's method would have to be shifted to the antinode of the expected solution. The time step size for the explicit integration scheme $\Delta t < 5 \cdot 10^{-8}\,\mathrm{s}$ is defined by the numerical stiffness of the ring package equations of motion and not by $\Delta t < 5 \cdot 10^{-6}\,\mathrm{s}$ resulting from the Nyquist-Shannon sampling theorem and 20,000 Hz being the polygonal frequency upper bound of a pushbelt CVT. The theoretically possible improvement factor 100 in practice decreases to a maximum realistic improvement factor. This factor depends on the computer architecture because of the

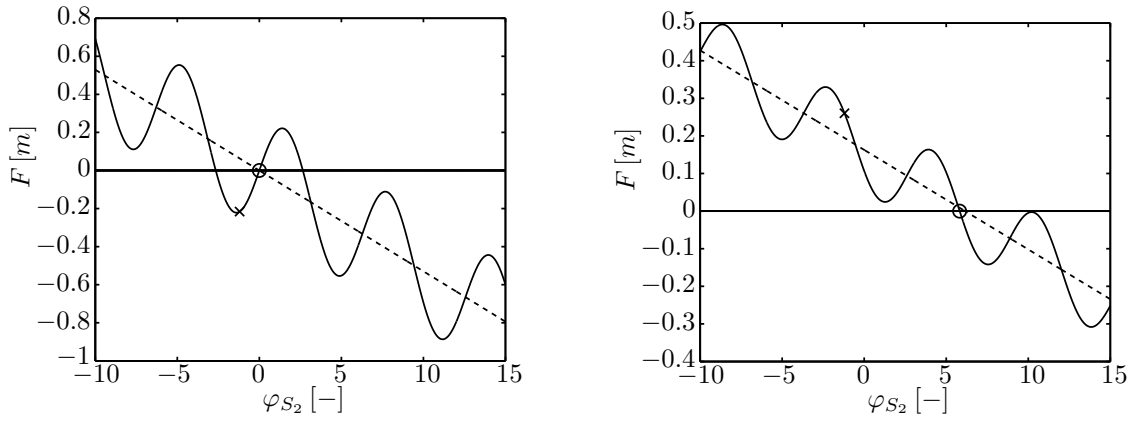

Figure 2.24: Zeros of the planar beam transformation root function.

additional effort per time step of linear implicit integration schemes and on the instability induced by the oscillation of the nonlinear transformation function projected to the abscissa.

2.5.2 Parallel Computing Architectures

Today, Moore's law states that the number of transistors on a standard processor doubles every 18 months. Based on empirical studies, Gordon Moore formulated this rule of thumb in 1965 and proposed a validity period of about ten to 15 years in 2007. This yields a profit in performance which cannot be achieved any more by higher clock rates due to technical limitations but by parallelism on CPU level with multicore architectures. The consequences for software developers are the adaptation of existing programs and the design of new ones concerning these hardware trends.

Usually, one has no memory limits in the case of multibody systems such that a multiple instruction multiple data (MIMD) architecture with shared memory can be used. This is the field of the OpenMP interface [15] giving the possibility to simply extend a serial program with control structures for parallelisation. Then, the advantages can be measured by

$$\text{speed-up} \quad s_n := \frac{t_1}{t_n} \,, \tag{2.259}$$

$$\text{efficiency} \quad e_n := \frac{s_n}{n} \tag{2.260}$$

whereby t_n is the run-time of the program on n processors. There exist several theoretical estimates for the maximum achievable speed-up,

$$\text{Amdahl's law} \quad s_n \leq s_{A_n} := \frac{1}{\sigma + \frac{1-\sigma}{n}} \preccurlyeq \frac{1}{\sigma} \,, \tag{2.261}$$

$$\text{Gustafson's law} \quad s_n = s_{G_n} := \frac{t_s + n\, t_p}{t_s + t_p} \preccurlyeq n \,. \tag{2.262}$$

Both rules are based on different ideas. Amdahl assumes the serial code part σ to be constant when considering one simulation model. This results in an upper bound for the speed-up because of administrative overhead when enlarging the number of processors. Gustafson looks at the simulation time of a parallel program on a single core machine with the sequential simulation time part t_s and the parallel simulation time part t_p. For an asymptotic consideration, he assumes the sequential simulation time to decrease relatively if one uses more processors for example in the practically relevant applications of larger simulation models. Altogether, one has a more pessimistic rule of Amdahl and a more optimistic one of Gustafson available for comparison with experimental scaling measurements of a concrete program.

Profiling yields that in the discussed multibody system context of Fig. 2.23 the main computational cost per time step is spent for the kinematic update of the rigid elements and of the finite elements potentially being used for the discretisation of the flexible belt. Both items are organised in loops from the point of view of software development. This can be summarised by the formulas for the components of the global equations of motion

$$\mathbf{M} = \sum_j \mathbf{J}_j^T \mathbf{M}_j \mathbf{J}_j \ , \quad \mathbf{h} = \sum_j \mathbf{J}_j^T \mathbf{h}_j \ , \quad \mathbf{W} = \sum_j \mathbf{J}_j^T \mathbf{W}_j \ . \tag{2.263}$$

The single update jobs of the summation loop are independent with respect to memory and computation. The final inserting into global memory space is the only critical task. According to Amdahl's law $s_4 \leq s_{A_4} = 2.05$, $e_4 \leq 0.5$ and according to Gustafson's law $s_4 \leq s_{G_4} = 2.2$, $e_4 \leq 0.55$ are expected for a four-core machine. The results in Fig. 2.25 show the thread profiling with parallelised updates, sequential summation, blocking of threads and not parallelised segments.

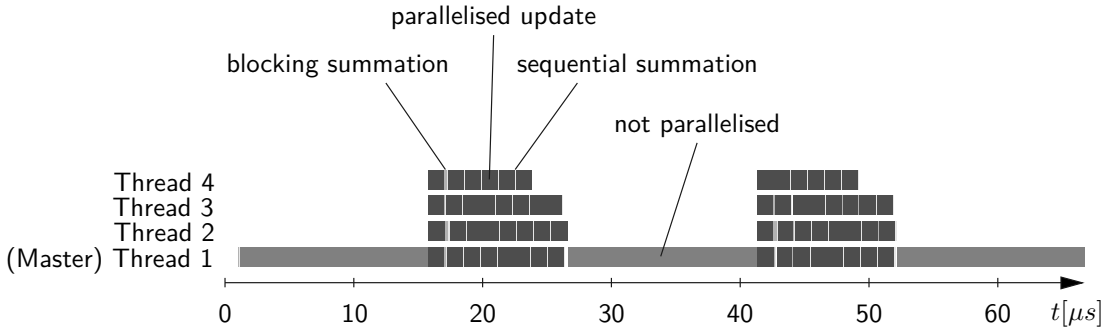

Figure 2.25: Thread profiling.

A speed-up $s_4 = 1.7$ has been achieved resulting in an efficiency factor $e_4 = 0.43$. Hence, the result of parallelisation is quite promising but there should still be possibilities to improve the scaling of the parallel parts about $0.07 - 0.12$ efficiency values in comparison to the theory and to extend parallelisation to parts that have not been parallelised by now.

2.5.3 Practical Evaluations and Experiences

The academic example of the previous sections (Fig. 2.23) uses a relative kinematics between elements and flexible belt and a unilateral contact law between the elements. In the following this setting is extended step-by-step to the real pushbelt CVT simulation model (Fig. 2.23).

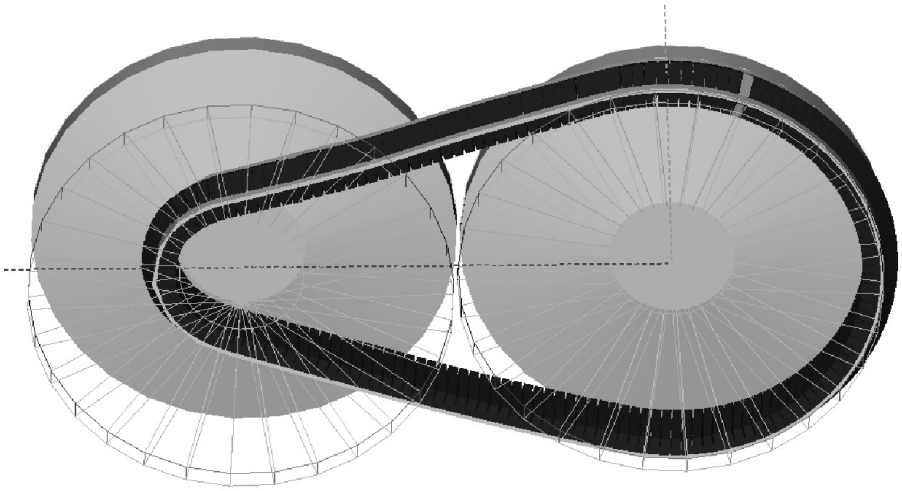

Figure 2.26: Real pushbelt CVT simulation model.

In this context also the number of elements is increased to 160 which is a good compromise for reasonable validation [27].

Stability

The behaviour of the simulation should appear as robust as possible in practice. Section 2.5.1 shows that the transformation between internal and global coordinates of the ring package is a major factor constraining the time step size. It points out that adding damping does not improve this behaviour in practice. Only the usage of implicit integration schemes would be a solution.

Parallelisation

Analysing an absolute description with bilateral contact law between elements and flexible belt instead of the relative kinematics and varying the number of rigid elements in Fig. 2.23 changes the amount of computing time of an half-explicit timestepping scheme during the update functions for the smooth right hand side $\boldsymbol{h}$, the gap velocities $\dot{\boldsymbol{g}}$, the contact JACOBIANS $\boldsymbol{J}$, the gaps $\boldsymbol{g}$ and the system matrix $\boldsymbol{G} = \boldsymbol{W}^T \boldsymbol{M}^{-1} \boldsymbol{W}$ for the constraint solution as well as the GAUSS-SEIDEL constraint solver. The results are shown in Tab. 2.3.

Table 2.3: Profiling of an extended chain of pearls example.

N_E	update $\boldsymbol{h}$	update $\dot{\boldsymbol{g}}$	update $\boldsymbol{J}$	update $\boldsymbol{g}$	update $\boldsymbol{G}$	GS solver
30	$s_{A_2} = 1.03$	$s_{A_2} = 1.03$	$s_{A_2} = 1.08$	$s_{A_2} = 1.16$	$s_{A_4} = 1.32$	neglected
	$s_{G_2} = 1.05$	$s_{G_2} = 1.05$	$s_{G_2} = 1.14$	$s_{G_2} = 1.28$	$s_{G_4} = 1.96$	neglected
	$s_2 = 0.92$	$s_2 = 0.96$	$s_2 = 0.98$	$s_2 = 1.03$	$s_4 = 0.79$	neglected
80	neglected	neglected	$s_{A_2} = 1.05$	$s_{A_2} = 1.11$	$s_{A_4} = 1.70$	neglected
	neglected	neglected	$s_{G_2} = 1.10$	$s_{G_2} = 1.20$	$s_{G_4} = 2.65$	neglected
	neglected	neglected	$s_2 = 0.97$	$s_2 = 0.99$	$s_4 = 0.70$	neglected
160	neglected	neglected	$s_{A_2} = 1.01$	$s_{A_2} = 1.02$	$s_{A_4} = 1.29$	$s_{A_2} = 1.42$
	neglected	neglected	$s_{G_2} = 1.02$	$s_{G_2} = 1.04$	$s_{G_4} = 1.90$	$s_{G_2} = 1.59$
	neglected	neglected	$s_2 = 0.99$	$s_2 = 1.01$	$s_4 = 1.21$	$s_2 = 0.99$

Each update method is treated separately. Except the last one, they are parallelised with respect to the number of bodies or contacts using OpenMP on a two-core machine with dynamic scheduling which turns out to perform better than static scheduling. The update of $\boldsymbol{G}$ includes the solution of a linear system of equations. This is parallelised using *ATLAS*[1] on a four-core computer. The theoretical upper bounds of Amdahl's and Gustafson's law describe the respective computational amount of the routines and the expected benefit due to parallelisation. The expression *neglected* states that the fraction of the method with respect to the overall computational amount is under a certain threshold. The practical experiences for 30 and 80 elements are mean values from three calculations with 500 time and five plot steps. For 160 elements only 200 time and two plot steps have been done. The following comments can be made:

- The dominance of the kinematic and kinetic update of elements and finite elements vanishes in comparison with the relative kinematics.
- The contact kinematic and kinetic calculations become more and more important (gaps $\boldsymbol{g}$, gap velocities $\dot{\boldsymbol{g}}$, Jacobians, contact solver).
- The calculation of the gaps $\boldsymbol{g}$ and the gap velocities $\dot{\boldsymbol{g}}$ is dominated by the bilateral contact between elements and flexible band with 96.5% and 73.5%, respectively.
- The practical experiences are disillusioning in comparison with the theory. Although contact calculations are the main overall computational amount, they are decoupled. Each single contact calculation is very fast and the overhead due to parallelisation exceeds the achievable benefit in the current implementation. The only items to discuss for the CVT application with 160 elements seem to be the update of the gaps $\boldsymbol{g}$ and of $\boldsymbol{G}$.
- *ATLAS* is an abbreviation for automatically tuned linear algebra software and behaves differently depending on the used computer architecture. Hence, the improvement by parallelising the update of $\boldsymbol{G}$ is difficult to reproduce.

1 `http://www.netlib.org/atlas/`

The real CVT model additionally includes considerably more contact descriptions for instance friction laws, two ring packages with 12 finite elements each, the nipple-hole or rocking edge kinematics and the whole element – pulley interaction. The results are shown in Tab. 2.4.

Table 2.4: Profiling of pushbelt CVT.

$\mathbf{N_E}$	update J	update $\dot{g}$	update G	update g
80	$\mathbf{s_{A_2} = 1.06}$ $\mathbf{s_{G_2} = 1.11}$ $\mathbf{s_2 = 1.00}$	$s_{A_2} = 1.06$ $s_{G_2} = 1.11$ $s_2 = 0.96$	$s_{A_4} = 1.15$ $s_{G_4} = 1.51$ $s_4 = 0.94$	$s_{A_2} = 1.37$ $s_{G_2} = 1.54$ $s_2 = 0.96$
160	$\mathbf{s_{A_2} = 1.04}$ $\mathbf{s_{G_2} = 1.08}$ $\mathbf{s_2 = 1.04}$	$s_{A_2} = 1.05$ $s_{G_2} = 1.09$ $s_2 = 1.00$	$s_{A_4} = 1.39$ $s_{G_4} = 2.11$ $s_4 = 1.03$	$s_{A_2} = 1.28$ $s_{G_2} = 1.43$ $s_2 = 0.98$

Each update method is treated separately. The update methods except the one for $\boldsymbol{G}$ are parallelised with respect to the number of bodies or contacts using OpenMP on a two-core machine with dynamic scheduling. The update of $\boldsymbol{G}$ is parallelised using *ATLAS* on a four-core computer. The practical experiences for 80 and 160 elements are mean values from three calculations with 10 time and no plot steps. The following comments can be made:

- The contact solver vanishes from the table with methods of most computational amount and some of the methods change their priority in comparison to the chain of pearls example.
- The calculation of the gaps $\boldsymbol{g}$ and the gap velocities $\dot{\boldsymbol{g}}$ is dominated by the bilateral contact between elements and flexible band with 98.0% and 99.2%, respectively.
- Only the update of the Jacobian is worth to take for another test. The benefit of its parallelisation is at the theoretical maximum.

Table 2.5 shows methods with less overall computational amount.

Table 2.5: Not valuable items to parallelise for pushbelt CVT according profiling.

$\mathbf{N_E}$	update h	update M	update kinematics	GS solver
80	$\mathbf{s_2 = 1.00}$	$\mathbf{s_2 = 1.00}$	$s_2 = 0.96$	$s_2 = 0.96$
160	$\mathbf{s_2 = 1.04}$	$\mathbf{s_2 = 1.04}$	$s_2 = 1.00$	$s_2 = 1.00$

Even their parallelisation can be promising. Finally, the update of the right hand side $\boldsymbol{h}$, of the mass matrix $\boldsymbol{M}$ and of the Jacobians are selected as a bundle for a further test with 160 elements on different state-of-the-art personal computers with different operating systems (OS) and even virtual machines (VM) (Tab. 2.6).

As architecture No. 7 has been used for the separated analysis, this again shows that increasing the rate of parallisation not necessarily leads to lower computation time. Further, it is obvious that there is a major dependence on the computer architecture

Table 2.6: Test of update bundle on different computer architectures.

No.	architecture	OS	cores	update bundle
1	Intel Core i5 750 2.67GHz, 8MB L3-Cache, 4GB RAM	Windows 32bit	4 2 1	$s_4 = 1.01$ $s_2 = 1.00$ $t_1 = 30\,\mathrm{s}$
2	Intel Core i5 660 3.33GHz, 4MB L3-Cache, 8GB RAM	Linux 64bit	2 1	$s_2 = 0.95$ $t_1 = 40\,\mathrm{s}$
3	Intel Core i7 920 2.67GHz, 8MB L3-Cache, 6GB RAM	Linux 64bit	4 2 1	$s_4 = 0.88$ $s_2 = 0.96$ $t_1 = 43\,\mathrm{s}$
4	Intel Core i5 750 2.67GHz, 8MB L3-Cache, 4GB RAM	Linux 64bit	4 2 1	$s_4 = 0.88$ $s_2 = 0.97$ $t_1 = 44\,\mathrm{s}$
5	Intel Core2 Duo T9300 2.5GHz, 6MB L2-Cache, 4GB RAM	Windows 32bit VM Host: Linux 64bit	2 1	$s_2 = 1.02$ $t_1 = 45\,\mathrm{s}$
6	Intel Core i5 750 2.67GHz, 8MB L3-Cache, 2GB RAM	Linux 64bit VM Host: Windows 64bit	2 1	$s_2 = 0.96$ $t_1 = 46\,\mathrm{s}$
7	Intel Core2 Duo T9300 2.5GHz, 6MB L2-Cache, 4GB RAM	Linux 64bit	2 1	$s_2 = 1.02$ $t_1 = 51\,\mathrm{s}$
8	Intel Core2 Quad Q8300 2.67GHz, 4MB L2-Cache, 4GB RAM	Linux 64bit	4 2 1	$s_4 = 0.83$ $s_2 = 0.88$ $t_1 = 54\,\mathrm{s}$
9	Intel Core2 Duo E8400 3.0GHz, 6MB L2-Cache, 4GB RAM	Linux 64bit	2 1	$s_2 = 0.94$ $t_1 = 66\,\mathrm{s}$
10	Twin Dual Core AMD Opteron 280 2.4GHz, 2x2x1MB L2-Cache, 4GB RAM	Linux 64bit	4 2 1	$s_4 = 1.00$ $s_2 = 1.11$ $t_1 = 104\,\mathrm{s}$

similar to the *ATLAS* library. Setting the affinity of the different threads to specific cores deteriorates the results on all platforms.

The benefit of parallelisation is depending both on the model and on the computing architecture. For the chain of pearls and the real CVT example, totally different results have been achieved and also the test on different computers shows that an individual adjustment is necessary. One known but arbitrarily difficult possibility is the effective elimination of cache misses [80]. For the effective usage of GPU-based parallelisation, about 10^5 to 10^6 threads are needed [80] which normally is only the case for simulations with granular materials but not in the standard multibody framework.

Taking the current implementation as a basis, it is decided not to parallelise during the validation process but start different load cases on the available CPUs.

Memory usage

According to Sect. 1.4, *MBSim* uses the HDF5 file format for writing data for plot and visualisation. This conceptually allows the analysis of large data sets. Though from a practical point of view, this possibility leads to an extensive random access memory (RAM) request during simulation. That is why, one should compromise

about how many data sets should be written. Based on the visualisation, all the bodies of the multibody framework should be plotted. The contact data is only necessary for some selected elements. Table 2.7 gives an overview of computation time and memory usage for different number of elements used for contact plotting whereby always 10 time as well as 10 plot steps have been evaluated.

Table 2.7: Memory usage and computing time of plot in comparison to no plot data.

plotted elements	**160**	**80**	**40**	**20**	**10**	**5**	**0**
memory usage	195%	160%	135%	121%	**118**%	112%	109%
computing time	135%	113%	105%	104%	**102**%	102%	102%

The 160 element CVT example without plot data and a peak RAM usage of about 340 MB is the reference.

As a compromise, 10 elements uniformly distributed are selected for contact plotting during validation.

Analytical evaluations

The analytical evaluation of the JACOBIAN of the root function in the point-to-flexible band constraints improves the stability in Sect. 2.5.1 but does not reduce the computational effort. In contrary, the analytical calculation of the respective JACOBIAN in the circle-to-frustum constraints reduces the computing time about 6.5%. That is why, analytical formulas are used wherever possible according to the descriptions in the specific chapters.

3 Results and Validation

A first check on the feasibility of the prescribed model can be done by verifying *global* external signals like torques and clamping forces (thrusts). To achieve a more deep validation on the mechanical working principles of the system, it is preferred to look at *local* internal quantities for instance contact forces at the elements. Again, the review paper [72] gives a good overview about the current state of CVT measurements. The most interesting contributions concerning local contact forces are summarised in [22, 23, 35, 63], [13] describes measurements at Eindhoven University of Technology concerning global values. Recently in [49], experiments and simulations concerning bearing forces have been outlined. Thereby in addition, spiral running, the position of loose sheaves, deformation of fixed sheaves, shaft deflection, efficiency and the friction coefficients between elements and pulleys have been investigated experimentally.

It is hard to analyse the mechanism of CVTs experimentally and it is not easy to adjust the input parameters for the simulation. For example, it is not exactly true that $M_O = i_r M_I$ because of torque loss. It could happen that one cannot reach the maximum torque in the simulation since the belt already slips. The maximum torque can be estimated from a formula that contains for example running radius, clamping force and friction coefficient. These quantities are always a bit uncertain such that the calculated maximum torque will deviate a bit from the actual maximum torque. In that case, some lower values for the final torque are tried next to some strategic points in between 0 and the maximum value – one can see in the following sections.

All simulations have been done after a first parameter variation. Apart from the geometrical and material values of elements, ring package and pulleys (Sects. 2.1.1, 2.1.2, 2.1.3), mainly the following parameters have been adapted: Lehr damping values $\tilde{\vartheta}_{\kappa_0}$, $\tilde{\vartheta}_{\tilde{\epsilon}}$ of the ring packages, tilting parameters of the loose sheaves, the friction parameters of the interactions and l_E of the element – element contact. The simulation has been done with 12 finite elements for 9 rings, rigid sheaves and with 160 elements avoiding spurious polygonal effects. Where necessary, a dimensionless description is chosen because of industrial secrecy.

3.1 Planar Validation with Local Data

A full set of local measurements has been conducted by Doshisha University in Kyoto and Honda R&D in the 1990s at low belt speeds and clamping pressures [22, 23, 35]. It is important to know that obtaining these contact forces is a challenging task requiring complex and delicate measuring techniques [72, 27]: telemetry systems are

sensitive to bias and require the elements to be quipped with sensors. These design modifications possibly affect the tensile and bending stiffness of the elements. At Bosch Transmission Technology B.V., only push forces between adjacent elements have been measured. A method is described which uses a sensor placed inside a signaling element [86]. This approach allows for experiments close to normal operating conditions of the pushbelt. Always, the results are only qualitatively available and only trends can be compared. These trends behave similarly for all transmission ratios $i_r < 1$ and for all transmission ratios $i_r > 1$. In the following, simulation curves of one exemplary element resulting from the Bosch Transmission Technology B.V. setting with transmission ratio $i_r = 2.0$ are compared with the measurements of Honda. This allows a shorter simulation time, because the input pulley angular velocity for simulation $\dot{\gamma}_I = 100\pi\,{}^1/_\mathrm{s}$ allows a faster revolution of the examined element than the one for the measurements $\dot{\gamma}_I = 31\,{}^1/_\mathrm{s}$. Furthermore, one can consistently compare with the whole set of contact forces. The maximum output torques for simulation and measurement are $M_{O,\max} = 125\,\mathrm{Nm}$ and $M_{O,\max} = 76\,\mathrm{Nm}$. The remaining values are shown in Tab. 3.1.

Table 3.1: Load case for the contact force validation.

ξ_O	0.0	0.3	0.5	0.8
F_{C_O} (simulation)	20 kN	20 kN	20 kN	20 kN
F_{C_O} (measurement)	5 kN	5 kN	5 kN	5 kN

The curves are always depicted like in Fig. 3.1.

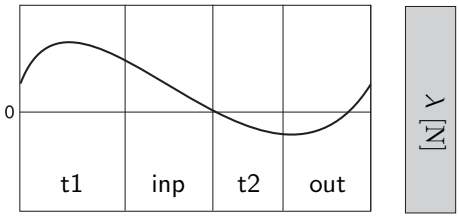

Figure 3.1: Distribution of a contact force λ within the trums and the pulleys.

The horizontal abscissa represents the actual position of the measuring element along the idealised cyclic reference path of the pushbelt running through the driving pulley wrapped arc *inp* along the strand *t1* towards the driven pulley entry, along its wrapped arc *out* and back along the strand *t2* to the starting position. In this manner the contact forces are a function of the reference path position assuming stationary behaviour.

3.1.1 Element – Pulley Contacts

Concerning the contact between element and pulley, one distinguishes between the normal, the radial and azimuthal components. As the measurements only represent the planar case, for the spatial simulations loose and fixed sheave contributions have to be summed-up, respectively.

Normal Contacts

Figure 3.2 shows a comparison of the normal component λ_{P_N} of the element to pulley contact.

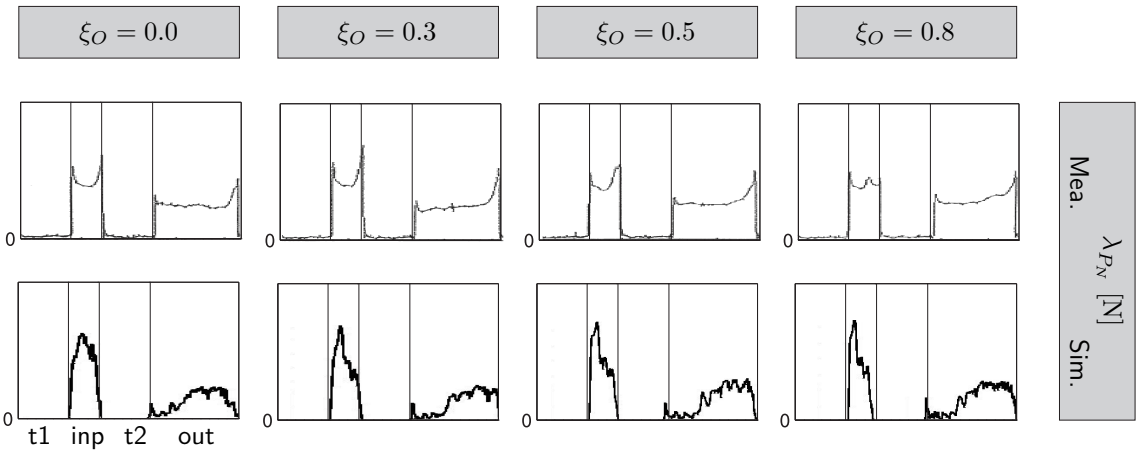

Figure 3.2: Measured and simulated normal contact between element and pulley.

This force arises if the element contacts the pulley.

It is very well reproduced by the calculations. Only the level of the simulation graphs at the running-in of the output pulley could be raised.

Radial Contacts

The radial component λ_{P_R} of the element – pulley contact force is depicted in Fig. 3.3.

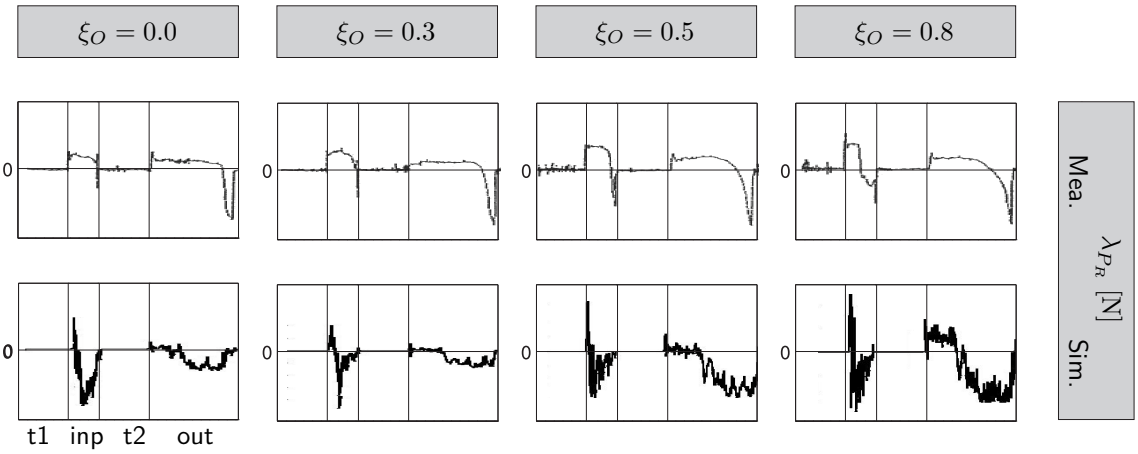

Figure 3.3: Measured and simulated radial contact between element and pulley.

The force counteracts the penetration of the pushbelt inwards to the pulley groove which is symbolised by a plus sign. When the element goes outwards from the pulley

groove, a negative force is obtained. The behaviour correlates with the analysis of the deviation of the element from its ideal circular radial position discussed in Sect. 3.2.2.

Again a good resemblance is achieved.

Azimuthal Contacts

In Fig. 3.4, one can see a comparison of the azimuthal component λ_{P_A} of the element to pulley contact force.

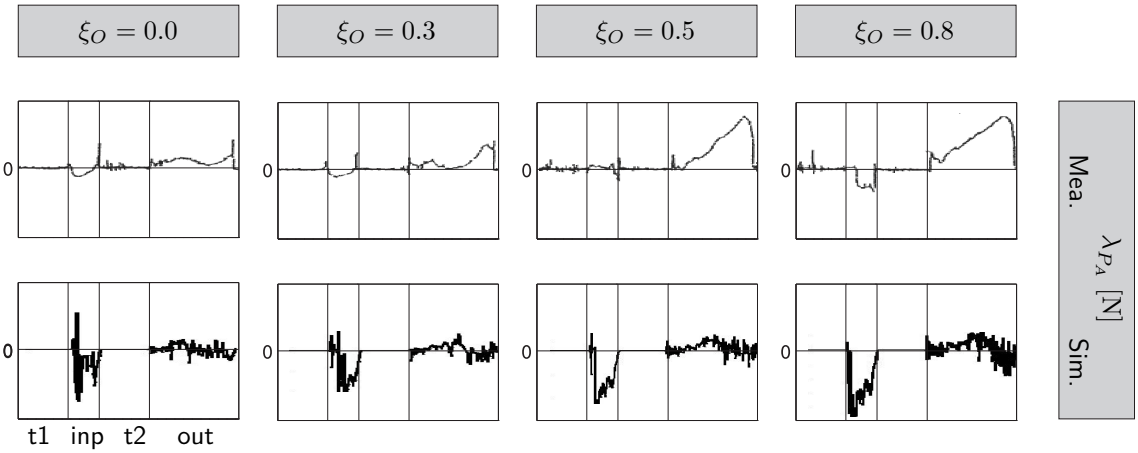

Figure 3.4: Measured and simulated azimuthal contact between element and pulley.

This force transmits power from the pulley to the pushbelt at the input and vice versa at the output active arcs. A plus sign means that the element drives the pulley. When the pulley drives the element, a minus sign occurs.

When comparing the curves, one has to take into account that the azimuthal equality of forces does not hold for the measurement curves. The fraction of positive forces is much higher than their negative counterpart. Though, the correlation in the input arc is quite good. In the output arc, an additional oscillation occurs in the simulation curves. When considering the mean values, a satisfactory match can be found.

3.1.2 Element – Ring Package Contacts

Like for the element – pulley contact, a normal and this time only one tangential component have to be discussed. The spatial values of the simulation are summarised to one planar result, respectively.

Normal Contacts

The element – ring package normal force acts on the element shoulder in order to keep the element in the pulley groove (cf. the force propagation λ_{R_N} in Fig.3.5).

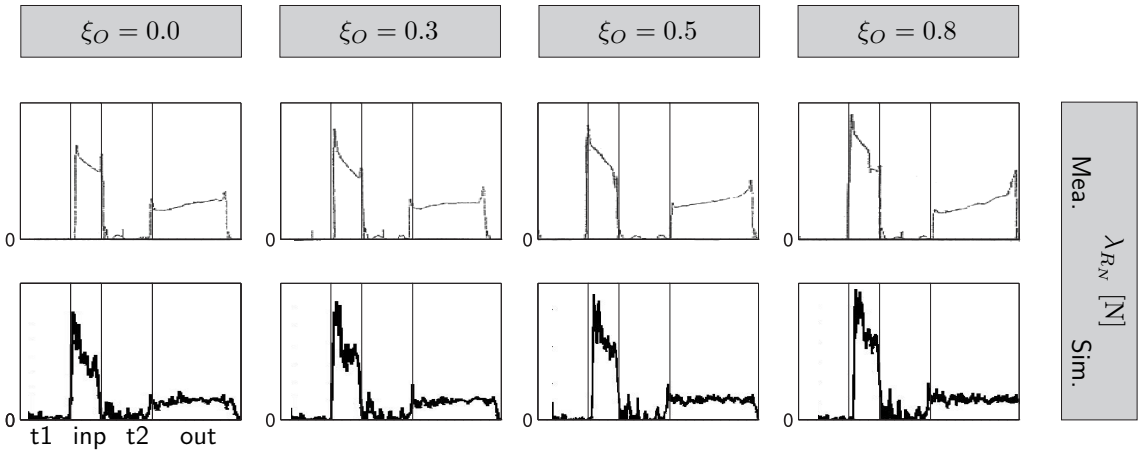

Figure 3.5: Measured and simulated normal contact between element and ring package.

It is caused by the prestressing of the ring packages and so correlates with their internal tensile forces. As both λ_{R_N} and λ_{P_N} have depending components, λ_{P_N} is influencing the behaviour of λ_{R_N}.

Simulation and measurement curves match very closely.

Tangential Contacts

Relative motion between element and ring packages is depicted by the tangential force in-between λ_{R_T} in Fig. 3.6.

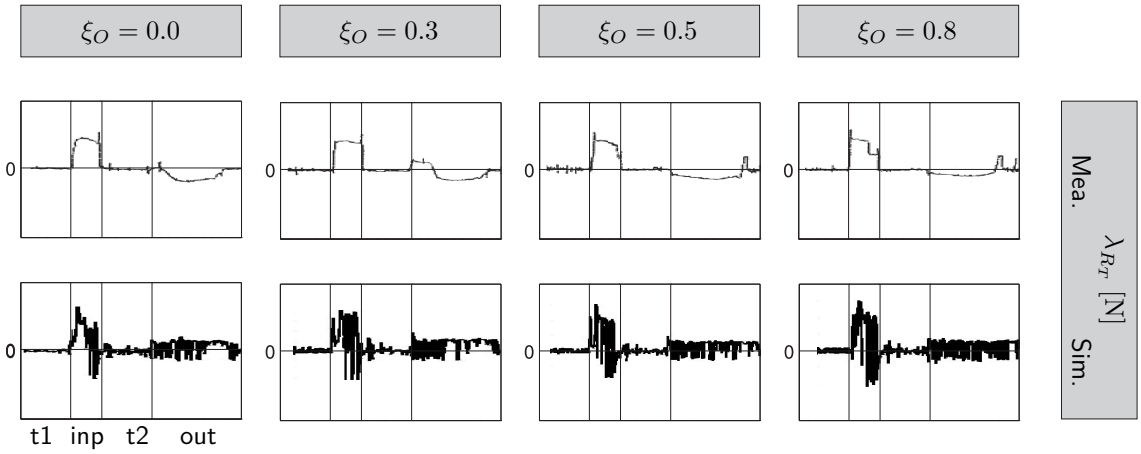

Figure 3.6: Measured and simulated tangential contact between element and ring package.

A negative signal means that the ring package pulls the element. For a plus sign, the element is faster than the ring package.

In the input pulley, one finds a good match. The contact force is clearly positive. The results of the simulation at the output pulley do not coincide with the measurement curves. According to oral statements of Bosch Transmission Technology B.V., λ_{R_T} should be around zero. This is not the case for both measurement and simulation. Though even if one ignores the oscillations in the simulation, the mean slip between elements and rings is obviously in the opposite direction with respect to the measurements. A physical interpretation of this phenomenon cannot be given.

3.1.3 Element – Element Contacts

It is the push force λ_{E_N} that is characteristic for the working principle of a pushbelt, which makes it essentially different from for instance chain type CVTs. It is expected that elements are compressed only in certain regions of the system. In other regions, they will separate because of longitudinal clearance between the elements. The push force is divided over the element into two rocking edge contacts and into a top area contact (Fig. 3.7).

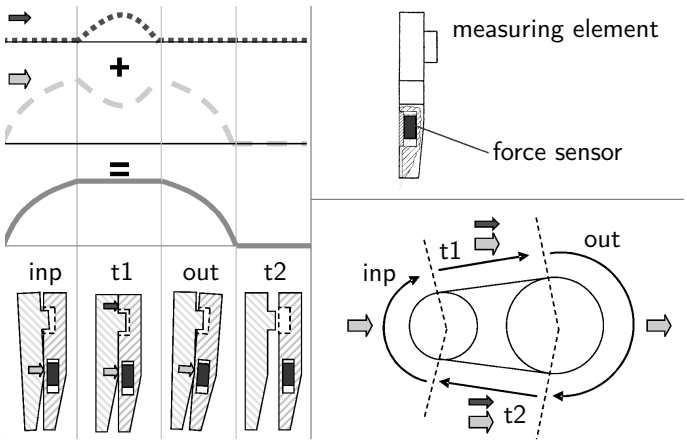

Figure 3.7: Push force measuring strategy and push force division.

When traveling around the variator reference path, the sensor only detects push forces when the element contacts its neighbours at the rocking edge. The simulation allows for all three contributions. The simulated push force results are presented in Fig. 3.8 in correspondence to the measured cases.

Obviously, the match between measurements and simulation is good apart from quite large oscillations in the simulation. The measured push force distribution shows a decrease on the strands in opposition to the simulations because of the mentioned missing top contact. The expected overall behaviour of the measurements is indicated by a dotted line.

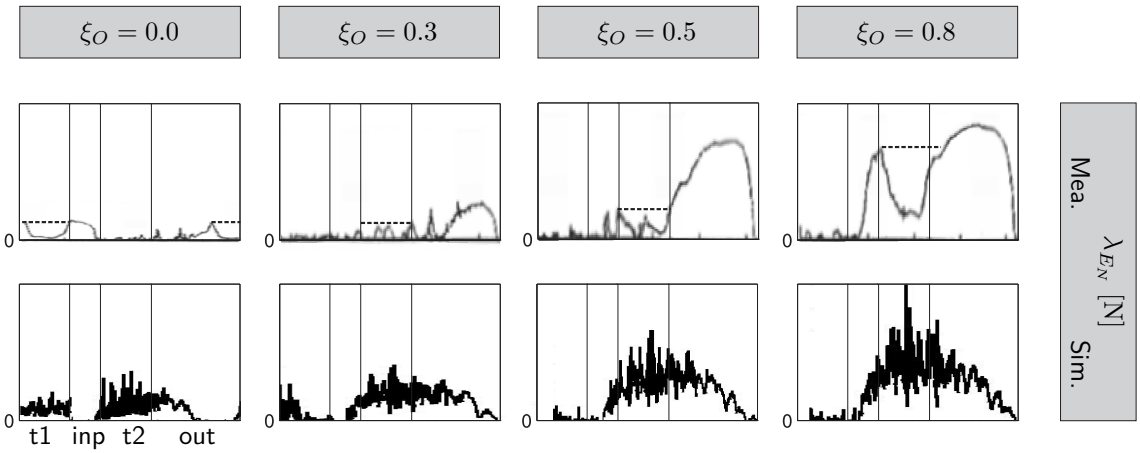

Figure 3.8: Measured and simulated normal contact between element and element.

3.2 Spatial Validation with Global Data

As local contact values are only available representing planar force distributions, the further reliability of the spatial simulation model has to be verified with global measurement data. The respective measurements have been conducted by Bosch Transmission Technology B.V.

3.2.1 Thrust Ratio

According to Sect. 1.1.2, the thrust ratio ζ is a very important criterion for pulley slip and so an essential characteristic of the overall physical behaviour. It is not easy to meet the different levels changing the transmission ratio i_r and output torque ratio ξ_O mainly due to deformation of the pulleys [49].

Figure 3.9 shows measured and simulated thrust ratio functions ζ in a stationary setting depending on the output torque ratios ξ_O for five different transmission ratios $i_r \in \{0.5, 0.6, 1.0, 1.6, 2.4\}$ in top-down arrangement. The remaining values of the load case are given by $\dot{\gamma}_I = \frac{200\pi}{3}\,{}^1\!/\!_{\mathrm{s}}$, $M_{O,\max} = 150\,\mathrm{Nm}$, $F_{C_O} = 11\,\mathrm{kN}$. For the simulation, the input thrust is given by the cutting force, for the measurements a control regulates the thrust yielding a quite nervous behaviour of the curves.

The correlation between simulation and measurements is good. The difference between corresponding curves is maximum about 25% also taking into account the measurement deviations.

3.2.2 Spiral Running

Spiral running is the about 1% spiral deviation of the elements from the circular radial position in the pulley grooves. Section 1.1.2 states that this is mainly influenced by the sheave flexibility and the prestressing of the ring packages. Of course

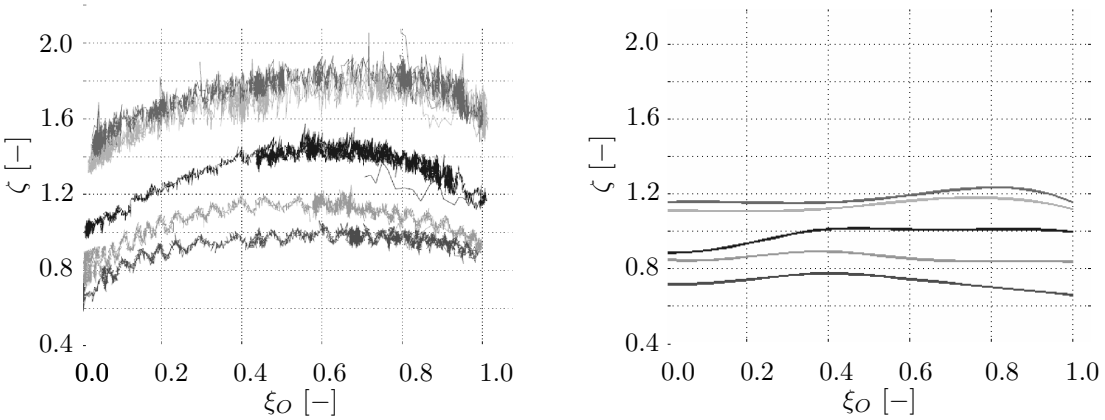

Figure 3.9: Measured (left) and simulated (right) thrust ratio.

there is also a correspondence to the radial friction force between element and pulley (Sect. 3.1.1).

Figure 3.10 shows the spiral running for $i_r = 2.4$ at the input pulley for four different torque ratios $\xi_O \in \{0.0, 0.4, 0.8, 1.0\}$ with respect to $M_{O,\max} = 260\,\mathrm{Nm}$ in top-down arrangement on the left side.

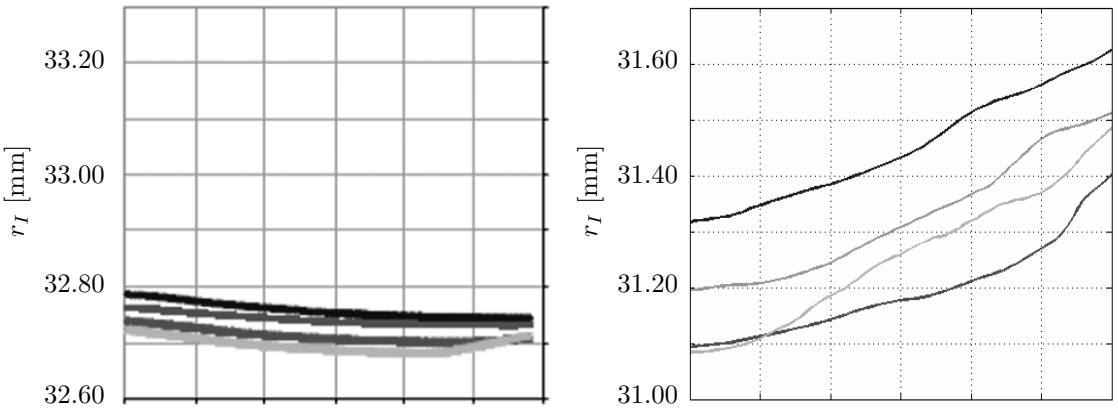

Figure 3.10: Measured (left) and simulated (right) spiral running for $i_r = 2.4$ at input.

The remaining values of the load case are given by $\dot{\gamma}_I = \frac{200\pi}{3}\,1/\mathrm{s}$, $F_{C_O} = 35\,\mathrm{kN}$. The results at the output pulley are presented in Fig. 3.11 whereby the curves are ordered bottom-up on the left side with respect to the increasing torque ratio.

Figure 3.12 depicts the spiral running for $i_r = 0.5$ at the input pulley for four different torque ratios $\xi_O \in \{0.0, 0.4, 0.7, 1.0\}$ with respect to $M_{O,\max} = 81\,\mathrm{Nm}$ in top-down arrangement on the left side.

The remaining values of the load case are given by $\dot{\gamma}_I = \frac{200\pi}{3}\,1/\mathrm{s}$, $F_{C_O} = 18\,\mathrm{kN}$. The results at the output pulley are described in Fig. 3.13 with the curves corresponding bottom-up on the left side to the increasing torque ratio.

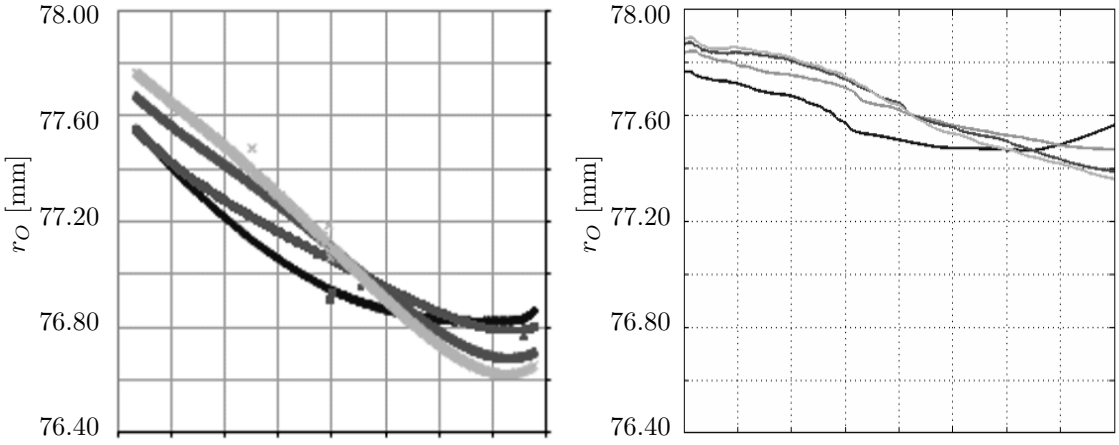

Figure 3.11: Measured (left) and simulated (right) spiral running for $i_r = 2.4$ at output.

The results are excellent, even better than for the thrust ratio. The corresponding curves differ at most 5%. The most obvious deviations occur at the smaller arcs. Here, measurements are less trustworthy and deformations smaller. The large arcs have the correct trend, the behaviour is very reasonable.

3.2.3 Alignment Setting

Equation (2.224) introduces a measure for the misalignment of the pushbelt. The amount of misalignment changes as a function of the transmission ratio due to the geometry of the sheaves and the fixed belt length (Fig. 2.21). Although misaligned running has no durability influence until the misalignment reaches a critical value, misalignment must be minimised in order to optimise functioning of the belt. Thus, the fixed sheaves in a CVT should be aligned in such a way that the belt runs straight. Section 2.3 states that this is not possible (Fig. 3.14). Finally, the misalignment

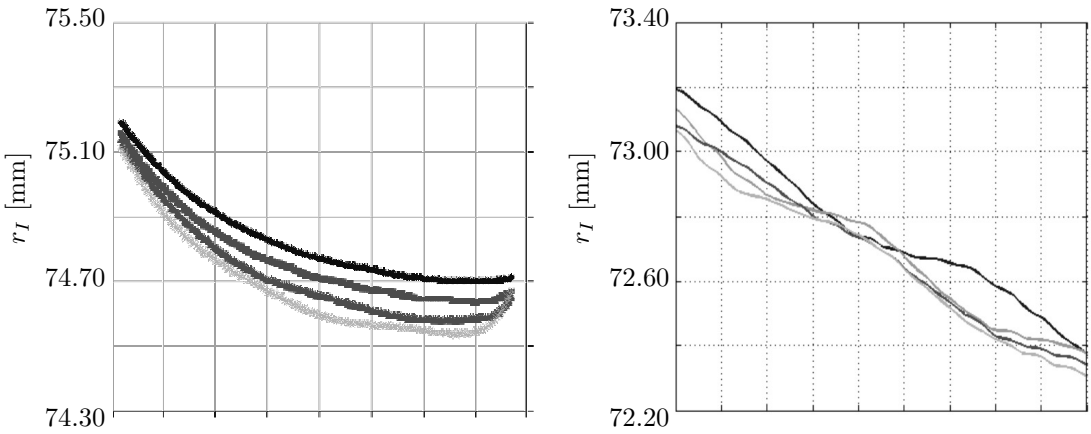

Figure 3.12: Measured (left) and simulated (right) spiral running for $i_r = 0.5$ at input.

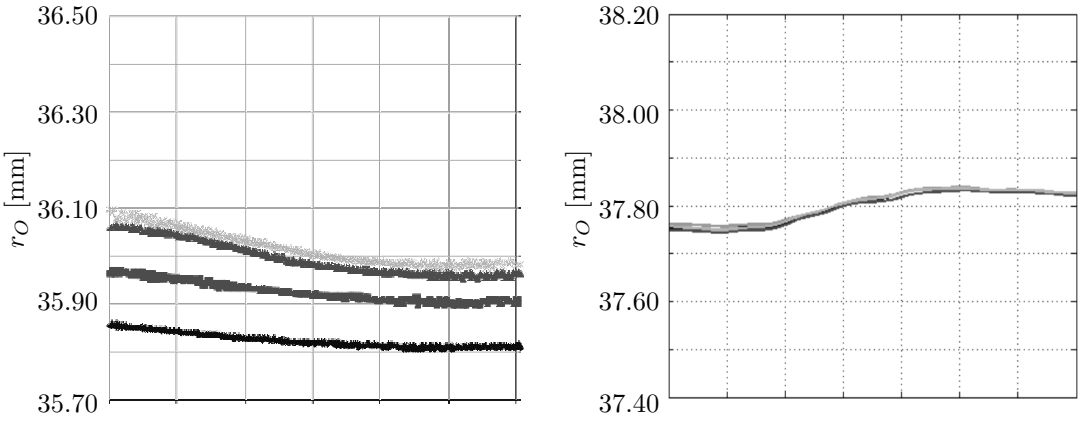

Figure 3.13: Measured (left) and simulated (right) spiral running for $i_r = 0.5$ at output.

function is constructed in a way such that the maximum deviation at top speed is minimal which is obtained for $i_r \approx 0.6$.

Figure 3.15 shows the simulation of a typical misalignment curve (left) and the measurements of a typical and two border (right) misalignment curves in the same scaling. The ordinate ticks have been neglected as the point of origin depends on the selection of the pulley alignment and so on the definition of the fixed sheaves. It is only worth to state the ordinate size of the simulation box with 1.2 mm. The pulley alignment is chosen such that the misalignment curve is in the area of good operation for each ratio. Outside this area, a significant increase in slip and so a decrease in the output angular velocity are measured. The size of the good area is larger towards $i_r = 2.6$ due to lower belt speed and becomes critical around the top speed. For each transmission ratio i_r, the load case is given by Tab. 3.2. At steady

Table 3.2: Load case for the alignment validation.

i_r	$\dot{\gamma}_I$	M_0	F_{C_O}
?	$\frac{200\pi}{3}$ 1/s	0.0	11 kN

states, the results of a typical curve are marked with a circle in Fig. 3.15. A steady

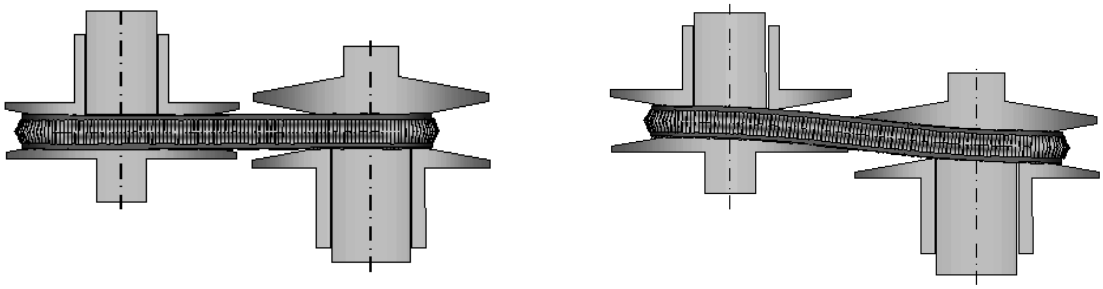

Figure 3.14: Straight and misaligned run of the pushbelt.

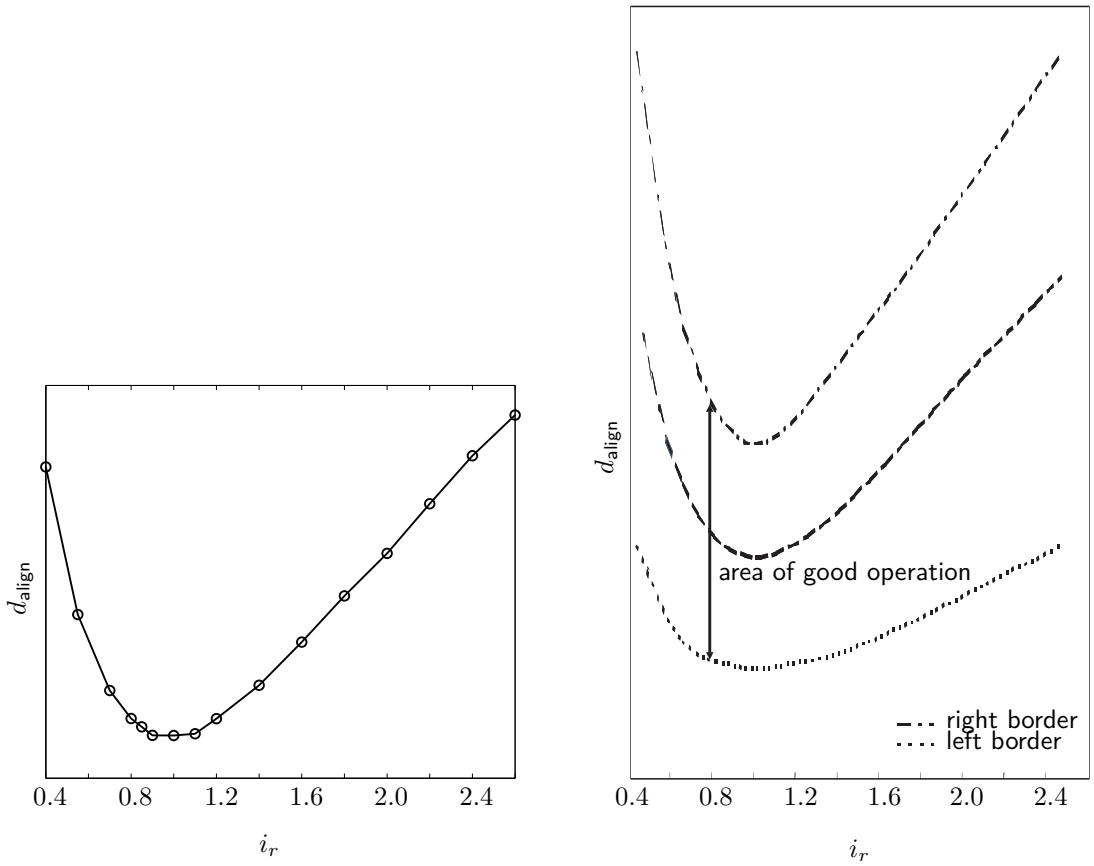

Figure 3.15: Simulated (left) and measured (right) misalignment in the magnitude 10^{-4} m.

state for each i_r is defined to be reached if the angular velocity of the output pulley is approximately periodic.

Altogether, a piecewise linear interpolation yields a very good agreement with the typical measurement curve.

4 Conclusion

A pushbelt CVT is an alternative transmission system with high expectation values to improve fuel economy and dynamic performance of a vehicle. Though, the expected increase has not been achieved in all cases [72]. For further analysing the system behaviour, experimental studies can be accomplished. This is a very sophisticated and expensive task. For effectively understanding and improving the system, it is often better to perform computer simulations. In chapter 1, set-up and functionality of pushbelt CVTs are outlined and important phenomena as well as necessary modelling prerequisites are given. A literature survey shows that there is still no spatial model considering all relevant flexibilities and transient states caused by ratio shifting. The only validated planar model representing all these issues [27] is based on the nonsmooth mechanics approach and is the point of departure for the present spatial extension. The basics and relevant literature citations about nonsmooth mechanics and its efficient discretisation with timestepping schemes are summarised. Therefore, theoretical and numerical formalisms are introduced and the software framework *MBSim* at the Institute of Applied Mechanics is described.

In chapter 2, a spatial transient model of a pushbelt variator is derived considering the components of the CVT and the different interactions separately. The elements are represented by rigid bodies. For the pulley sheaves, either a rigid description or a Reissner-Mindlin finite element plate with moving frame of reference can be selected. The ring packages are modelled with spatial large deformation beams based on co-rotational and inertial principles. For the interactions, it is distinguished between the sheave – sheave joint ensuring the same angular velocity within a pulley, the interactions to the environment defining the load case and internal CVT contact configurations. For the contact between elements and pulley sheaves, the contact law is chosen decoupled and flexible in normal direction. For the tangential direction, a Stribeck law is chosen. In the case of rigid sheaves, the contact kinematics can be analytically reduced and results in numerically solvable cone section problems. Otherwise, the contact kinematics has to be evaluated numerically from beginning. A NURBS-based surface description guarantees an efficient root search algorithm. For the contact between adjacent elements, only the normal direction is considered. The contact law is flexible and the respective kinematics can either be solved analytically or results in the same cone section problems as in the element – pulley setting. The last contact group is the guidance of the elements by the ring packages due to a bilateral normal contact law and Stribeck friction in tangential direction. In every case, a nonlinear equation has to be solved numerically during the contact search because of the numerical representation of the ring package. Initialisation and assembling for a stationary load case is done by using a simplified kinetic belt model. Hence, transient oscillations can be avoided. Altogether, a very detailed model has

been developed with a degree of freedom of about 3500 and 5500 contacts fulfilling the necessary prerequisites from chapter 1 and extending the model [27] according to Tab. 2.2. Parallelisation techniques and implicit integration schemes are tested to reduce the high computation time and practical experiences are summarised.

A validation of the overall simulation model is accomplished in chapter 3. Local contact forces between an exemplary element and the pulleys, the ring packages as well as an adjacent element are discussed and compared. Throughout, the results are in good correspondence. As the available measurements only reflect the planar case, additionally global values are examined. The thrust ratio curves differ maximum about 25% and show a good correlation. The radial deviation of the element curve in the pulley groove from a circle is called spiral running and drifts at most 5% from the measurements. Last, the typical misalignment curve is also very well reproduced. Overall one can conclude that the typical behaviour of the pushbelt variator system at realistic operation conditions is predicted adequately by the mathematical model.

The simulation model both represents the most important phenomena and shows a good correlation with experimental results. It can be applied to analyse the dynamics of the real system and to improve its performance concerning out-of-plane motion, misalignment, comfort and fuel consumption. Though to use it with control algorithms, as part of drivetrain models or with mathematical optimisation methods, reduced models would be more appropriate. The proposed model is an excellent origin to develop such simplifications by model order reduction techniques [19] or by substituting some bodies for instance the ring models with the promising one in [41] or interactions for example the dynamic sheave representation with a quasi-static Maxwell law [27]. Then, these new models could be understood in detail due to comparability and would be fast enough to derive ratio and thrust shifting rules predicting and optimising the slip behaviour also in comparison to planar descriptions. According to the author, this will be one of the most important issues for the future such that it is always ensured that operating conditions automatically meet the load requirements [72]. Another item is the improvement of parallelisation concepts using the OpenMP standard mainly analysing cache misses. GPU-based parallelisation is only effective for granular materials [80].

Bibliography

[1] Acary, Vincent ; Brogliato, Bernard: *Lecture notes in applied and computational mechanics*. Vol. 35: *Numerical methods for nonsmooth dynamical systems: applications in mechanics and electronics*. 1st edition. Berlin : Springer, 2008. – ISBN 3–540–75391–5

[2] Acary, Vincent ; Perignon, Franck: An introduction to Siconos / INRIA. 2007. – Forschungsbericht

[3] Alart, Pierre ; Curnier, Alain: A mixed formulation for frictional contact problems prone to Newton like solution methods. In: *Comput Methods Appl Mech Engrg* 92 (1991), pp. 353 – 375. – ISSN 0045–7825

[4] Arnold, Martin: Numerical methods for simulation in applied dynamics. In: Arnold, Martin (Hrsg.) ; Schiehlen, Werner (Hrsg.): *Simulation Techniques for Applied Dynamics*. Wien : Springer, 2009 (CISM International Centre for Mechanical Sciences 507). – ISBN 978–3–211–89548–1, pp. 191–246

[5] Bathe, Klaus-Jürgen ; Bolourchi, Said: Large displacement analysis of three-dimensional beam structures. In: *Int J Numer Meth Eng* 14 (1979), pp. 961–986. – ISSN 0029–5981

[6] Belytschko, Ted ; Schwer, Leonard: Large displacement, transient analysis of space frames. In: *Int J Numer Meth Eng* 11 (1977), pp. 65–84. – ISSN 0029–5981

[7] Berard, Stephan ; Trinkle, Jeff ; Nguyen, Binh ; Roghani, Ben ; Fink, Jonathan ; Kumar, Vijay: daVinci Code: a multi-model simulation and analysis tool for multi-body systems. In: *2007 IEEE International Conference on Robotics and Automation ; Roma, Italy, 10th-14th April 2007*, IEEE, 2007. – ISBN 1–4244–0602–1, pp. 2588–2593

[8] Bhate, Rohan ; Srivastava, Nilabh: Influence of pulley actuation force on the transient dynamics of a metal V-belt CVT. In: *SAE 2009 Commercial Vehicle Engineering Congress & Exhibition Technical, Rosemont, Illinois, 6th until 7th October 2009*, 2009

[9] Braess, Dietrich: *Finite elements : theory, fast solvers, and applications in elasticity theory*. 3. ed. Cambridge : Cambridge University Press, 2007. – ISBN 978–0–521–70518–9

[10] Brogliato, Bernard: *Lecture notes in control and information sciences*. Vol. 220: *Nonsmooth impact mechanics : models, dynamics and control*. 1st edition. London : Springer, 1996. – ISBN 3–540–76079–2

[11] Brogliato, Bernard ; Dam, Tonny ten ; Paoli, Laetitia ; Genot, Frank ; Abadie, Michel: Numerical simulation of finite dimensional multibody nonsmooth mechanical systems. In: *Appl Mech Rev* 55 (2002), pp. 107–150. – ISSN 0003–6900

[12] Bullinger, Markus ; Pfeiffer, Friedrich ; Ulbrich, Heinz: Elastic modelling of bodies and contacts in continuously variable transmissions. In: *Multibody System Dynamics* 13 (2005), pp. 175–194. – ISSN 1573–272X

[13] Carbone, Giuseppe ; Mangialardi, Luigi ; Bonsen, Bram ; Tursi, Carlo; Veenhuizen, Bram: CVT dynamics: theory and experiments. In: *Mech Mach Theor* 42 (2006), pp. 409–428. – ISSN 0094–114X

[14] Carbone, Guiseppe ; Novellis, Leonardo de ; Commissaris, Gijs ; Steinbuch, Maarten: An enhanced CMM model for the accurate prediction of steady state performance of CVT chain drives. In: *J Mech Des* 132 (2010), pp. 1–8. – ISSN 1050–0472

[15] Chapman, Barbara ; Gabriele ; Jost ; Pas, Ruud van d.: *Using OpenMP : portable shared memory parallel programming*. Cambridge, Mass. : MIT Press, 2008 (Scientific and engineering computation). – ISBN 978–0–262–53302–7

[16] Crisfield, Michael A.: A consistent co-rotational formulation for non-linear, three-dimensional, beam elements. In: *Comput Methods Appl Mech Engrg* 81 (1990), pp. 131–150. – ISSN 0045–7825

[17] Deuflhard, Peter: *Springer series in computational mathematics*. Vol. 35: *Newton methods for nonlinear problems : affine invariance and adaptive algorithms*. Corr. 2. print. Berlin : Springer, 2006. – ISBN 3–540–21099–7

[18] Dombrowski, Stefan von ; Schwertassek, Richard: Analysis of large flexible body deformation in multibody systems using absolute coordinates. In: *Advances in Computational Multibody Dynamics, Lisbon, 20th-23rd September 1999*. Lisbon, Portugal : Instituto Superior Tecnico, 1999, pp. 359–378

[19] Fehr, Jörg ; Eberhard, Peter: Improving the simulation process in flexible multibody dynamics by enhanced model order reduction techniques. In: *Multibody Dynamics 2009, Eccomas Thematic Conference, Warsaw, 29th June until 2nd July 2009*, 2009

[20] Flores, Paulo ; Leine, Remco I. ; Glocker, Christoph: Modeling and analysis of rigid multibody systems with translational clearance joints based on the nonsmooth dynamics approach. In: *Multibody Dynamics 2009, Eccomas Thematic Conference, Warsaw, 29th June until 2nd July 2009*, 2009

[21] *fmatvec - Fast Matrix-Vector Library*. GNU Lesser General Public License `http://fmatvec.berlios.de`

[22] Fujii, Toru ; Kitagawa, Takashi ; Kanehara, Shigeru: A study of a metal pushing V-belt type CVT - part 2: compression force between metal blocks and ring tension. In: *SAE Technical Paper Series* 930667 (1993), pp. 129–138. – ISSN 0148–7191

[23] Fujii, Toru ; Kurokawa, Takemasa ; Kanehara, Shigeru: A study of a metal pushing V-belt type CVT - part 1: relation between transmitted torque and pulley thrust. In: *SAE Technical Paper Series* 930666 (1993), pp. 117–127. – ISSN 0148–7191

[24] Funk, Kilian ; Pfeiffer, Friedrich: A time-stepping algorithm for stiff mechanical systems with unilateral constraints. In: *International Conference on Nonsmooth/Nonconvex Mechanics with Applications in Engineering , Thessaloniki , 5th until 6th July 2002*, 2002

[25] Förg, Martin: *Fortschritt-Berichte VDI : Reihe 20, Rechnerunterstützte Verfahren*. Vol. 411: *Mehrkörpersysteme mit mengenwertigen Kraftgesetzen : Theorie und Numerik*. Als Manuskript gedruckt. Düsseldorf : VDI-Verl., 2007. – ISBN 978–3–18–341120–7

[26] Förg, Martin ; Engelhard, Thomas ; Ulbrich, Heinz: Analysis of different time-integration methods applied to a nonsmooth industrial problem. In: *Fifth EUROMECH Nonlinear Dynamics Conference : 7th-12th August 2005*. Eindhoven : Eindhoven Univ. of Technology, August 2005

[27] Geier, Thomas: *Fortschrittberichte VDI : Reihe 12, Verkehrstechnik, Fahrzeugtechnik*. Vol. 654: *Dynamics of push belt CVTs*. Als Manuskript gedruckt. Düsseldorf : VDI-Verl., 2007. – ISBN 978–3–18–365412–3

[28] Gerbert, Göran: Influence of band friction on metal V-belt mechanics / Division of Machine Elements, Chalmers University of Technology. Göteborg, 1985 (1985-08-25). – Forschungsbericht

[29] Gerstmayr, Johannes: *Absolute coordinate formulations for flexible multibody dynamics systems*, Johannes Kepler Universität Linz, Diss., 2007

[30] Glocker, Christoph: *Lecture notes in applied and computational mechanics*. Vol. 1: *Set-valued force laws in rigid body dynamics : dynamics of non-smooth systems*. 1st edition. Berlin : Springer Verlag, 2001. – ISBN 978–3–540–41436–0

[31] Hairer, Ernst ; Wanner, Gerhard: *Springer series in computational mathematics*. Vol. 14: *Solving ordinary differential equations*. Corrected Second Printing. Berlin : Springer, 2002. – ISBN 3–540–60452–9

[32] *HDF5Serie - A HDF5 Wrapper for Time Series*. GNU Lesser General Public License
`http://hdf5serie.berlios.de`

[33] Hilbert, David ; Cohn-Vossen, Stephan: *Geometry and the imagination*. 2. ed., repr. Providence, RI : AMS Chelsea Publ., 1999. – ISBN 0–8218–1998–4

[34] Jean, Michel: The nonsmooth contact dynamics method. In: *Comput Methods Appl Mech Engrg* 177 (1999), pp. 235–257. – ISSN 0045–7825

[35] Kanehara, Shigeru ; Fujii, Toru ; Kitagawa, Takashi: A study of a metal pushing V-belt type CVT - part 3: what forces act on metal blocks. In: *SAE Technical Paper Series* 940735 (1994), pp. 139–169. – ISSN 0148–7191

[36] Kell, Thomas ; Fritz, Peter ; Pfeiffer, Friedrich: Vibrations in roller chain drives. In: *5th International Congress on Sound and Vibration, Adelaide, 15th until 18th December 1997*, 1997

[37] Kikuchi, Fumio: An improved 4-node quadrilateral plate bending element of the Reissner-Mindlin type. In: *Comput Mech* 23 (1999), pp. 240–249. – ISSN 0178–7675

[38] Klaassen, Tim ; Bonsen, Bram ; Meerakker, Koen van d. ; Vroemen, Bas ; Veenhuizen, Bram ; Veldpaus, Frans ; Steinbuch, Maarten: The empact CVT: modelling, simulation and experiments. In: *Int J Modelling, Identification and Control* 3 (2008), pp. 286–296. – ISSN 1746–6172

[39] Krüssmann, Martin: A new CVT push-belt to increase driveline efficiency and power density. In: *8th International CTI Symposium: Innovative Automotive Transmissions, Berlin, 30th November until 3rd December 2009*, 2009

[40] Kuwabara, Shinya ; Fujii, Toru ; Kanehara, Shigeru: Power transmitting mechanisms of CVT using a metal V-belt and load distribution in the steel ring. In: *SAE Technical Paper Series* 980824 (1998), pp. 49–59. – ISSN 0148–7191

[41] Lang, Holger ; Linn, Joachim ; Arnold, Martin: Multibody dynamics simulation of geometrically exact Cosserat rods. In: *Multibody Dynamics 2009, Eccomas Thematic Conference, Warsaw, 29th June until 2nd July 2009*, 2009

[42] Lebrecht, Wolfgang ; Pfeiffer, Friedrich ; Ulbrich, Heinz: Analysis of self-induced vibrations in a pushing V-belt CVT. In: *International Continuously Variable and Hybrid Transmission Congress, San Francisco, 23rd until 25th September 2004*, 2004

[43] Leine, Remco I. ; Glocker, Christoph: A set-valued force law for spatial Coulomb-Contensou friction. In: *Eur J Mech* 22 (2003), pp. 193–216. – ISSN 0997–7546

[44] Leine, Remco I. ; Nijmeijer, Hendrik: *Lecture notes in applied and computational mechanics*. Vol. 18: *Dynamics and bifurcations of non-smooth mechanical systems*. Corr. print. Berlin : Springer, 2006. – ISBN 3–540–21987–0

[45] Leine, Remco I. ; Wouw, Nathan van d.: *Lecture notes in applied and computational mechanics*. Vol. 36: *Stability and convergence of mechanical systems with unilateral constraints*. Berlin : Springer, 2008. – ISBN 978–3–540–76975–0

[46] Luo, Albert: *Discontinuous dynamical systems in time-varying domains*. Beijing : Higher Education Press, 2009 (Nonlinear physical science). – ISBN 978–3–642–00252–6

[47] *MBSim - Multi-Body Simulation Software*. GNU Lesser General Public License `http://mbsim.berlios.de`

[48] Moreau, Jean J.: Unilateral contact and dry friction in finite freedom dynamics. In: *Nonsmooth Mechanics and Applications*. Wien : Springer Verlag, 1988. – ISBN 3–211–82066–3, pp. 1–82

[49] Möller, Jens: *Konstruktions- und Antriebstechnik*. Vol. 3: *Rechnerische und experimentelle Bestimmung der Lagerkräfte eines stufenlosen Umschlingungsgetriebes*. Tönning : Der Andere Verlag, 2010. – ISBN 978–3–89959–966–4

[50] Möller, Michael ; Leine, Remco I. ; Glocker, Christoph: An efficient approximation of orthotropic set-valued force laws of normal cone type. In: *7th Euromech Solid Mechanics Conference, Lisbon, 7th until 11th September 2009*, 2009

[51] Neumann, Lutz ; Ulbrich, Heinz ; Pfeiffer, Friedrich: New model of a CVT rocker pin chain with exact joint kinematics. In: *J Comput Nonlinear Dynam* 1 (2006), pp. 143–149. – ISSN 1555–1415

[52] Noll, Erik van d. ; Sluis, Francis van d. ; Dongen, Tom van ; Velde, Arie van d.: Innovative self-optimizing clamping force strategy boosts effiency of the pushbelt CVT. In: *7th International CTI Symposium: Innovative Automotive Transmissions, Berlin, 1st until 4th December 2008*, 2008

[53] *OpenMBV - Open Multi Body Viewer*. GNU General Public License `http://openmbv.berlios.de`

[54] Pfeiffer, Friedrich: *Lecture notes in applied and computational mechanics*. Vol. 40: *Mechanical system dynamics*. Corr. 2. print. Berlin : Springer, 2008. – ISBN 978–3–540–79435–6

[55] Pfeiffer, Friedrich ; Borchsenius, Fredrik ; Förg, Martin: New hydraulic system modelling. In: *ASME Design Engineering Technical Conference, Chicago, 2nd - 6th September 2003*, 2003

[56] Pfeiffer, Friedrich ; Glocker, Christoph: *Multibody dynamics with unilateral contacts*. 1st edition. New York : John Wiley & Sons Inc., 1996 (Wiley series in nonlinear science). – ISBN 0–471–15565–9

[57] Piegl, Les ; Tiller, Wayne: *The NURBS book*. 2. ed. Berlin : Springer, 1997 (Monographs in visual communications). – ISBN 3–540–61545–8

[58] Rothenbühler, Yves: *New slip synthesis and theoretical approach of CVT slip control*, Ecole Polytechnique Federale de Lausanne, Diss., 2009

[59] Sattler, Heiko: *Stationäres Betriebsverhalten stufenlos verstellbarer Metallumschlingungsgetriebe*, Universität Hannover, Diss., 1999

[60] Schiehlen, Werner: Multibody system dynamics: roots and perspectives. In: *Multibody System Dynamics* 1 (1997), pp. 149–188. – ISSN 1384–5640

[61] Schindler, Thorsten ; Friedrich, Markus ; Ulbrich, Heinz: Computing time reduction possibilities in multibody dynamics. In: Blajer, Wojciech (Hrsg.) ; Arczewski, Krzysztof (Hrsg.) ; Fraczek, Janusz (Hrsg.) ; Wojtyra, Marek (Hrsg.): *Multibody Dynamics: Computational Methods and Applications*. Dordrecht : Springer, to appear 2010 (Computational Methods in Applied Sciences)

[62] Schindler, Thorsten ; Förg, Martin ; Friedrich, Markus ; Schneider, Markus ; Esefeld, Bastian ; Huber, Robert ; Zander, Roland ; Ulbrich, Heinz: Analysing dynamical phenomenons: introduction to MBSim. In: *Proceedings of 1st Joint International Conference on Multibody System Dynamics, Lappeenranta, 25th-27th May 2010*, 2010. – ISBN 978–952–214–778–3

[63] Schindler, Thorsten ; Geier, Thomas ; Ulbrich, Heinz ; Pfeiffer, Friedrich ; Velde, Arie van d. ; Brandsma, Arjen: Dynamics of pushbelt CVTs. In: *Umschlingungsgetriebe : Ketten und Riemen - Konstruktion, Simulation und Anwendung von Komponenten und Systemen; Tagung Berlin, 21. und 22. Juni 2007*. Düsseldorf : VDI-Verlag, 2007 (VDI-Berichte ; 1997). – ISBN 978–3–18–091997–3

[64] Schindler, Thorsten ; Ulbrich, Heinz ; Pfeiffer, Friedrich ; Velde, Arie van d. ; Brandsma, Arjen: Spatial simulation of pushbelt CVTs with timestepping schemes. In: *Appl Numer Math* (to appear 2010). – ISSN 0168–9274

[65] Sedlmayr, Martin: *Fortschrittberichte VDI : Reihe 12, Verkehrstechnik, Fahrzeugtechnik*. Vol. 558: *Räumliche Dynamik von CVT-Keilkettengetrieben*. Als Manuskript gedruckt. Düsseldorf : VDI-Verlag, 2003. – ISBN 3–18–355812–2

[66] Shabana, Ahmed: *Dynamics of multibody systems*. 3. ed. New York : Cambridge University Press, 2005. – ISBN 0–521–85011–8

[67] Shabana, Ahmed ; Bauchau, Olivier ; Hulbert, Gregory: Integration of large deformation finite element and multibody system algorithms. In: *J Comput Nonlinear Dynam* 2 (2007), pp. 351–359. – ISSN 1555–1415

[68] Simo, Juan C. ; Vu-Quoc, Loc: A geometrically-exact rod model incorporating shear and torsion-warping deformation. In: *Int J Solid Struct* 27 (1991), pp. 371–393. – ISSN 0020–7683

[69] Simons, Sjoerd ; Klaassen, Tim ; Veenhuizen, Bram ; Carbone, Giuseppe: Shift dynamics modelling for optimisation of variator slip control in a pushbelt CVT. In: *Int J Vehicle Design* 48 (2008), pp. 45–64. – ISSN 0143–3369

[70] Sluis, Francis van d. ; Dongen, Tom van ; Spijk, Gert-Jan van ; Velde, Arie van d. ; Heeswijk, Ad van: Fuel consumption potential of the pushbelt CVT. In: *FISITA 2006 : World Automotive Congress; 22 - 27 October, Yokohama, Japan*. Yokohama, 2006

[71] Sorge, Francesco: Transient mechanics of V-belt variators. In: *International Continuously Variable and Hybrid Transmission Congress, San Francisco, 23rd until 25th September 2004*, 2004

[72] Srivastava, Nilabh ; Haque, Imtiaz: A review on belt and chain continuously variable transmissions (CVT): dynamics and control. In: *Mech Mach Theor* 44 (2008), pp. 19–41. – ISSN 0094–114X

[73] Srivastava, Nilabh ; Haque, Imtiaz: Transient dynamics of metal V-belt CVT: effect of band pack slip and friction characteristic. In: *Mech Mach Theor* 43 (2008), pp. 459–479. – ISSN 0094–114X

[74] Srnik, Jürgen ; Pfeiffer, Friedrich: Dynamics of CVT chain drives. In: *Int J Vehicle Design* 22 (1999), pp. 54–72. – ISSN 0143–3369

[75] Stadler, Michael ; Holzapfel, Gerhard: Subdivision schemes for smooth contact surfaces of arbitrary mesh topology in 3D. In: *Int J Numer Meth Eng* 60 (2004), pp. 1161–1195. – ISSN 0029–5981

[76] Stadler, Michael ; Holzapfel, Gerhard ; Korelc, Joze: C^n continuous modelling of smooth contact surfaces using NURBS and application to 2D problems. In: *Int J Numer Meth Eng* 57 (2003), pp. 2177–2203. – ISSN 0029–5981

[77] Stewart, David: Rigid-body dynamics with friction and impact. In: *SIAM Rev* 42 (2000), pp. 3–39. – ISSN 1095–7200

[78] Stiegelmeyr, Andreas: A time stepping algorithm for mechanical systems with unilateral contacts. In: *ASME International Design Engineering Technical Conference, Las Vegas, 4th until 7th September 1999*, ASME, 1999

[79] Studer, Christian: *Lecture notes in applied and computational mechanics.* Vol. 47: *Numerics of unilateral contacts and friction : modeling and numerical time integration in non-smooth dynamics.* Berlin : Springer Verlag, 2009. – ISBN 978–3–642–01099–6

[80] Tasora, Alessandro ; Negrut, Dan ; Anitescu, Mihail: GPU-based parallel computing for the simulation of complex multibody systems with unilateral and bilateral constraints: an overview. In: Blajer, Wojciech (Hrsg.) ; Arczewski, Krzysztof (Hrsg.) ; Fraczek, Janusz (Hrsg.) ; Wojtyra, Marek (Hrsg.): *Multibody Dynamics: Computational Methods and Applications.* Dordrecht : Springer, to appear 2010 (Computational Methods in Applied Sciences)

[81] Tenberge, Peter: Efficiency of chain-CVTs at constant and variable ratio: a new mathematical model for a very fast calculation of chain forces, clamping forces, clamping ratio, slip, and efficiency. In: *International Continuously Variable and Hybrid Transmission Congress, San Francisco, 23rd until 25th September 2004*, 2004

[82] Thomsen, Per G. (Hrsg.): *Non-smooth problems in vehicle systems dynamics : Proceedings of the Euromech 500 Colloquium*. Berlin : Springer, 2010. – ISBN 978–3–642–01355–3

[83] Trinkle, Jeffrey ; Pang, Jong-Shi ; Sudarsky, Sandra ; Lo, Grace: On dynamic multi-rigid-body contact problems with Coulomb friction. In: *J Appl Math Mech* 4 (1997), pp. 267–279. – ISSN 0044–2267

[84] Ugural, Ansel ; Fenster, Saul: *Advanced strength and applied elasticity*. New York : American Elsevier, 1975. – ISBN 0–444–00160–3

[85] Ulbrich, Heinz: Some selected research activities in mechatronic applications - case studies. In: *International Conference on Engineering Mechanics, Structures, Engineering Geology, Rhodos, 22nd until 24th July 2009*, 2009

[86] VDT. *European Patent EP-0772034 Measuring system for belt forces occurring in variator systems in dynamical circumstances*. 1996

[87] Wasfy, Tamer ; Noor, Ahmed: Computational strategies for flexible multibody systems. In: *Appl Mech Rev* 56 (2003), pp. 553–613. – ISSN 0003–6900

[88] Wriggers, Peter: *Computational contact mechanics*. 1st edition. Chichester West Sussex : John Wiley & Sons Ltd., 2002. – ISBN 0–471–49680–4

[89] Zander, Roland: *Fortschritt-Berichte VDI : Reihe 20, Rechnerunterstützte Verfahren*. Vol. 420: *Flexible multi-body systems with set-valued force laws*. Als Manuskript gedruckt. Düsseldorf : VDI-Verlag, 2009. – `http://mediatum2.ub.tum.de/node?id=654788`. – ISBN 978–3–18–342020–9

[90] Zander, Roland ; Schindler, Thorsten ; Friedrich, Markus ; Huber, Robert ; Förg, Martin ; Ulbrich, Heinz: Non-smooth dynamics in academia and industry: recent work at TU München. In: *Acta Mech* 195 (2008), pp. 167–183. – ISSN 0001–5970

[91] Zander, Roland ; Ulbrich, Heinz: Rotating elastic disks with rigid body contacts in MBS. In: *Proceedings of the 77th Annual Meeting of the Gesellschaft für Angewandte Mathematik und Mechanik e.V.* Bremen : Universität Bremen, March 2006